Specific Absorption Rate Distribution in Simple Geometrical Bodies at Radio Frequencies

by

Gary Hing-On Wong

A thesis
submitted to the
School of Graduate Studies and Research
of the University of Ottawa
as partial fulfillment of the
requirements for the degree of
M.A.Sc
in the
Department of Electrical Engineering

OTTAWA, Ontario, 1983

The University of Ottawa requires the signatures of all persons using or photocopying this thesis. Please sign below, and give address and date.

ABSTRACT

The theoretical and experimental induced field distributions in simple spherical, cylindrical, and block models under plane wave irradiation are studied and compared. The practical limitations and calibrations of a new computer-based scanning system using an electric-field-probe technique are derived from the compared results in simple models for three different frequencies. Although close correlations between the calculated and measured results in the spherical and cylindrical models are found, large discrepancies in the compared results for the block model occurred. These discrepancies are mostly due to the nonisotopic response of the probe and the direct pick-up by the lossy transmission lines in the probe. They are also partly due to the inaccurate numerical solutions obtained from the tensor-integral-equation technique and the moment method.

ACKNOWLEDGEMENTS

The author wishes to express his sincere gratitude to his supervisors, Professors S.S.Stuchly and M.A.Stuchly, for their guidance throughout the course of this research.

Thanks is due also to other staff members involved in the project, A.Kraszewski, D.Adamski, G.Hartsgrove , and S.Symons.

Special thanks is given to my wife, Susan, and my parents for their encouragement and support during the course of my graduate studies.

LIST OF SYMBOLS

E-field	Electric field
EM	Electromagnetic
$\|E_T\|$	Magnitude of the Total Electric Field (V/m)
f	Frequency (Hz)
H-field	Magnetic Field
$H_n^{(2)}$	Hankel Function of the 2nd Kind
J_n	Bessel Function of the 1st Kind
J_n'	First Derivative of the Bessel Function of the First Kind
k_o	Free Space Wave Number
k	Propagation Constant in the Medium
l	Cell Size (m)
MW	Microwave
P	Absorbed Power Density in the Medium (W/m^3)
RF	Radio-frequency
RW	Radiowave
SAR	Specific Absorption Rate (W/kg)
S	Specific Heat Capacity of the Medium (J/kg-°C)
T	Temperature (°C)
t	Time (s)

TE	Transverse Electric Field
TM	Transverse Magnetic Field
Y_n	Bessel Function of the 2nd Kind
Y_n'	First Derivative of the Bessel Function of the 2nd Kind
ε_o	Free Space Permittivity (F/m)
ε	Permittivity of the Medium (F/m)
ε'	Dielectric Constant of the Medium
ε''	Loss Factor of the Medium
λ_o	Free Space Wavelength at a Certain Frequency (m)
λ	Wavelength in the Medium at a Certain Frequency (m)
μ_o	Free Space Permeability (H/m)
ρ	Density of the Medium (kg/m^3)
ω	Angular Frequency (rad/s)
σ	Conductivity of the Medium (S/m)

CONTENTS

LIST OF TABLES

LIST OF FIGURES

Chapter 1

INTRODUCTION

1.1 GENERAL

Radiowaves (RW) and microwaves (MW), as part of the electromagnetic (EM) spectrum, have found numerous and continuously growing uses in various fields. Applications include communications, transportation, domestic, medical, and industrial uses. In some of those applications, humans are exposed to EM radiation of various intensities. RW and MW radiations when interacting with biological bodies undergo complicated changes due to reflection, refraction, and diffraction. These changes are strongly dependent upon the electrical properties of the biological body; the physical properties such as frequency, intensity, and polarization of the exposure field, and the surrounding environment of the body such as the presence of a conducting object and other reflecting surfaces.

In order to study the biological effects of EM radiation, it is important to find the distribution of the absorbed energy in the biological body. A basic universally accepted parameter, which specifies the rate at which the energy is absorbed by a unit mass of the exposed body (i.e. dose rate

), is called the Specific Absorption Rate (SAR) expressed in watts per kilogram. The value of SAR obtained by dividing the total absorbed power by the mass of the body is called the average SAR. The notation (SAR) used in this thesis is referred to as the local SAR which is the ratio of the power deposited in a small volume of the absorbing body to the mass of that volume (Durney [14]). For steady-state sinusoidal fields, the SAR is calculated from the following equation:

$$SAR = \frac{1}{2}\frac{\sigma}{\rho}|E_T|^2 \quad W/kg \qquad (1)$$

where σ is the tissue conductivity in S/m,

ρ is the density of the tissue in kg/m^3,

$|E_T|^2$ is the square magnitude of the total electric field in $[V/m]^2$.

1.2 STATE OF THE ART

There are generally two basic approaches of obtaining dosimetric data for biological bodies. These are the theoretical dosimetry and experimental dosimetry. Most of the work in the theoretical and experimental dosimetries have concentrated on the plane wave, far-field irradiation conditions because of the simplicity of analysing such exposures both numerically (Chen and Guru [10]) and

experimentally (Hagmann et al. [21]). Recently, some researchers have analysed theoretical models exposed to the near-field of simple sources such as short electric and magnetic dipoles (Chatterjee et al. [8] & [9], Hizal & Baykal [23], Iskander et al. [25], and Lakhtakia et al. [27]).

1.2.1 Theoretical Dosimetry

The main advantage of the theoretical approach is that the SAR distribution in the simulated objects with a nonuniform permittivity distribution can be calculated, whereas in the experimental approach, experiments can only be performed on homogeneous or multilayered models. Solving Maxwell's equations for an actual human body is prohibitively difficult. The earliest calculations of SAR distribution were performed for simple models such as a planar slab, sphere and infinite cylinder, which are easy to analyse mathematically. Later, with the development and use of digital computers, several more complex models such as the prolate spheroid, ellipsoid and other irregular shaped models, such as a block model of an average man, were analysed. A summary of the theoretical methods for calculating the power absorption in biological models of the human body under plane wave irradiation is given in Table 1.

There are two major techniques which have been used, namely, analytical and numerical. The main difference between the two techniques is that in the analytical technique, the data is obtained by solving Maxwell's equations analytically, while the numerical technique is based on solving a large system of simultaneous equations by matrix inversion or other iterative techniques. The major drawback of the analytical technique is that only simple-shaped models, which simulate very approximately the shapes of the human body, can be analysed, while the major drawback of the numerical technique is that it requires long computations and a large computer memory size to calculate the numerical results with reasonable accuracy. However, the electrical properties of humans are so complicated that even in the numerical techniques, only a few parameters can be taken into account, and only approximate solutions can be obtained by using the theoretical dosimetry approach.

TABLE 1

A SUMMARY OF THE THEORETICAL METHODS

MODEL SHAPE	TECHNIQUES	FREQUENCY LIMITS	REFERENCES
Multilayered Semi-infinite Homogeneous Plane-slab (R^1)	Optical refraction - Snell's Law	up to 3 GHz *	[3]
Multilayered Infinite Circular Cylinder (R^2)	Long Wavelength approximation; Separation of variables and Recursion equations; or Geometrical Optics approximation.	up to 10 GHz *	[7], [30], and [34]
Multilayered Sphere (R^3)	Separation of variables and Boundary conditions	up to 5 GHz **	[23], [35] - [36]
Prolate Spheroid (R^3)	Empirical curve fitting; Extended Boundary condition method; or Long Wavelength approximation	10 MHz to 10 GHz *	[16], [25], and [30]
Ellipsoid (R^3)	Long Wavelength approximation	up to 30 MHz *	[31]
Body-of-revolution (R^3)	Surface integral equation and moment method	up to 300 MHz *	[40] - [43]
Block (R^3)	Tensor integral equation and moment method	up to 500 MHz *	[10], [20], [21]

Specified frequency limits are according to calculations performed on

* an average man with weight = 70 kg, height = 1.75 m, and perimeter = 0.867 m or

** an average human head with radius = 0.08 m.

R^1 represents one dimensional model

R^2 represents two dimensional model

R^3 represents three dimensional model

1.2.2 Experimental Dosimetry

Experimental dosimetry is a method for obtaining data on the SAR distribution under any irradiation conditions. Data is obtained by measuring either the average or the local SAR values of animals or phantom models. The models are made of materials that simulate the electrical properties and, in some cases, the thermal properties of tissues and the shapes of the test body. Experiments cannot be performed on living human beings because of the invasive nature of the experiments.

The advantage of the experimental approach is that the SAR distributions in complicated human body shapes, which cannot be theoretically analysed, can be measured in similarly shaped phantom models. Furthermore, SAR distribution can be obtained in animal cadavers. EM biological effects can be extrapolated from the data measured for phantom models or animal cadavers. A summary of the experimental techniques along with their relative advantages and disadvantages is given in Table 2.

TABLE 2

COMPARISONS OF DIFFERENT TECHNIQUES IN EXPERIMENTAL DOSIMETRY

Measurement Technique	Dosimetric Data obtained	Advantages	Disadvantages	References
Infrared Thermographic Method	Average SAR and SAR Distribution	- provides detailed SAR distribution in short time by the use of a scanning thermographic camera	- requires high power sources - cannot be applied in full scale model measurement - readout after termination of exposure must be done quickly to avoid thermal diffusion - high cost of equipment	[17]
Calorimetric Technique	Average SAR only	- simple and inexpensive	- thermal radiation and convection affect the accuracy of the result	[14]
Noninterfering Thermometer Technique	Average SAR and SAR Distribution	- most accurate for measuring SAR distribution in the temperature regulated living bodies	- requires high power sources - the tissue phantom in this and the last two techniques has to simulate not only the electrical properties but also the thermal properties of the bodies	[12]
Differential Power Technique	Average SAR only	- accurate and easy	- size of the tested body is limited by the size of the exposure device	[6]
Nonperturbing Electric Field Probe Method	Average SAR and SAR Distribution	- can acquire accurate SAR distribution with minimal field perturbation - good spatial resolution - tissue phantom simulates electrical properties only - relatively low power of radiator ($\sim$ 10W) - probing of full scale models is possible	- requires calibrated nonperturbing probes	[5]

1.3 MOTIVATION

The main objective of this thesis is to evaluate and determine the practical limitations of experimental dosimetry. This is part of a project concerned with the mapping of the internal field distribution of a full scale model of man for different frequencies using a computer-based scanning system. As a first step, three simple-shaped models are analysed for plane wave irradiation, both theoretically and experimentally. The practical limitations of the experimental dosimetry can then be derived from the comparison between the two methods. In addition, the exact quantitative performance of the electric-field-probe technique can be evaluated. After the performance of the entire experimental dosimetry system has been measured, the internal field distribution of the full-scaled human model can be mapped within the experimental errors which are derived from the results obtained using simple models.

1.4 DEFINITION OF THE PROBLEM AND PURPOSE OF THE THESIS

Several theoretical techniques for solving the SAR distribution were reviewed in the previous section. Three models are chosen to be analysed here. Two theoretical analyses are implemented on a digital computer to calculate the SAR distributions of the cylindrical and block models under plane wave irradiation. The SAR distributions in the

circular cylindrical model of man from the analytical solution in the frequency range of 300 MHz to 1 GHz have never been compared with experiments, even though it has been proven by experiments (Massoudi et al. [30] & [34]) that this method can well determine the average SAR of the man-size models from frequencies of 400 MHz to 5 GHz. This technique is also believed to be the most efficient way to determine the SAR distribution as well as the average SAR in a frequency range of 500 MHz to 1 GHz.

It has been proven by Neuder [36] that there are good correlations between the theory and experiments on lossy dielectric spheres, therefore the spherical model is also analysed here in order to calibrate the experimental system.

Finally, a numerical technique in solving the SAR distribution of the block model is studied by comparing the numerical results with the experimental results. The advantage in choosing these three models is that their molds can be constructed easily by using minimal field disturbing materials.

Irradiations at frequencies of 350, 920 and 2450 MHz are chosen to be analysed because it has been proven [21] that head resonance occurs at a frequency of 350 MHz, while MW at frequencies of 915 and 2450 MHz are frequently used for industrial, scientific and medical applications.

This thesis will make the following contributions to the field of RF dosimetry:

- The experimental verifications of the theoretical calculations of the SAR distributions in the cylindrical and block models;
- The derivation of the practical limitations of the automated experimental dosimetry system;
- The calibrations of three triaxial electric field probes in different materials at frequencies of 350, 920 and 2450 MHz.

1.5 OUTLINE

The theoretical methods used for the calculations of the SAR distribution for sphere, circular cylinder, and block models and their computational and practical limitations are briefly described in chapter 2. The derivations for each model are given in the appendices. The numerical results of the SAR distribution are presented in Chapter 3. Chapter 4 describes the experimental procedures and materials which are used. The comparisons between the theories and the experiments are discussed in Chapter 5 with the conclusions and some suggestions for future work.

Chapter 2

THEORETICAL ANALYSES

2.1 GENERAL

Several methods have been developed to calculate the electric field distribution in models of different shapes that simulate the human body or its parts. Three models, namely cylindrical, spherical, and block model, are analysed here using three different methods. In all cases, plane wave irradiation is assumed. The main reason for choosing the three specific models is that their shapes and plane wave irradiation conditions are easy to analyse both theoretically and experimentally so that the resulting SAR distributions can be compared.

Brief descriptions of the numerical analysis for finding the electric fields induced inside each model irradiated by a plane wave are given in latter sections, while the computational steps and the detailed descriptions of the derivation of the field distribution for all three models are given in the following chapter and the appendices, respectively. The steady-state solutions are assumed to be time dependent as $e^{j\omega t}$ for all the cases. All three models are considered in free space.

The parameters which describe the electrical properties of the tissues are:

1. μ (H/m) is the tissue permeability, which describes the magnetic properties of the tissue. For most biological tissue, it is assumed to be equal to μ_o (free space) (H/m);

2. $\varepsilon/\varepsilon_o = \varepsilon' - j\varepsilon''$ is the tissue relative permittivity, where ε_o (F/m) is the free space permittivity, ε' is the dielectric constant, and ε'' is the loss factor;

3. $\sigma = \omega\varepsilon_o\varepsilon''$ (S/m) is the tissue conductivity, which relates the square of the magnitude of induced electric field (E-field) to the absorbed power in the tissue.

2.2 CYLINDRICAL MODEL

The infinite circular cylinder can simulate the middle section of the trunk, thighs or arms of the human body, when the wavelength of the incident field is small as compared to the size of the body. Due to the attenuation in tissues, the field interactions between different parts of the body become less significant as the frequency increases. Therefore the result of the simulation by the infinite cylindrical model will give a precise estimate of the SAR

distribution as well as the average SAR in different parts of the human body, at frequencies above 400 MHz (Massoudi et al. [34]). The SAR distribution and the average SAR in a cross section of a finite circular cylinder can also be estimated from the solution for an infinite circular cylinder with the same diameter when the cross section is far from the ends. In the middle section, the SAR distribution is only slightly disturbed by the end reflections.

The configuration of an infinite circular cylinder consisting of multiple layers of lossy dielectrics, under plane wave irradiation, is shown in Fig.1. The electric field distribution in such a model was analysed (Bussey & Richmond [7]) under the following conditions:

— The direction of the incident plane wave is normal to the cylinder axis. Taking this axis as a reference, the incident fields can be designated as:

  i) Transverse Magnetic (TM) mode, where the incident E-field vector is parallel to the cylinder axis;

  ii) Transverse Electric (TE) mode, where the incident E-field vector is perpendicular to the cylinder axis;

  iii) Arbitrary mode, where neither the magnetic nor the electric field are parallel to

the cylinder axis. The arbitrary mode can be represented as a vector sum of the TM and TE modes;

- The permittivity in each layer and along the cylinder axis does not change;
- The induced field vectors follow the direction of the incident field vectors, since the cylinder is infinitely long and the incident E- and H-fields (electric and magnetic fields) are tangential to the boundary;
- The field distribution does not change along the cylinder axis;
- The limitations on the diameter of the infinite circular cylinder as compared to the wavelength have not been analysed by Bussey and Richmond [7].

2.2.1 Transverse Magnetic (TM) Mode

The electric field vector in this mode is directed along the cylinder axis. The multilayered infinite circular cylinder is shown in Fig.1. The E-field outside the cylinder is equal to the sum of the series expansions of the incident plane wave of unit amplitude (first term) and the scattered field (second term). Since the incident E-field is along the

z direction, the expression for the E-field outside the cylinder is given by [7]:

$$E_z = \sum_{n=0}^{\infty} \left[e_n j^{-n} J_n(k_o r) + C_n H_n^{(2)}(k_o r) \right] \cos\phi \qquad (2)$$

where $e_n = 1$ for $n = 0$ or $e_n = 2$ for $n > 0$

$k_o = \omega\sqrt{\mu_o \varepsilon_o}$ is the free space wave number

C_n are the coefficients of expansion

j is the imaginary unit

J_n is the Bessel function of the 1st kind

H_n is the Hankel function of the 2nd kind

The induced fields in layer m, m=1,2,..,M, while M+1 is in free space, are given by [7]:

$$E_{z,m} = \sum_{n=0}^{\infty} \left[A_{mn} J_n(k_m r) + B_{mn} Y_n(k_m r) \right] \cos n\phi \qquad (3)$$

$$H_{\phi,m} = \left(\frac{k_m}{j\omega\mu_m} \right) \sum_{n=0}^{\infty} \left[A_{mn} J'(k_m r) + B_{mn} Y'_n(k_m r) \right] \cos n\phi \qquad (4)$$

where $k_m = \omega\sqrt{\mu_m \varepsilon_m}$ is the propagation constant of layer m

μ_m is the permeability of layer m

$\mu_m = \mu_o$ (free space) (H/m) is assumed in this thesis

ε_m is the permittivity of layer m

Y_n is the Bessel function of the second kind

J'_n is the derivative of the Bessel function of the 1st kind

Y'_n is the derivative of the Bessel function of the 2nd kind

The coefficients A_{mn} and B_{mn} can be found from the boundary conditions at the interface between layers m and m+1, namely, that the tangential components of electric field E_z (Eqn.3) and magnetic field H_ϕ (Eqn.4) are continuous. The expressions for the coefficients were derived from the recursion equations. The analyses are given in Appendix A.

2.2.2 Transverse Electric (TE) Mode

In this case the magnetic field vector is directed along the cylinder axis. The solution can also be found from a similar analysis as in the TM mode. It is derived in Appendix A. The H-field outside the cylinder is given by:

$$H_z = \sum_{n=0}^{\infty} \left[e_n j^{-n} J_n(k_o r) + C_n H_n^{(2)}(k_o r) \right] \cos n\phi \qquad (5)$$

and the resulting H- and E-fields in layer m are, respectively, given by:

$$H_{z,m} = \sum_{n=0}^{\infty} \left[A_{mn} J_n(k_m r) + B_{mn} Y_n(k_m r) \right] \cos n\phi \qquad (6)$$

$$E_{\phi,m} = \left(\frac{k_m}{j\omega\epsilon_m} \right) \sum_{n=0}^{\infty} \left[A_{mn} J'_n(k_m r) + B_{mn} Y'_n(k_m r) \right] \cos n\phi \qquad (7)$$

where M+1 is in free space.

2.2.3 Arbitrary Mode

When the incident electric field vector is at an angle with respect to the cylinder axis, the total induced electric field can be calculated by considering two orthogonal components, which can be evaluated using equations derived in the previous two sections.

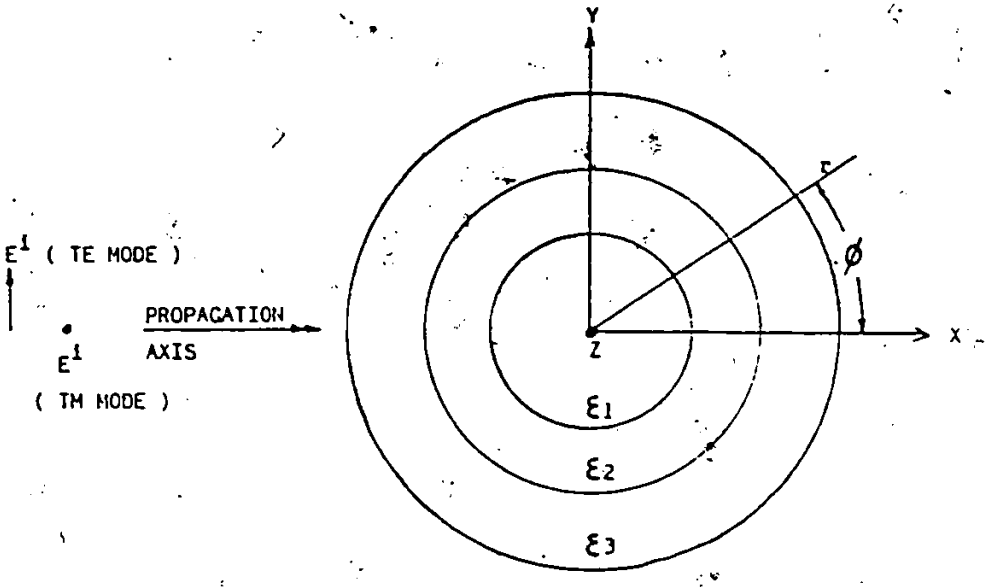

i.) SECTIONAL VIEW OF THE MULTILAYERED INFINITE CIRCULAR CYLINDER

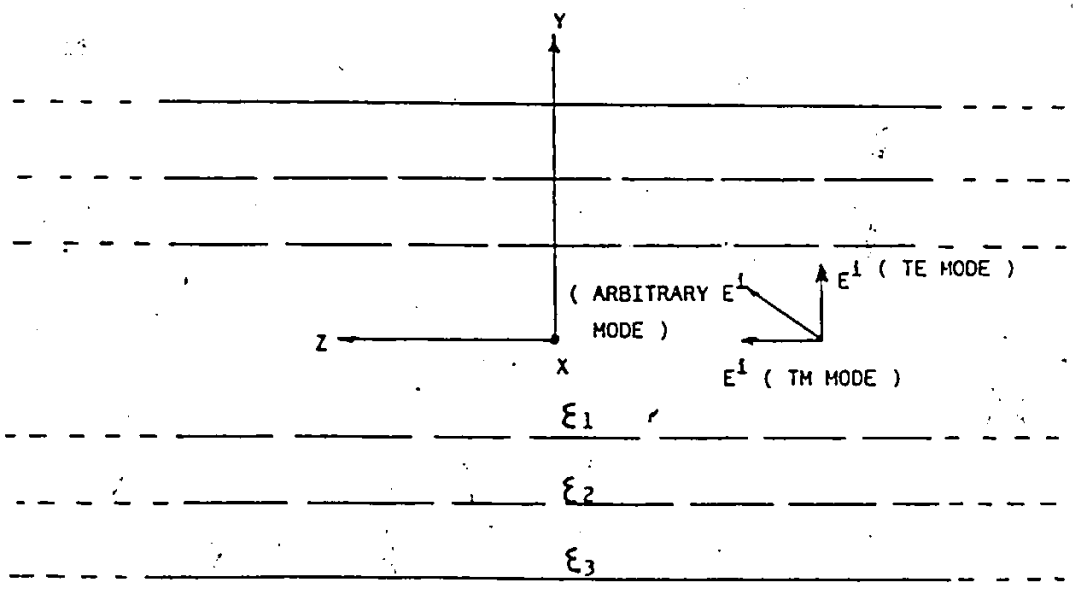

ii.) SIDE VIEW OF THE MULTILAYERED INFINITE CIRCULAR CYLINDER

Fig.1: TM, TE OR ARBITRARY MODAL PLANE WAVE INCIDENT ON A MULTILAYERED INFINITE CIRCULAR CYLINDER AND ITS CIRCULAR CYLINDRICAL COORDINATE SYSTEM

2.3 SPHERICAL MODEL

A computer program for finding the internal field distribution for a multilayered sphere irradiated by an EM plane wave was developed by Neuder [36] using the Mie method. The advantages of this technique are that it provides an exact analytical solution without any simplifications on the formulation and it can be used for a multilayered spherical model of any size. The major disadvantages of this technique are that it cannot be used for the models with nonhomgeneous properties within the layer and it is not a good model of the human body since the shape of the human body is very different from a sphere.

The theory is briefly described in this section while the limitations of the numerical technique as specified in the program are given in the next chapter. The general mathematical procedure for obtaining the wave equations inside or outside a sphere uses a technique of separation of variables and series expansions of the incident, internally induced and externally scattered fields in terms of spherical vector functions. Field continuity requirements at all interfaces, finiteness at the origin and appropriate field behaviour in infinity are applied to determine expansion coefficients for the induced and scattered fields. The configuration analysed here is shown in Fig.2. The incident fields for the plane wave irradiation in the rectangular coordinates are [36]:

$$\bar{E}_{inc} = \hat{i}_x E_o e^{j(k_o z - \omega t)} \qquad (8)$$

$$\bar{H}_{inc} = \hat{i}_y \frac{k_o}{\mu \omega} E_o e^{j(k_o z - \omega t)} \qquad (9)$$

These fields in the spherical coordinates can be expressed as:

$$\bar{E}_{inc} = E_o e^{-jwt} \sum_{n=1}^{\infty} j^n \frac{2n+1}{n(n+1)} \left[\bar{m}_{oln}^{(1)} - j\bar{n}_{eln}^{(1)} \right] \qquad (10)$$

$$\bar{H}_{inc} = \frac{-k_o}{\mu_o w} E_o e^{-jwt} \sum_{n=1}^{\infty} j^n \frac{2n+1}{n(n+1)} \left[\bar{m}_{eln}^{(1)} - j\bar{n}_{eln}^{(1)} \right] \qquad (11)$$

where

E_o is the amplitude of the incident E-field

k_o is the free space wave number

w is the angular frequency

μ_o is the free space permeability

$\bar{m}_{\xi ln}^{(1)}$ and $\bar{n}_{\xi ln}^{(1)}$ are the spherical vectors given in Appendix B.

The fields in a layer P are:

$$E_p = E_o e^{-jwt} \sum_{n=1}^{\infty} j^n \frac{2n+1}{n(n+1)} \left[a_n^p \bar{m}_{oln}^{(1)} - jb_n^p \bar{n}_{eln}^{(1)} + \alpha_n \bar{m}_{oln}^{(3)} - j\beta_n \bar{n}_{eln}^{(3)} \right] \qquad (12)$$

$$H_p = \frac{-k^p}{\mu_p w} E_o e^{-jwt} \sum_{n=1}^{\infty} j^n \frac{2n+1}{n(n+1)} \left[b_n^p \bar{m}_{eln}^{(1)} - j\bar{n}_{oln}^{(1)} + \alpha_n \bar{m}_{eln}^{(3)} + j\beta_n \bar{n}_{oln}^{(3)} \right] \qquad (13)$$

Coefficients a_n, b_n, α_n, and β_n are also given in Appendix B.

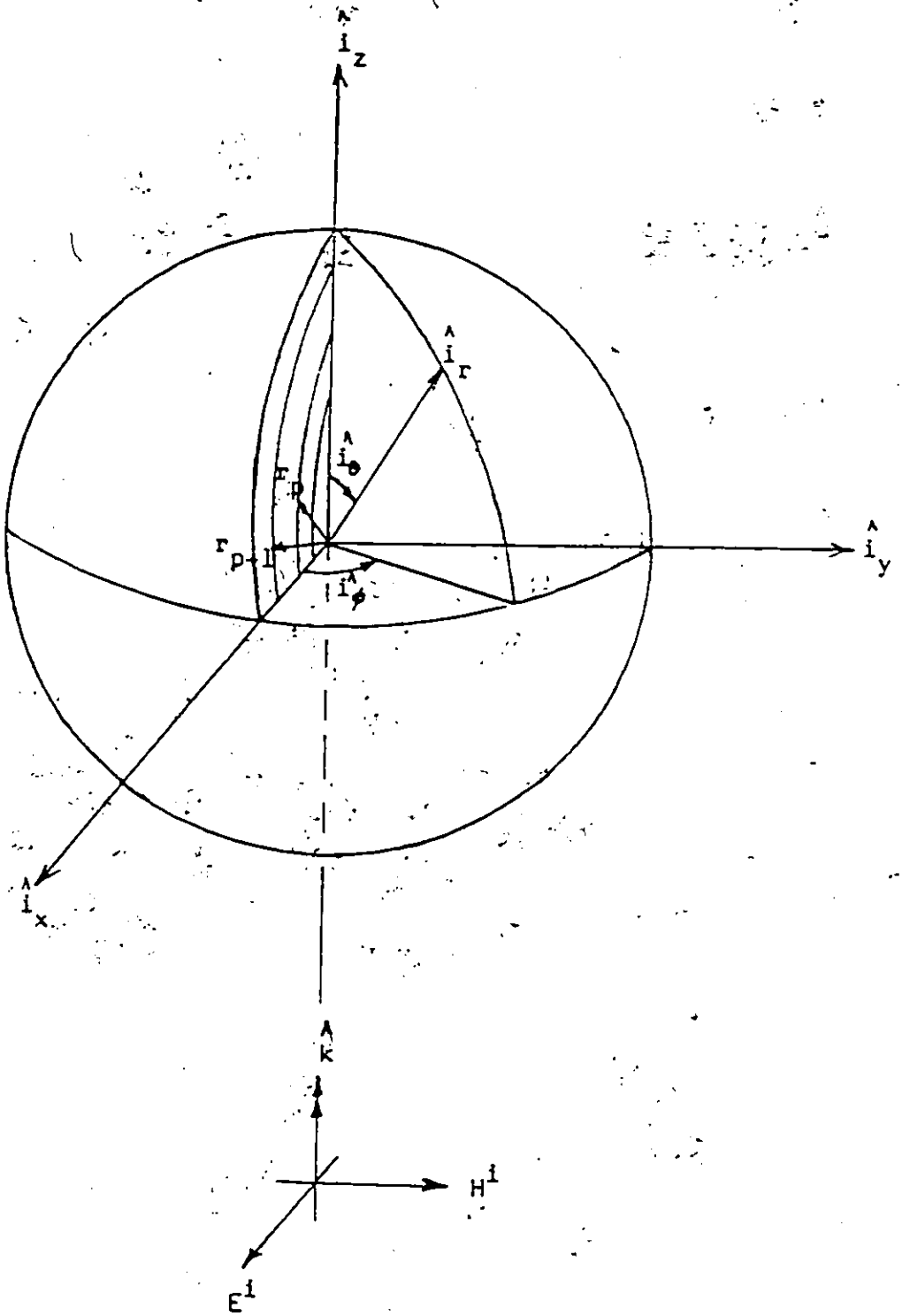

Fig.2: SYSTEM OF A MULTILAYERED SPHERE IN THE SPHERICAL COORDINATES

2.4 BLOCK MODEL

A general technique for finding the electric field inside an arbitrary biological body induced by an incident electromagnetic wave was developed by Livesay & Chen [29]. The method is based on formulating a tensor integral equation for the electric field inside the body. The equation is then solved numerically. This approach is more general than the two previous techniques. Electrically small bodies with nonhomogeneous properties and irradiated by a general incident field, such as a plane wave or a combination of plane waves, can be analysed by this method.

In the analysis, the body is subdivided into N homogeneous cells. The maximum cell size (l) for the moment method solution as derived in Hagmann et al. [18] is equal to $2.45/|k|$, where k is the propagation constant in the medium of the homogeneous cell, in order to validate the assumption that the E-field and permittivity are constant within the cell. However, this technique cannot efficiently determine the SAR distribution when there is a large cross section in the body having the rotational symmetry with respect to the incident H-field. The dimensions of this cross section are comparable to the wavelength in the tissue (λ) at a certain frequency. The impressed magnetic field will then excite a magnetic mode (i.e. an asymmetrical mode with respect to the centre and the propagation axis of the

body) of induced E-field in the body from the induction of eddy currents which flow along the propagation path of the incident wave in the body. To avoid this effect, the cross section of the body which is perpendicular to the H-field, must be small as compared to λ. Due to the cell size condition and computational limitations, the practical block model of man has been numerically analysed only up to a frequency of 500 MHz (Chen & Guru [10]).

When a finite heterogeneous biological body with a dielectric constant $\varepsilon'(r)$ and a conductivity $\sigma(r)$ is irradiated by an EM plane wave as shown in Fig.3, an electric field $E(r)$ is induced inside the body and an EM wave is scattered outside the body. This scattered field can be represented by replacing the body with an equivalent free space current density J_{eq} , which is bounded within the volume of the replaced body [29]:

$$J_{eq}(r) = \left[\sigma(r) + \frac{jw}{\varepsilon_o}(\varepsilon'(r) - 1) \right] E(r) = \gamma(r)E(r) \qquad (14)$$

Using the free-space tensor Green's function $G(r,r')$, the scattered field $E^S(r)$ can be expressed in terms of J_{eq} as follows:

$$E^S(r) = PV\int_V J_{eq}(r')\, G(r,r')\, dV' - \frac{J_{eq}(r)}{3jw\varepsilon_o} \qquad (15)$$

where PV is the principal value of the integral as defined in Appendix C. The expression for the Green function G(r,r') is also given in Appendix C. The total field inside the body is given by:

$$E(r) = E^{i}(r) + E^{s}(r) \qquad (16)$$

Substituting Eqn.(15) into (16) results in:

$$\left[1 + \frac{\tau(r)}{3jw\varepsilon_o} \right] E(r) - PV\int_V \tau(r')E(r')G(r,r')dV' = E^{i}(r) \qquad (17)$$

The integral equation (17) can be transformed into the matrix equation (18) by using the moment method:

$$\begin{bmatrix} [G_{xx}] & [G_{xy}] & [G_{xz}] \\ [G_{yx}] & [G_{yy}] & [G_{yz}] \\ [G_{zx}] & [G_{zy}] & [G_{zz}] \end{bmatrix} \begin{bmatrix} [E_x] \\ [E_y] \\ [E_z] \end{bmatrix} = - \begin{bmatrix} [E_x^i] \\ [E_y^i] \\ [E_z^i] \end{bmatrix} \qquad (18)$$

where [G] is a 3Nx3N coefficient matrix relating the three rectangular components $[E_x]$, $[E_y]$ and $[E_z]$ of the total field to those $[E_x^i]$, $[E_y^i]$, and $[E_z^i]$ of the incident field. The coefficient matrix [G] is defined in Appendix C. The formulas for finding the coefficient matrix as given in Appendix C were originally developed by Livesay and Chen [29]. The method employs a pulse function for expansion:

$$\bar{E} = \sum_{n=1}^{N} \bar{E}_n P_n \qquad (19)$$

where

$$P_n = \begin{cases} 1 & \text{inside the cell n} \\ 0 & \text{elsewhere} \end{cases}$$

and an impulse function for testing or by collocation method as shown in Appendix C:

$$\delta (x - x_m , y - y_m , z - z_m)$$

where the subscript m indicates the point at which the field is to be calculated.

The pulse function basis results in a constant value representing E within each homogeneous cell, while the impulse testing function enforces the integral at the centre of each cell so that the calculated E values are representative of the cell centres. The volume integral in [G] is calculated approximately by integrating the function over the volume of a sphere. The volume and the centre of the sphere are equivalent to those of the cell, therefore the solution is valid only if the cell shape is not very different from a sphere. The cubical cell shape is used in this thesis for computational convenience. The derivation is given in Appendix A.

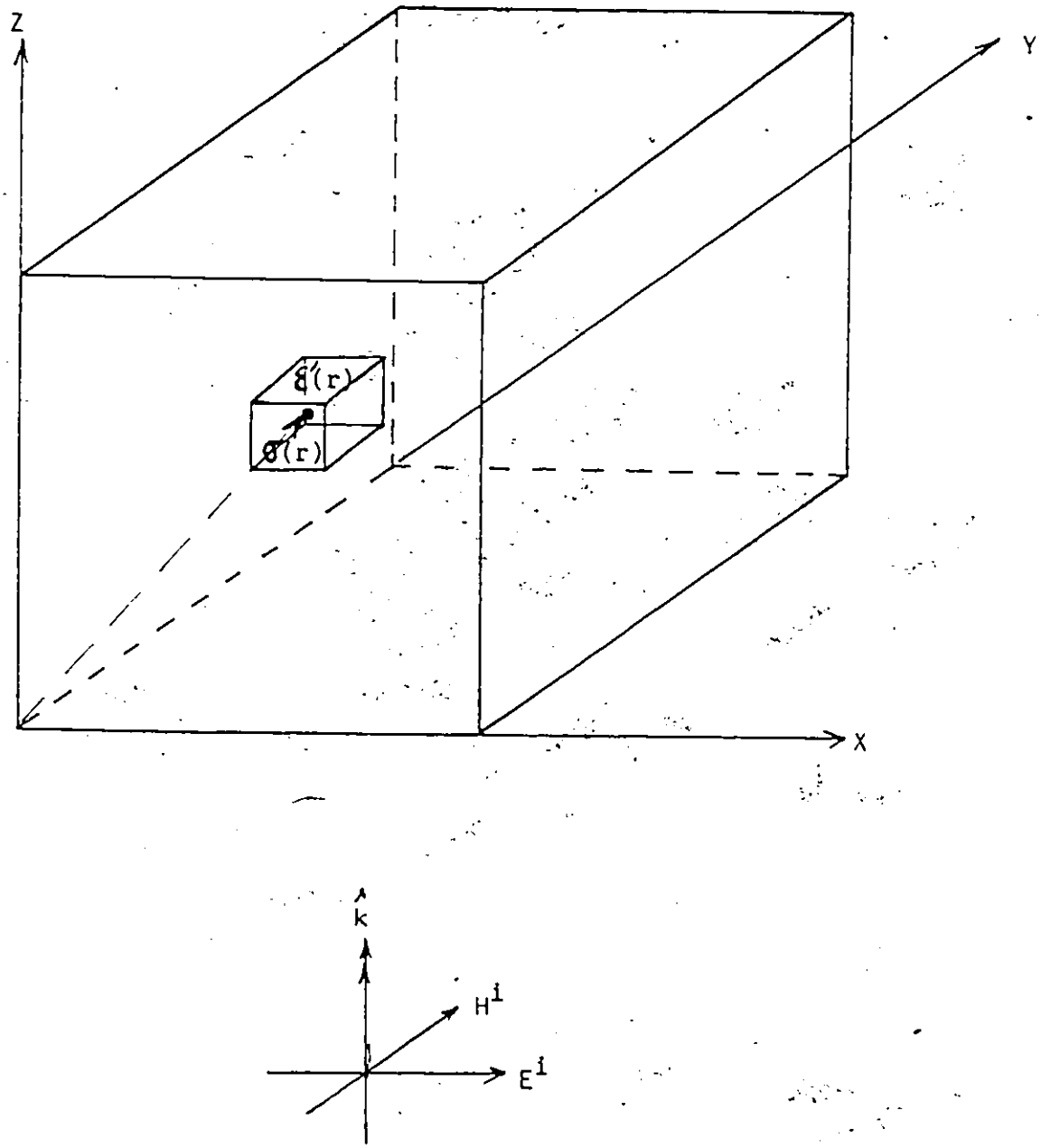

Fig.3: A BLOCK WITH A DIELECTRIC CONSTANT $\varepsilon'(r)$ AND A CONDUCTIVITY $\sigma(r)$ ILLUMINATED BY A PLANE WAVE IN THE RECTANGULAR COORDINATES

Chapter 3

THEORETICAL RESULTS

3.1 CYLINDRICAL MODEL

The numerical calculations of the total induced fields inside the cylinder in both TM and TE modes were implemented on a digital computer using the Fortran language and double precision with the following steps to perform the calculations:

1. Definition of the problem:

   i) the number of layers;

   ii) the outer radius of each layer;

   iii) the relative complex permittivity of each layer;

   iv) the number of desired observation points in the radial direction;

   v) the number of desired observation points in the angular direction ;

2. Initiation:

   The unnormalized amplitudes in the first layer from [7] are:

   $$A'(1,n) = (1.,0.)$$

B'(1,n) = (0.,0.) ;

3. Computation:

   i) Find the denormalization constants from Eqn.A-11 for TM mode or Eqn.A-14 for the TE mode;

   ii) Find the unnormalized amplitudes in the outermost layer from the recursion equations (Eqn.A-6), and from Eqns.A-9 and A-10;

4. Solution:

   i) Use Eqns.3 or 6 to find the total induced electric field for the given observation points for the TM or TE modes, respectively;

   ii) Calculate E or H fields in the outermost boundary both from the inner layer and the outer space for TM or TE modes, respectively, in order to check if they are equal.

Limitations on the calculation for double layer models:

— $|k|R < 22.8$, to avoid the large values of the Bessel functions; where R is the outermost radius;

— $|k|r > 1.87$, to avoid divergence of the Bessel functions in the zone near the cylinder origin; where r is the radius of the observation point;

- Since the field distribution inside the cylinder is symmetrical with respect to the propagation axis, E-fields are calculated only for observation points in one semicircular section of the cylinder;

- Maximum number of layers is five. However, this limit can be expanded by changing the array size (n) of the relative permittivity ET(n), as defined in the computer program;

- Maximum of twelve terms in the sum of the series of Bessel functions are used. Usually the sum of four or five terms of the Bessel series will converge with the displacement norm:

$$\|\Delta\| = |\Delta F| / |F| < 10^{-7} ,$$

where

$|\Delta F|$ is the modulus of the difference between the old and the new solutions,

$|F|$ is the modulus of the old solution.

The average SAR of the infinite circular cylindrical models of an average man and a rat have been numerically analysed by Massoudi et al. [30]. The results have been compared with experiments. They have proven that the numerical and experimental results agree very well when the

diameter of the models is larger than $0.3\lambda_o$ and the diameter to length ratio of the models is smaller than 0.13, where λ_o is the free space wavelength. These limits are derived from the results on [30]. The sizes of 24.8cm in diameter and 1.83m in length corresponding to $0.29\lambda_o$ in diameter at a frequency of 350 MHz and diameter to length ratio of 0.14 of a finite circular cylinder are chosen to be analysed using the above conditions. These dimensions can also represent a cylindrical model of a man. The field distributions in some sections of this finite cylinder, including the middle section, should be very close to that of an infinite cylinder since the dimensions of this finite cylinder are close to the limits specified above.

The SAR and E-field distributions inside the circular cylinder, which has a permittivity equal to that of the average tissue, were calculated at a frequency of 350 MHz and for an incident power density of 1 mW/cm^2. The effect of the 5mm acrylic wall of the cylinder was also accounted for. The electrical properties of the cylinder are $\varepsilon' = 2.6$ for the wall, $\varepsilon' = 38.9$ and $\varepsilon'' = 53.5$ for the tissue phantom inside the cylinder.

The electric field intensities along and perpendicular to the propagation axis inside the cylinder are shown in Figs.4-7. Even though the field intensities in the region near the centre (i.e. radius r is less than $1.87/|k|$)

cannot be calculated, the result in that region can be extrapolated because of the field continuity condition. The field intensities must be decreasing towards the centre since the field intensities in both the TM and TE modes are decreasing from the sides towards the centre of the cylinder in the direction along and perpendicular to the direction of propagation. Comparing the field distributions for the TM and TE modes for the same irradiaton conditions one can conclude that the power absorbed for the TM mode is greater than that for the TE mode at a frequency of 350 MHz. The calculations on the SAR distribution in the cylinder having the same diameter but filled with muscle saline phantom cannot be performed since $|k|R > 22.8$, which causes computational instability.

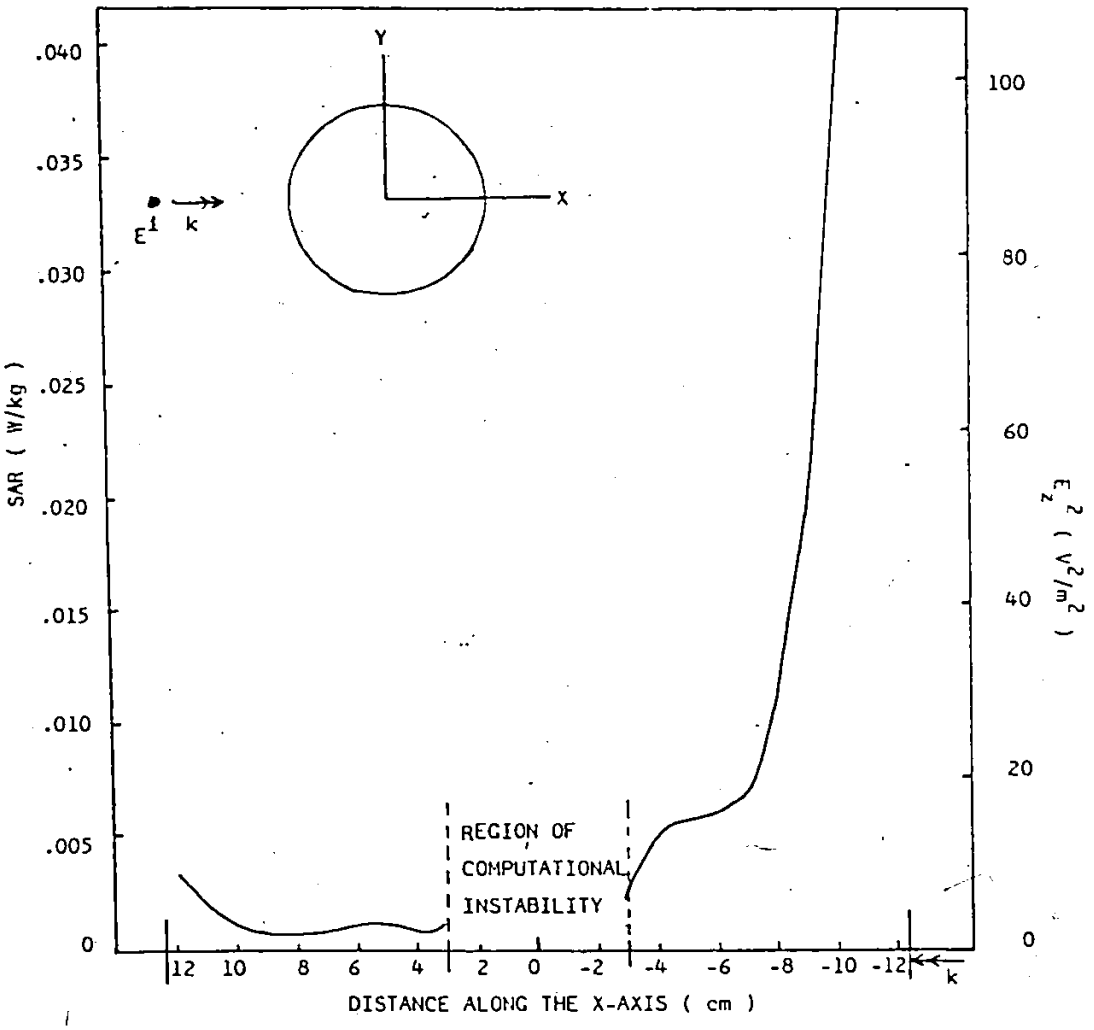

Fig.4: THEORETICAL RESULTS OF THE SAR AND ELECTRIC FIELD ACROSS AN INFINITE LOSSY DIELECTRIC CYLINDER FILLED WITH THE AVERAGE TISSUE PHANTOM ($\varepsilon' = 38.9, \varepsilon'' = 53.5$), TM Mode, f = 350 MHz, Incident Power Density = 1 mW/cm^2, Diameter = 24.8 cm, and Diameter/λ_o = 0.29; where the double arrow indicates the direction of incidence of the EM wave.

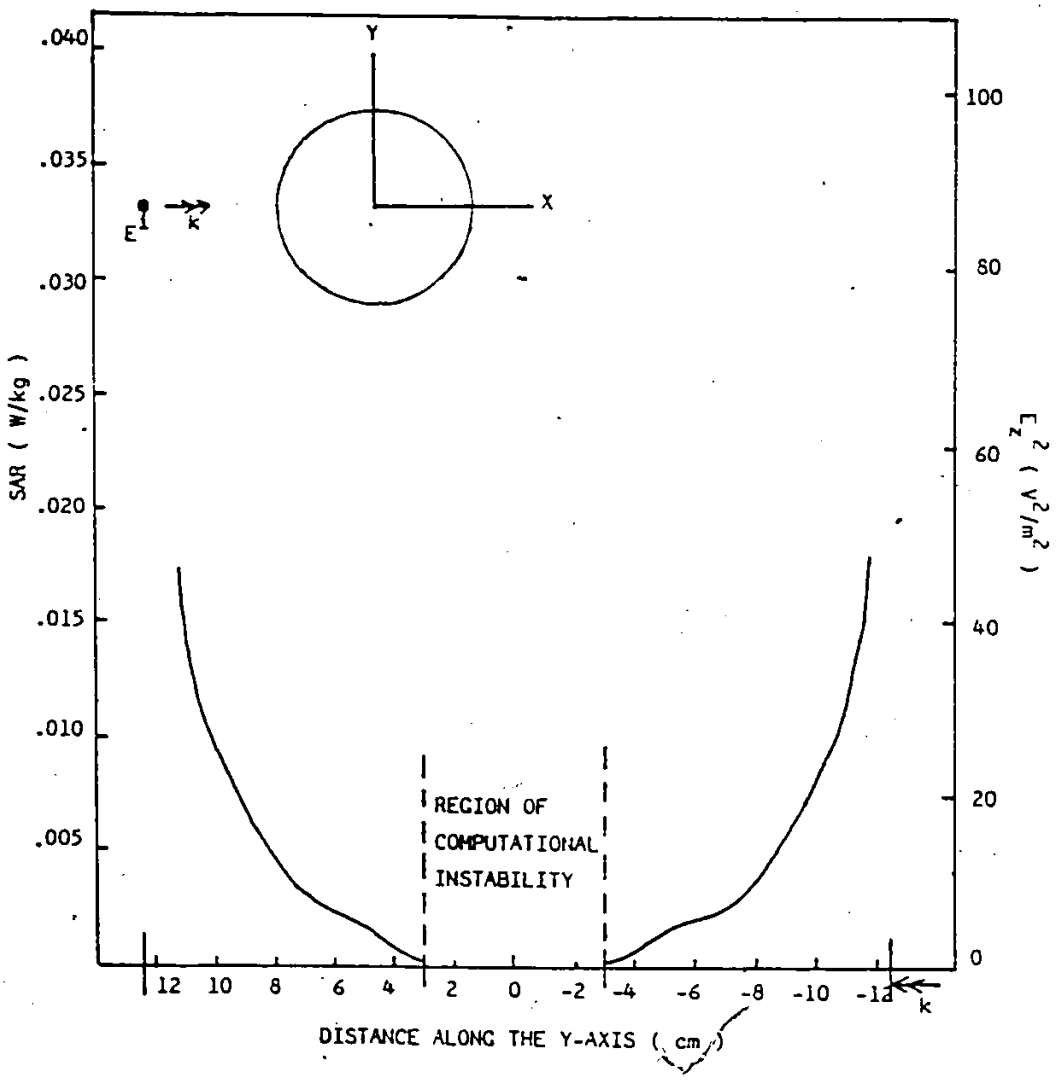

Fig.5: THEORETICAL RESULTS OF THE SAR AND ELECTRIC FIELD ACROSS AN INFINITE LOSSY DIELECTRIC CYLINDER FILLED WITH THE AVERAGE TISSUE PHANTOM ($\varepsilon' = 38.9$, $\Sigma'' = 53.5$), TM Mode, $f = 350$ MHz, Incident Power Density = 1 mW/cm^2, Diameter = 24.8 cm, and Diameter/λ_o = 0.29; where the double arrow indicates the direction of incidence of the EM wave.

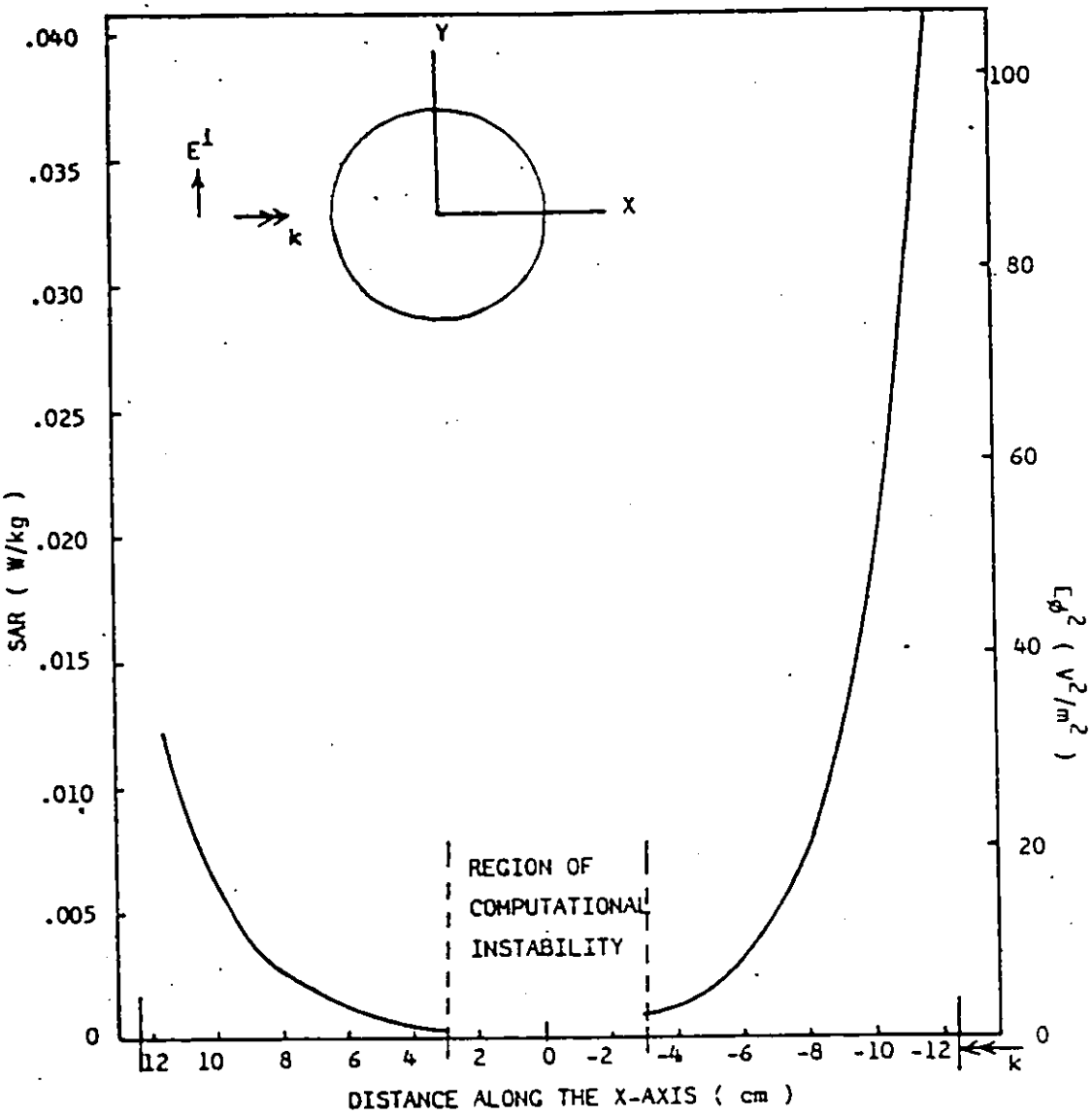

Fig.6: THEORETICAL RESULTS OF THE SAR AND ELECTRIC FIELD ACROSS AN INFINITE LOSSY DIELECTRIC CYLINDER FILLED WITH THE AVERAGE TISSUE PHANTOM ($\varepsilon' = 38.9$, $\varepsilon'' = 53.5$), TE Mode, f = 350 MHz, Incident Power Density = 1 mW/cm^2, Diameter = 24.8 cm, and Diameter/λ_o = 0.29; where the double arrow indicates the direction of incidence of the EM wave

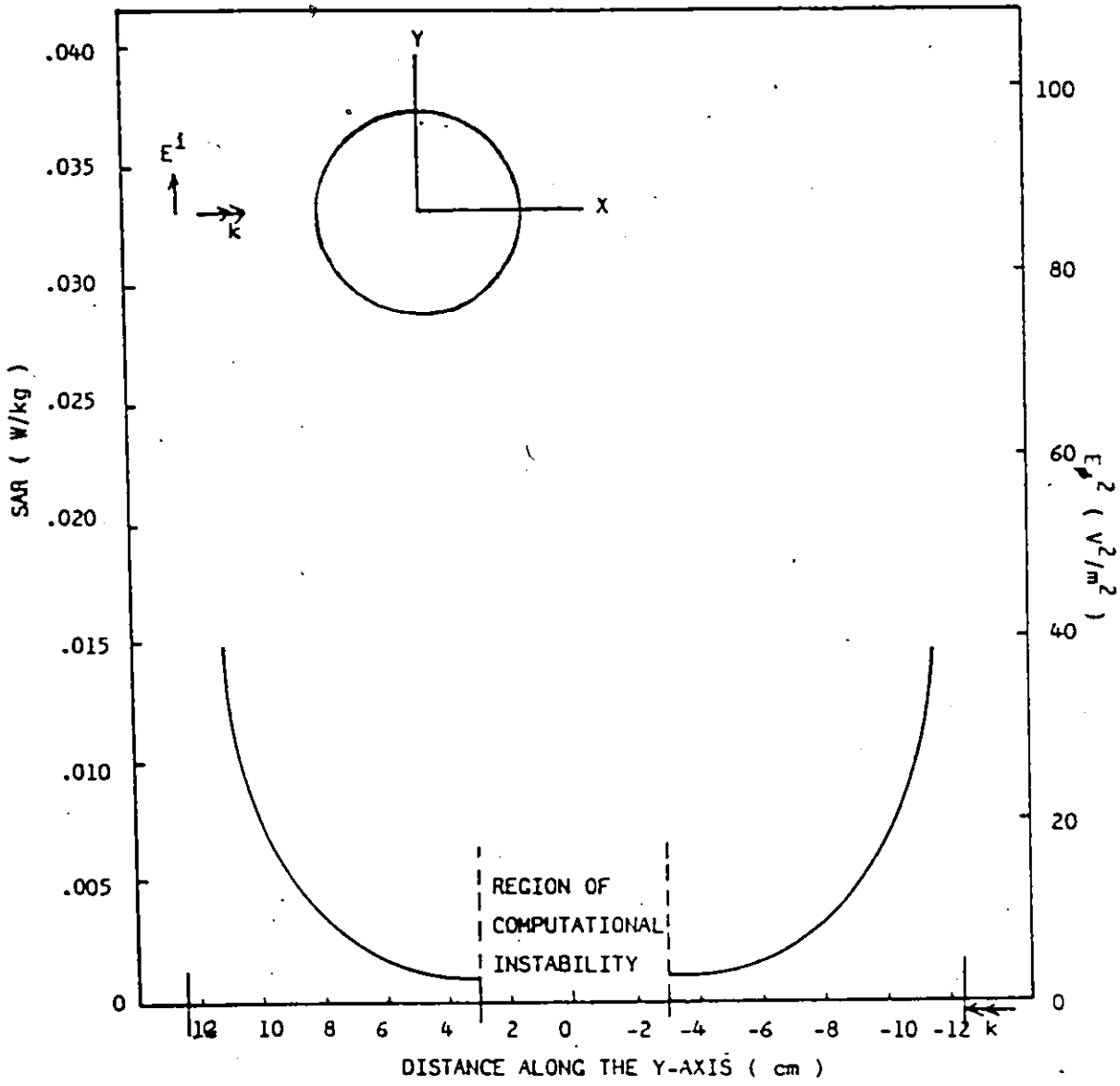

Fig.7: THEORETICAL RESULTS OF THE SAR AND ELECTRIC FIELD ACROSS AN INFINITE LOSSY DIELECTRIC CYLINDER FILLED WITH THE AVERAGE TISSUE PHANTOM ($\epsilon' = 38.9$, $\epsilon'' = 53.5$), TE Mode, $f = 350$ MHz, Incident Power Density = 1 mW/cm^2, Diameter = 24.8 cm, and Diameter/λ_o = 0.29; where the double arrow indicates the direction of incidence of the EM wave.

3.2 SPHERICAL MODELS

The computer program developed by Neuder [36] was provided courtesy of the Bureau of Radiological Health.

Restrictions of the program are as follows:

- Maximum number of layers is 10;
- Each layer is homogeneous;
- $|k|\, r < 90.83$, as derived from a homogeneous sphere; where r is the radius of the homogeneous sphere.

The computer program provides the results of induced electric and magnetic fields, local SAR, total power absorbed in the whole sphere and fractional power absorption by each layer of the sphere.

The local SAR and electric field intensity for three different sizes of homogeneous sphere having the following diameters: 16, 12, and 6.6 cm, and average and muscle tissue properties were calculated here at different frequencies. The reason for choosing these specific sizes is that 16-cm and 12-cm diameter spheres can simulate the human head (adult and child) while a 6.6-cm diameter sphere can simulate the hamster head. The results are shown in Figs.8-14 for an incident power density of 1 mW/cm^2. The SAR and E-field distribution along the Z axis of the 12-cm

diameter sphere at 2450 MHz for two values of the permittivity differing by 5% are shown in Fig.15.

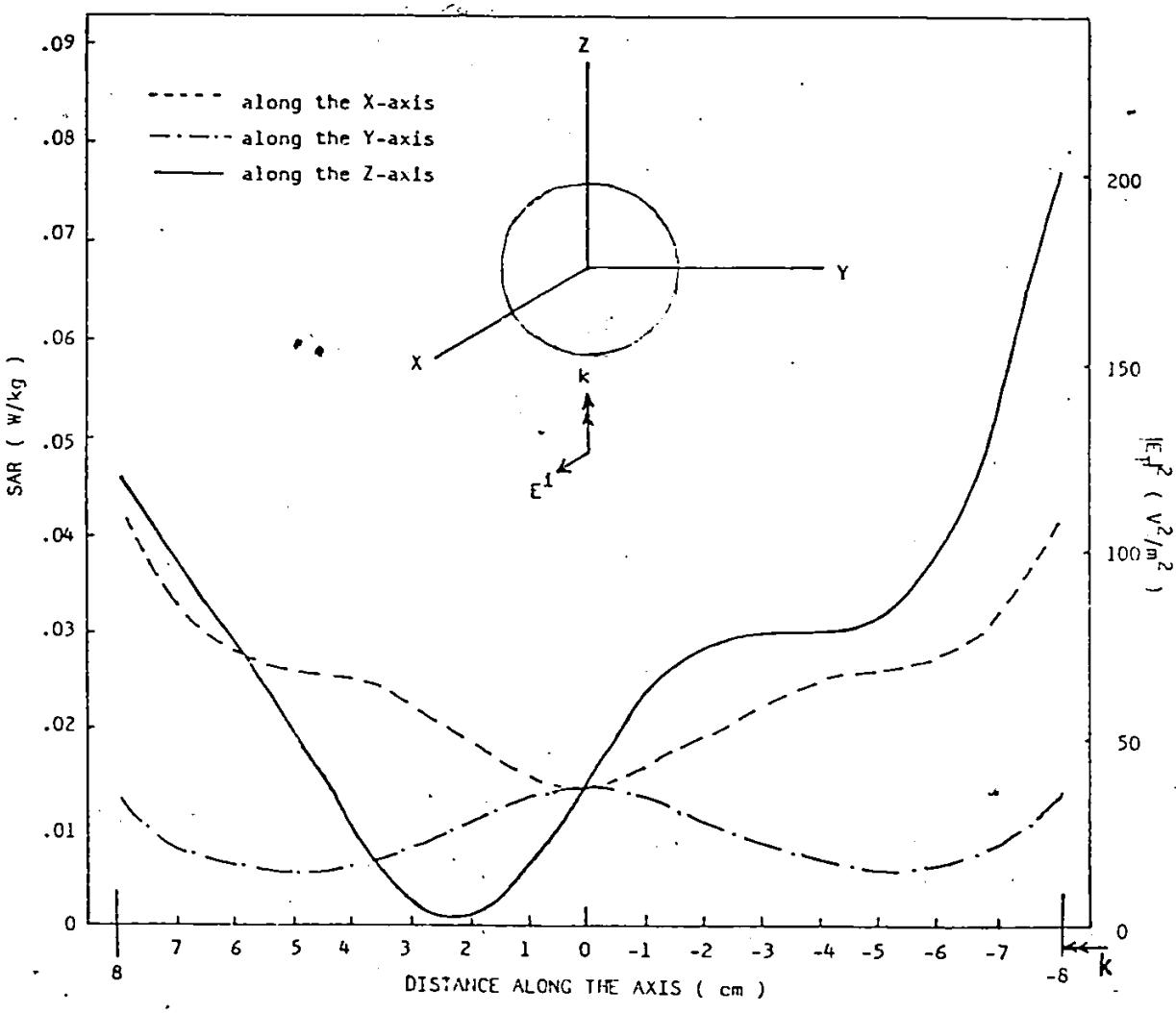

Fig.8: THEORETICAL RESULTS OF THE SAR AND ELECTRIC FIELD OF THE AVERAGE TISSUE PHANTOM SPHERE ($\varepsilon' = 38.9$, $\sigma = 1.04$ S/m, f = 350 MHz, Incident Power Density = 1mW/cm^2, Diameter = 16 cm, Diameter/$\lambda_0 = 0.19$, and Total Absorbed Power = 73.4 mW); where the double arrow indicates the direction of incidence of the EM wave along the Z-axis.

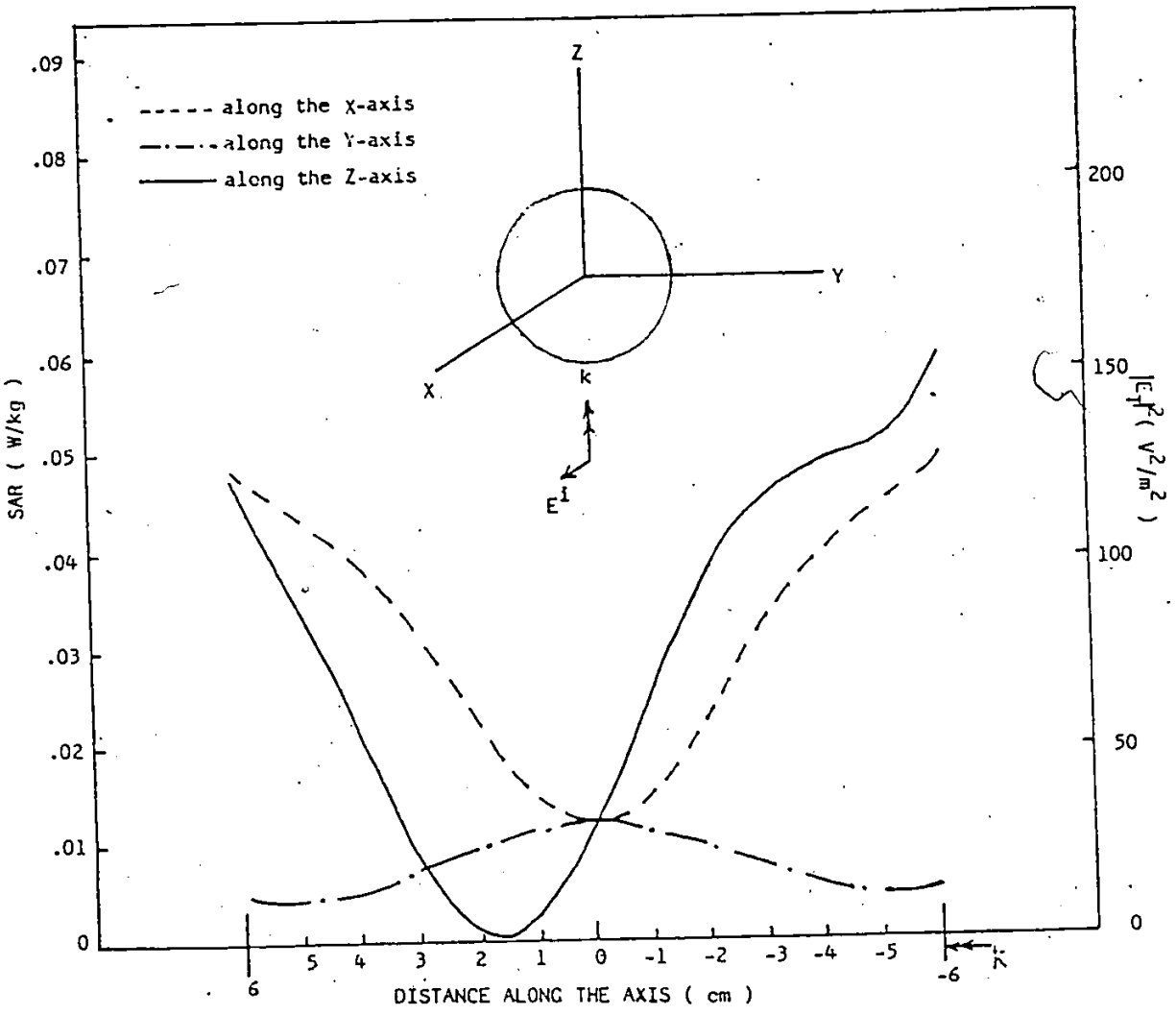

Fig.9: THEORETICAL RESULTS OF THE SAR AND ELECTRIC FIELD OF THE AVERAGE TISSUE PHANTOM SPHERE ($\varepsilon' = 38.9$, $\sigma = 1.04$ S/m, $f = 350$ MHz, Incident Power Density = 1mW/cm^2, Diameter = 12 cm, Diameter/$\lambda_o = 0.14$, and Total Absorbed Power = 34.8 mW); where the double arrow indicates the direction of incidence of the EM wave along the Z-axis.

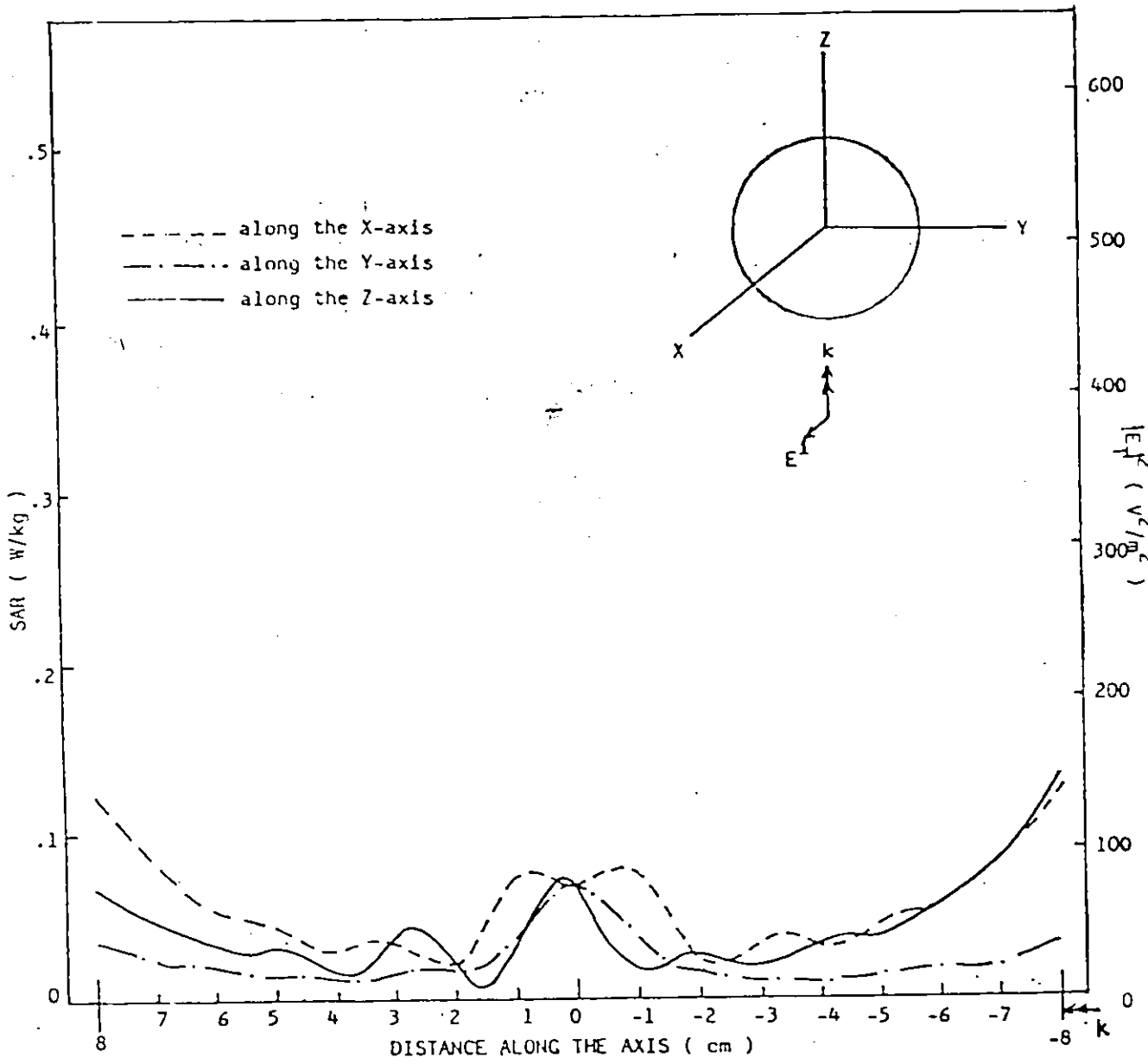

Fig.10: THEORETICAL RESULTS OF THE SAR AND ELECTRIC FIELD OF THE MUSCLE SALINE SPHERE ($\epsilon' = 76.0$, $\sigma = 1.58$ S/m, $f = 920$ MHz, Incident Power Density = 1 mW/cm^2, Diameter = 16 cm, Diameter/λ_o = 0.49, and Total Absorbed Power = 76.5 mW); where the double arrow indicates the direction of incidence of the EM wave along the Z-axis.

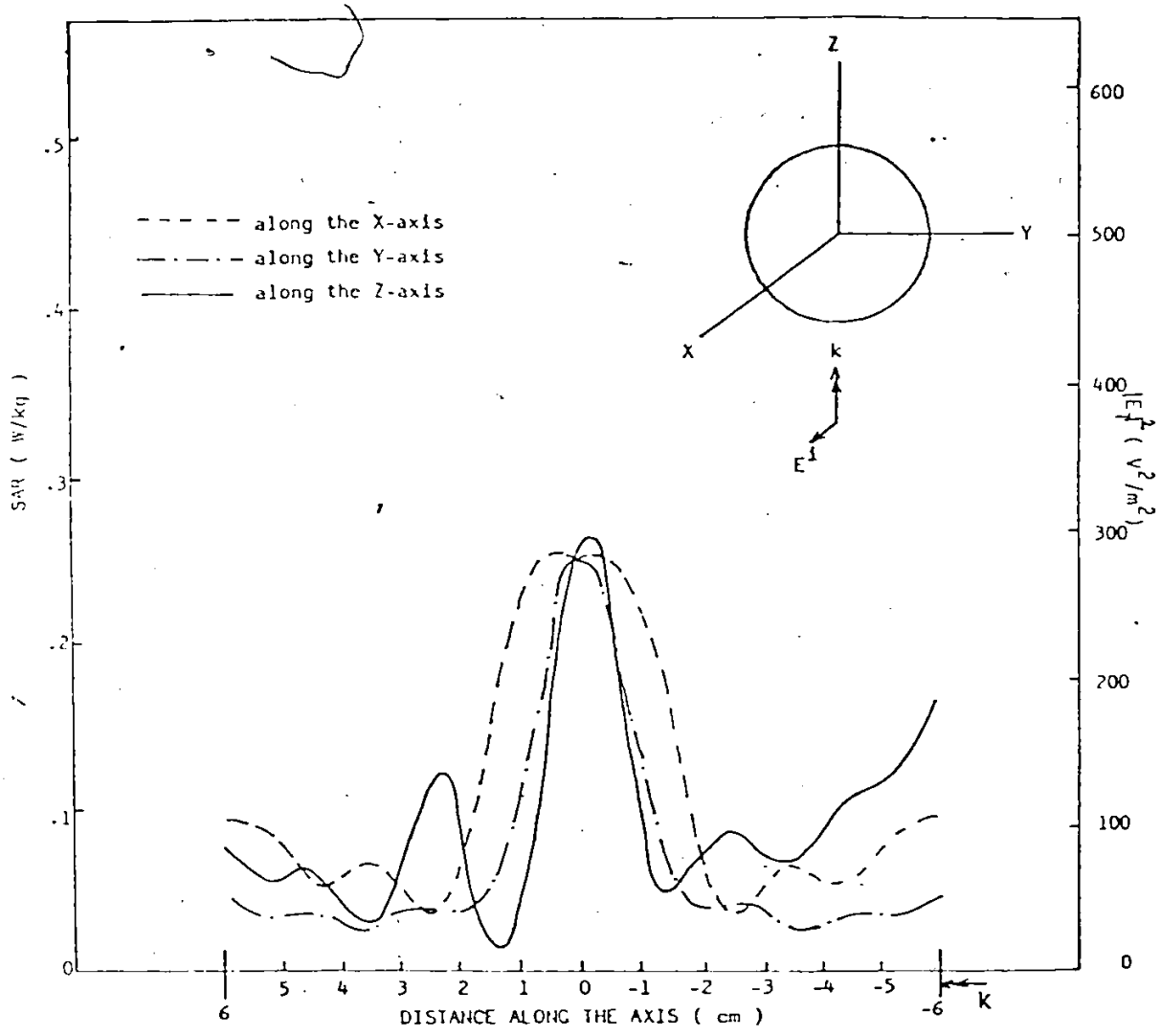

Fig.11: THEORETICAL RESULTS OF THE SAR AND ELECTRIC FIELD OF THE MUSCLE SALINE SPHERE ($\varepsilon' = 76.0$, $\sigma = 1.58$ S/m, $f = 920$ MHz, Incident Power Density = 1 mW/cm^2, Diameter = 12 cm, Diameter/λ_o = 0.37, and Total Absorbed Power = 49.7 mW); where the double arrow indicates the direction of incidence of the EM wave along the Z-axis.

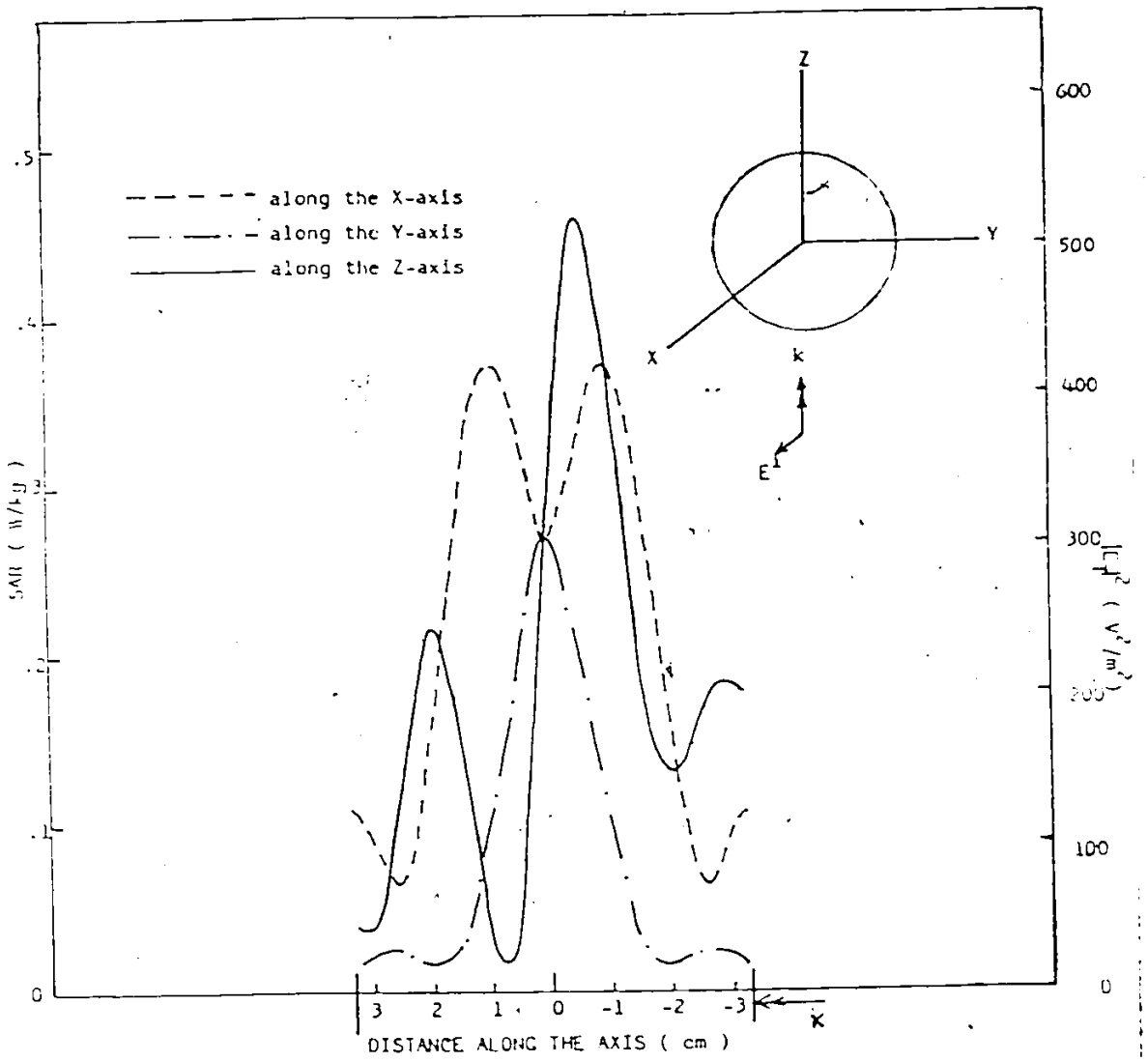

Fig.12: THEORETICAL RESULTS OF THE SAR AND ELECTRIC FIELD OF THE MUSCLE SALINE SPHERE ($\varepsilon' = 76.0$, $\sigma = 1.58$ S/m, f = 920 MHz, Incident Power Density = 1 mW/cm^2, Diameter = 6.6 cm, Diameter/λ_o = 0.2, and Total Absorbed Power = 12.9 mW); where the double arrow indicates the direction of incidence of the EM wave along the Z-axis.

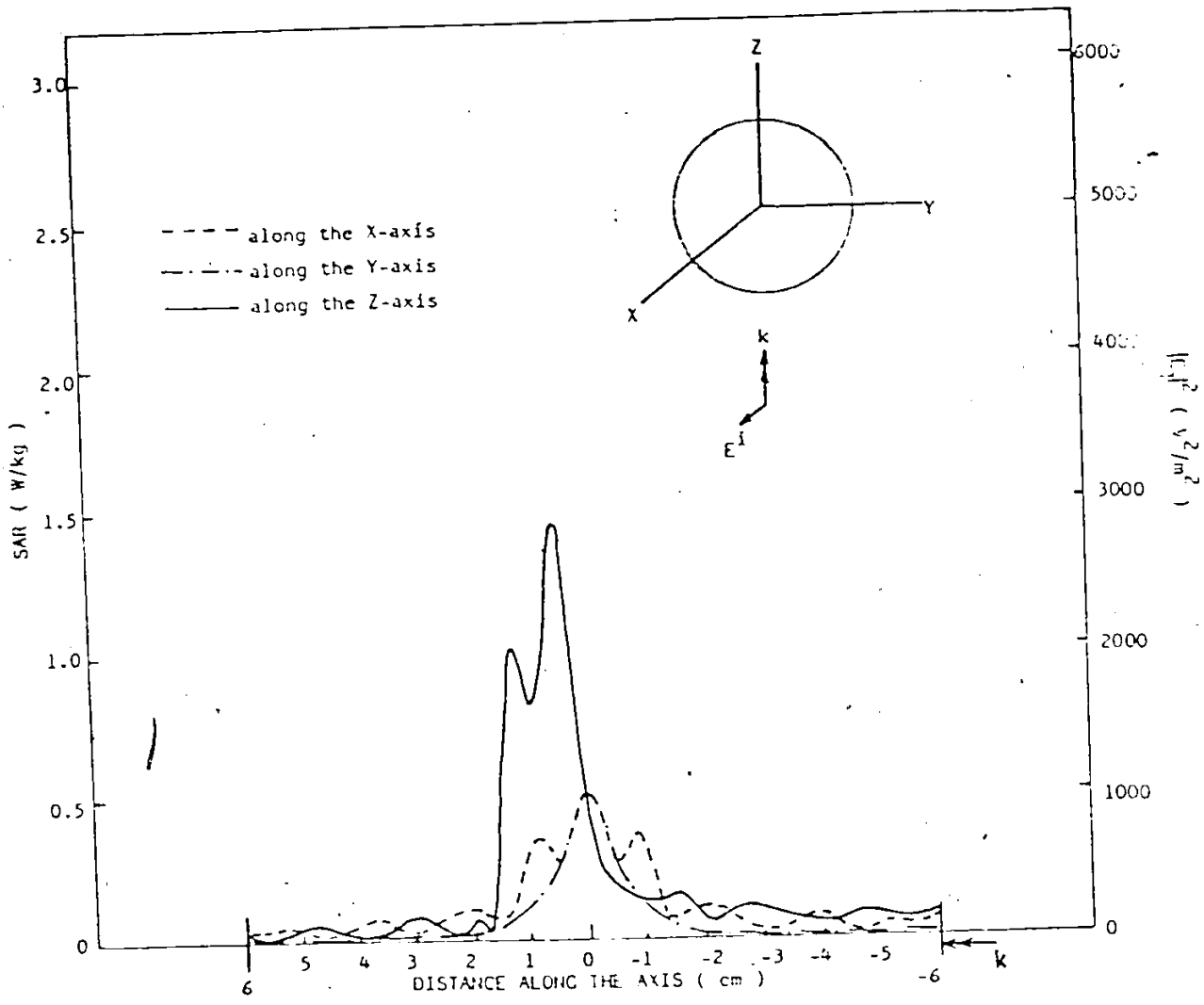

Fig.13: THEORETICAL RESULTS OF THE SAR AND ELECTRIC FIELD OF THE MUSCLE SALINE SPHERE ($\varepsilon' = 77.9$, $\sigma = 1.02$ S/m, $f = 2450$ MHz, Incident Power Density = 1 mW/cm^2, Diameter = 12 cm, Diameter/λ_o = 0.98, and Total Absorbed Power = 36.5 mW); where the double arrow indicates the direction of incidence of the EM wave along the Z-axis.

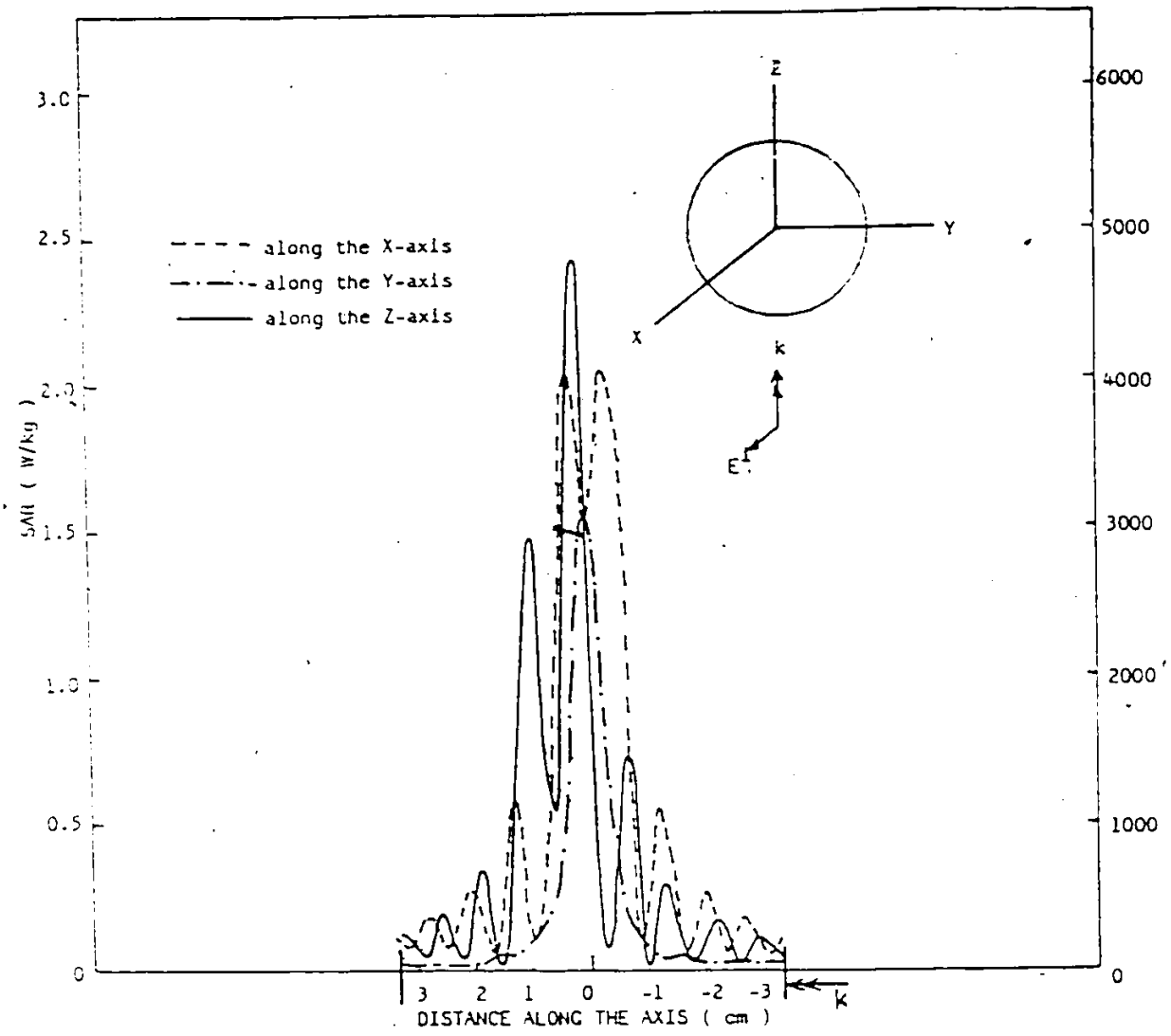

Fig.14: THEORETICAL RESULTS OF THE SAR AND ELECTRIC FIELD OF THE MUSCLE SALINE SPHERE ($\varepsilon' = 77.9$, $\sigma = 1.02$ S/m, $f = 2450$ MHz, Incident Power Density = 1 mW/cm^2, Diameter = 6.6cm, Diameter/λ_o = 0.54, and Total Absorbed Power = 36.5 mW); where the double arrow indicates the direction of incidence of the EM wave along the Z-axis.

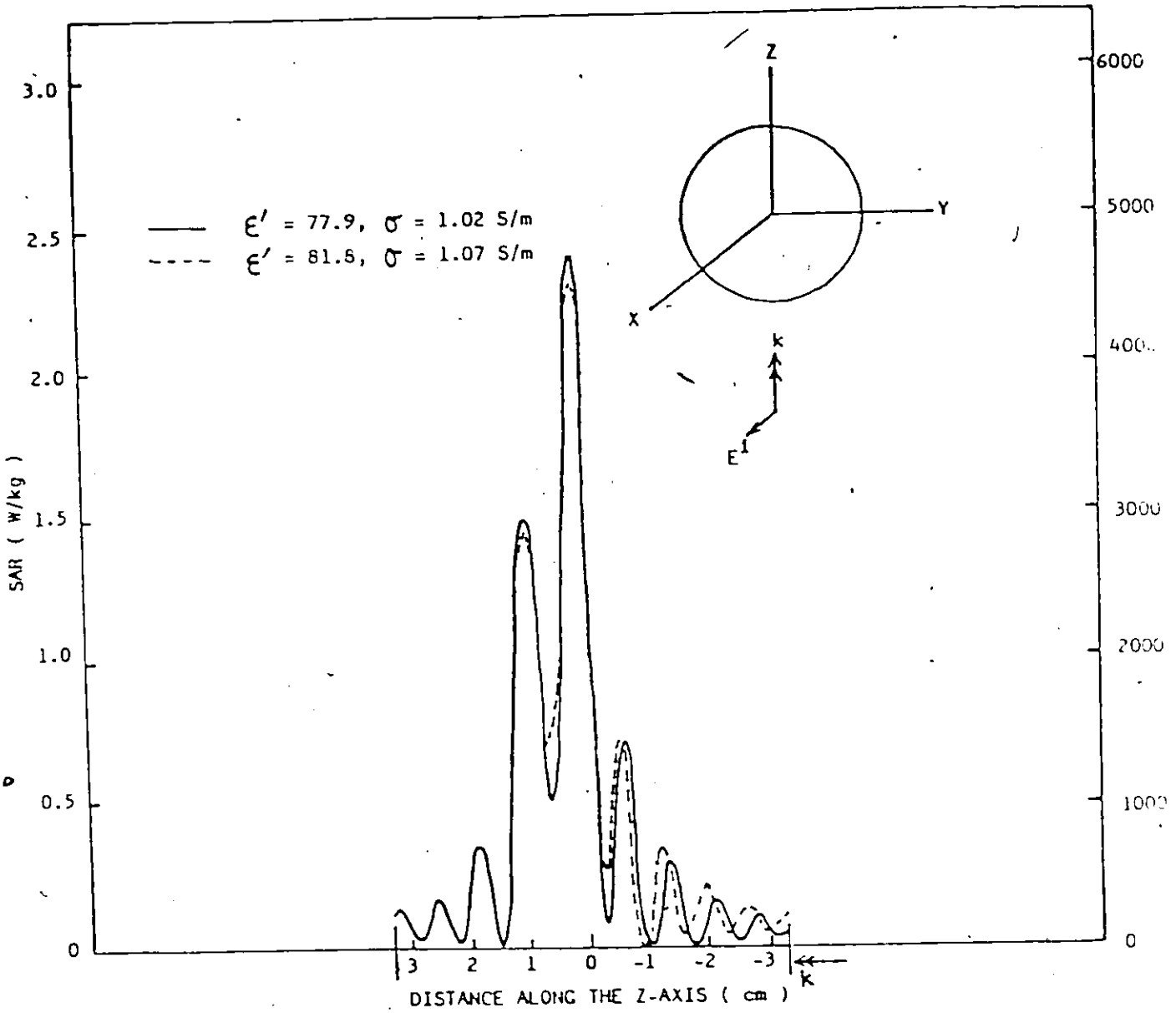

Fig.15: COMPARISON OF THE THEORETICAL SAR AND ELECTRIC FIELD DISTRIBUTION ALONG THE Z-AXIS OF THE MUSCLE SALINE SPHERE WITH AND WITHOUT +5% CHANGE IN THE PERMITTIVITY (Incident Power Density = 1 mW/cm^2, Diameter = 6.6 cm, Diameter/λ_o = 0.54); where the double arrow indicates the direction of incidence of the EM wave along the Z-axis.

The results of the calculations can be summarized as follows:

- For all frequencies, the total E-field along the propagation axis (Z-axis) and the axis parallel to the incident H-field (Y-axis) consists only of the component E_x that is parallel to the incident E-field vector, while the total field along the axis parallel to the incident E-field (X-axis) contains E_x and E_z components;

- There is less energy dissipated along the incident H-field axis (Y-axis) of the sphere as compared to that along the incident E-field (X-axis) and the propagation axis (Z-axis) where most energy is dissipated along the propagation axis;

- At a frequency of 350 MHz, peak SARs occur at the edge of the 16-cm (9.5 λ) and 12-cm (7.2 λ) spheres along the propagation axis, while at frequencies of 920 MHz and above, strong peak SARs occur near the centre of the 12-cm (greater than 21 λ) and 6.6-cm (greater than 12 λ) diameter spheres. The results shown in Fig.14 indicate that the E-field intensity near the centre of the 6.6-cm (30 λ) diameter sphere at a frequency of 2450 MHz is greater than the intensity of the incident field;

- The spheres of 16-cm (28λ) and 12-cm (21λ) diameter absorb more power at a frequency of 920 MHz than at a frequency of 350 MHz. The sphere of 6.6-cm (greater than 12λ) diameter absorbs approximately the same amount of power at frequencies of 920 MHz and 2450 MHz;

- A relatively small change (+5%) in the permittivity of the phantom tissue causes a significant change (-5.2% in the peak SAR) in the field distribution inside the sphere as shown in Fig.15.

3.3 BLOCK MODELS

The total fields in a block model in the matrix equation (18) were solved numerically by a computer program written in Fortran. The program consisted of the main program and five subprograms with the following steps:

1. Definition of the problem:

   i) the number of cells (n)

   ii) the array sizes of G(3n,3n), E(3n), and WA(3n)

   iii) the incident field

   iv) the frequency

v) the dielectric constant and conductivity for each cell

vi) the dimensions of the block

vii) the number of divisions on each side of the block;

2. Computation:

i) Calculate the rectangular coordinates of the cell centres;

ii) Check for the limit if $|k|\,l < 2.45$; where l is the cell size;

iii) Calculate the coefficients for the matrix [G] from Eqns.C-14 and C-16;

iv) Compute the decomposition of a rowwise permutation of matrix [G] and solve the system of matrix equations $[G][E] = -[E^i]$ by row equilibration and partial pivoting. This is done by calling an IMSL Library subroutine;

3. Solution:

The output provides the magnitudes of E in its complex form, and the sum of the square magnitudes of E in each cell;

Limitations on the numerical calculations:

- Cell shape must be cubical;
- Cell size $l < 2.45/|k|$ as derived by Hagmann et al. [18];
- Each cell must be homogeneous;
- For a 2 Mbyte computer memory storage, the maximum number of cells is 512.

The accuracy of the numerical results can be improved by applying:

- The symmetry of the model with respect to the incident field which can reduce the matrix size and therefore allow an increase in the number of cells of the block by a factor of two or four depending on the type of symmetry;
- The number of cells can also be increased by subdividing the cells one at a time into eight subcells and solving the induced field of the subcells which have been excluded from the body. The equivalent incident field of the subcell is the sum of the incident field of the subcell and its scattered field from the original N-1 cells.

In order to verify the accuracy of the calculated SAR distribution inside the block model by using the tensor-integral-equation technique and different number of cell subdivisions, 16-cm and 12-cm cubical blocks, and a 12cm X 12cm X 6cm block are chosen to be analysed. The sizes 16cm and 12cm are slightly larger than one wavelength (λ = 10.5cm) in the average tissue phantom at a frequency of 350 MHz. The results from these thick block models, as the thicknesses are comparable to λ , can also demonstrate that the accuracy of the solution can be affected by the impressed magnetic field. This is observed from the inconsistency of the calculated local SAR in the nearby cell regions arising from different number of cell subdivisions of the same block model. The SAR distributions for the above models and an incident power density of 1 mW/cm^2 at a frequency of 350 MHz are shown in Figs.16-18. Due to the symmetry with respect to the incident E-field vector, only one quarter of the sections of the SAR distributions are shown in the figures. For comparison, only the SAR distributions in a half of the cubes are shown in Figs.16-17. By comparing the values as shown in the darkened boxes of these figures, the calculated local SARs in one region deviate quite significantly from those in the nearby regions of different number of cell subdivisions. These results also show that the field distributions for the larger number of cell subdivisions deviate significantly

from those of the smaller number of cell subdivisions even when the cell size condition $|k|1 < 2.45$ is satisfied. The main cause of these results in thick models is that they both have a large cross section perpendicular to the incident H-field, therefore eddy currents are induced and flow along the long path in the blocks. This effect can be eliminated by subdividing the block into a very large number of cells. This has been shown using the same comparison on a thinner block as seen in the darkened boxes of Fig.18. There is some degree of consistency in the nearby regions of $|k|1 = 0.895$ and $|k|1 = 0.716$ when the number of subdividing cells increases from 256 to 500.

In order to eliminate the eddy current effect, some thinner blocks of thicknesses of 3.0cm, 4.0cm and 4.8cm, and cross section of 12X12 cm^2 are evaluated. The SAR distributions inside those thinner block models are given in Fig.20. The result using this technique with different cell sizes will be justified later by experiments.

The general comments resulting from the numerical calculations of the block models are as follows:

— The effect of induced eddy current on the thick (as compared to λ) block model can be eliminated by increasing the number of cell subdivisions. The product of the cell size and the thickness of the block as derived from the last result in Fig.18 must

be smaller than $0.065\ \lambda^2$, provided that $l < 2.45/|k|$, so that a good result will be obtained by the tensor-integral-equation technique and the moment method;

— The strongest component of the total E-field is along the direction of the incident E-field (E_x);

— The ratio of $|E_y|^2 + |E_z|^2$ to $|E_x|^2$ increases from the centre to the edge of the block, as shown in Fig.20 for the block sizes considered.

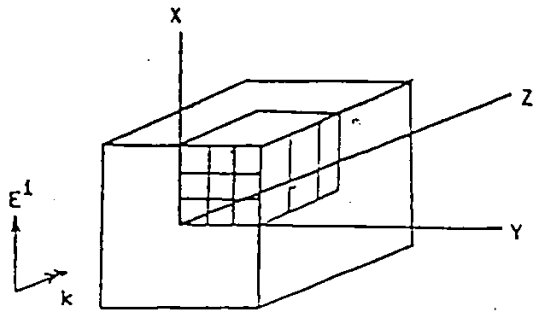

f = 350 MHz
ε' = 36.9
σ = 1.04 S/m
Incident Power Density = 1 mW/cm^2
$|k|$ = 59.6
l = cell size in m
λ = 10.5 cm

Dimensions: 16cm X 16cm X 16cm
Dimensions/λ : 1.52 X 1.52 X 1.52

10	11	17
24	23	29
30	30	37

1

19	22	18
33	25	21
40	27	23

2

49	52	39
60	44	24
72	45	21

3

$|k|l$ = 1.908

7	11	19
16	25	37
21	37	54

1

6	8	10
19	14	20
26	12	24

2

29	30	21
67	36	25
94	37	23

3

$|k|l$ = 1.59

9	12	18	26
22	29	52	55
34	44	87	86
39	50	106	101

1

5	8	13	16
8	13	38	38
9	10	50	58
10	10	59	68

2

8	11	13	12
27	18	22	20
44	16	10	20
58	21	8	21

3

19	21	26	20
50	34	33	27
77	43	25	25
98	53	27	26

4

$|k|l$ = 1.193

Fig.16: THE CALCULATED SAR DISTRIBUTION IN mW/kg IN A 16-cm CUBE WITH A DIFFERENT NUMBER OF CELL SUBDIVISIONS

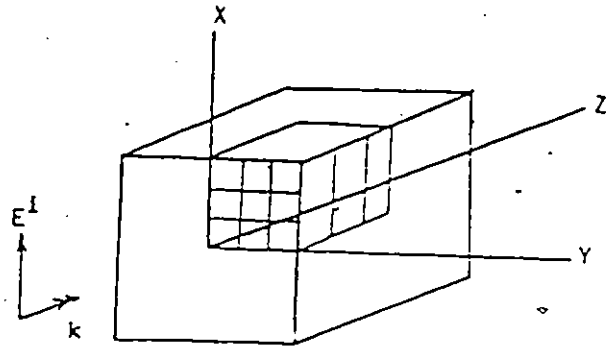

f = 350 MHz
ε' = 38.9
σ = 1.04 S/m
Incident Power Density = 1 mW/cm^2
$|k|$ = 59.6 m^{-1}
l = cell size in m
λ = 10.5 cm

Dimensions: 12cm X 12cm X 12cm
Dimensions/λ : 1.14 X 1.14 X 1.14

46	52	42
104	116	92
123	143	112

1

55	72	48
19	35	32
13	36	34

2

79	95	65
21	19	18
11	9	12

3

$|k|l$ = 1.431

27	30	27
70	74	58
94	103	78

1

39	52	31
36	58	40
40	63	44

2

57	72	41
22	37	25
9	13	13

3

$|k|l$ = 1.193

12	13	16	20
32	29	34	28
52	47	57	46
60	54	67	51

1

14	16	22	13
39	38	50	30
50	44	59	41
59	52	70	46

2

21	24	29	15
37	37	46	25
26	17	23	17
29	17	23	17

3

38	42	46	29
50	50	59	32
32	21	24	16
37	21	22	15

4

$|k|l$ = 0.895

Fig.17: THE CALCULATED SAR DISTRIBUTION IN mW/kg IN A 12-cm CUBE WITH A DIFFERENT NUMBER OF CELL SUBDIVISIONS

16	27	25
38	68	43
52	97	55

1

16	25	21
18	44	23
22	62	28

2

17	12	15
36	14	11
55	20	16

3

|k|1 = 1.193

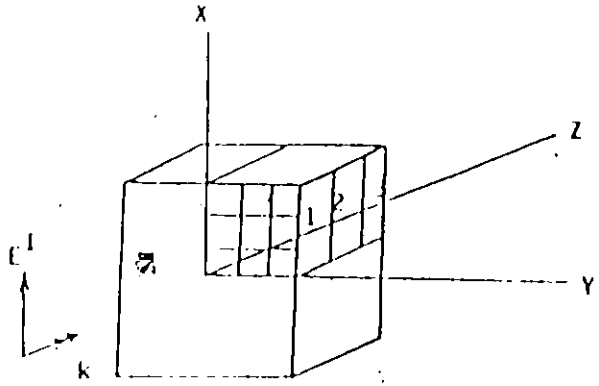

Dimensions: 12cm X 12cm X 6cm

Dimensions/λ : 1.14 X 1.14 X 0.57

f = 350 MHz

ε' = 38.9

σ = 1.04 S/m

Incident Power Density = 1 mW/cm²

|k| = 59.6 m^{-1}

l = cell size in m

λ = 10.5 cm

17	21	28	27
44	50	63	43
66	76	95	58
79	92	116	67

1

23	28	34	28
40	49	59	33
61	81	97	45
74	98	119	52

2

21	23	25	26
10	6	7	9
10	5	7	6
9	1	4	3

3

13	14	14	19
17	10	6	5
29	20	11	8
37	26	14	10

4

|k|1 = 0.895

16	18	22	26	29
40	38	45	52	41
61	58	67	79	53
81	75	86	105	62
91	84	97	120	66

1

21	23	27	32	26
42	39	48	55	34
70	65	80	92	50
92	87	107	128	63
104	99	122	148	71

2

25	29	30	35	30
16	14	14	23	18
20	17	21	29	19
21	15	22	34	17
21	14	22	34	14

3

23	25	25	27	28
11	9	5	7	8
14	11	6	4	6
15	11	6	2	3
16	10	4	0	1

4

11	13	16	17	25
5	8	4	3	5
8	8	6	3	3
11	12	10	5	3
13	15	13	6	3

5

|k|1 = 0.716

Fig.18: THE CALCULATED SAR DISTRIBUTION IN mW/kg IN A BLOCK WITH A DIFFERENT NUMBER OF CELL SUBDIVISIONS

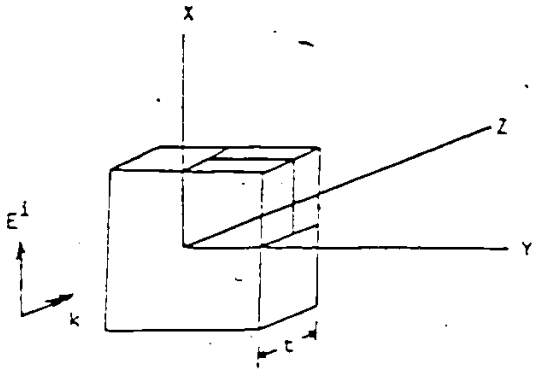

f = 350 MHz

ε' = 38.9

σ = 1.04 S/m

Incident Power Density = 1 mW/cm^2

|k| = 59.6 m^{-1}

l = cell size in m

λ = 10.5 cm

Dimensions: 12cm X 12cm X tcm

Dimensions/λ : 1.14 X 1.14 X t'

14	29	27
32	67	50
39	84	60

1

5	6	10
10	6	11
14	6	13

2

|kl| = 1.431

t = 4.8cm, t'= 0.46

18	32	28
44	78	49
60	112	64

1

2	6	9
1	6	6
1	6	5

2

|kl| = 1.193

t = 4.0cm, t'= 0.38

14	19	26	25
30	40	50	32
43	59	75	42
50	70	91	46

1

7	11	17	18
9	17	23	13
10	22	32	13
10	25	37	12

2

|kl| = 0.895

t = 3.0cm, t' = 0.28

Fig.19: THE CALCULATED SAR DISTRIBUTION IN mW/kg IN A BLOCK WITH DIFFERENT THICKNESSES AND DIFFERENT NUMBERS OF CELL SUBDIVISIONS

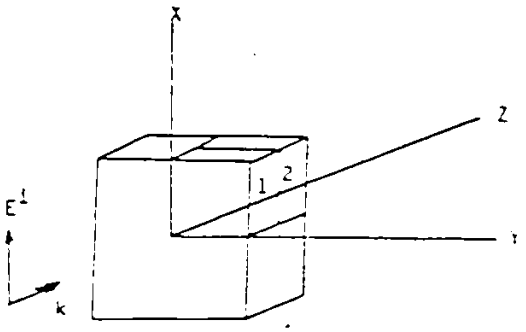

Dimensions: 12cm X 12cm X 4cm

Dimensions/λ : 1.14 X 1.14 X 0.38

f = 350 MHz

ε' = 38.9

σ = 1.04 S/m

Incident Power Density = 1 mW/cm^2

|k| = 59.6 m^{-1}

l = cell size in m

λ = 10.5 cm

|k|l = 1.193

46	76	59
115	204	125
156	290	167

$|E_x|^2$

0.5	7	14
0.05	0.9	0.2
0.01	0.2	0.4

$|E_y|^2$

0.01	0.2	0.1
0.3	0.2	0.09
0.05	0.03	0.03

$|E_z|^2$

(1)

1	9	24
0.3	0.5	0.2
0.04	0.08	0.3

$$\frac{|E_y|^2 + |E_z|^2}{|E_x|^2} \times 100\%$$

(1)

Fig.20: THE CALCULATED E-FIELD DISTRIBUTION IN V^2/m^2 IN THE FIRST LAYER OF A BLOCK AND THE RATIO BETWEEN THE SUM OF THE COMPONENTS $|E_y|^2$ AND $|E_z|^2$ AND $|E_x|^2$ IN PERCENTAGE

Chapter 4

EXPERIMENTAL PROCEDURES AND MATERIALS

4.1 GENERAL

A brief overview of different experimental methods for obtaining the dosimetric data was presented in the first chapter. The technique used in this thesis employs an electric field probe to measure the E-field distribution. This method has the following advantages:

- The actual field intensity can be acquired through real time measurements;
- Due to the high sensitivity of the probe, the phantom is exposed to low power irradiation so that heating effects are eliminated. This is important as an increase in the phantom temperature can alter the electric properties of the simulated tissue, whose permittivity is temperature dependent. A change in the electrical properties of the phantom can result in a change of the field distribution. The rate of temperature increase can be calculated using the following formula:

$$\frac{dT}{dt} = \frac{P}{\rho \cdot S} = \frac{SAR}{S} \qquad (20)$$

where,

S = 3975 J/kg-°C, is the specific heat of the phantom material

T is the temperature in °C

t is the time in s

P is the absorbed power density in the medium in W/m^3

For example, the rate of temperature increase for a 16-cm diameter sphere having the average tissue permittivity at 350 MHz with a 3-mW/cm^2 incident power density, which corresponds to the local SAR at the centre of 0.046 W/kg, is equal to 0.04 °C/hr., therefore temperature change due to a 3-mW/cm^2 incident power density is insignificant and does not affect the measurement of the SAR distribution;

— A large amount of data can be acquired in a relatively short time period by using a computer based scanning system;

— Fields at the point of measurement are only minimally perturbed by the insertion of the probe, if the probe is small compared with the wavelength in tissue (λ) and the measured object.

4.2 COMPUTER-BASED SCANNING SYSTEM

The measurements of the electric field distributions inside different models can be done relatively fast by use of a computer-based scanning system, which was designed and built at the University of Ottawa. The block diagram of the system and a part of the system inside the anechoic chamber are shown in Figs.21 and 22, respectively. The automatic scanning system (Barski et al [4]) which can acquire, store, display, and record the field intensity and its orientations consists of:

— An anechoic chamber with reflection of about -20db for frequencies greater than 300 MHz;

— Electromagnetic radiators for selected frequencies,

a) 350 MHz

-- a half wavelength slot antenna with gain of 4.87 or a half wavelength dipole with gain of 3.82 both fed from a HP8656A signal generator and a A1ADK power amplifier

b) 920 MHz

-- a half wavelength slot antenna with gain of 6.1

c) 2450 MHz

-- a horn antenna with gain of 26.7 fed from an HP8690b generator and a SINGER5120 power amplifier;

- A phantom model under test;

- A miniature triaxial E-field probe;

- An optically linked telemetry system:

  a telemetry transmitter mounted on the scanning unit and is used to amplify and convert the detected 560 Hz (which has been chosen from the optimal S/N of the system and sensitivities of the electric field probes [38]) or DC signal into a frequency modulated pulse signal. The conversion is done by a Voltage to Frequency converter, which drives an infrared LED and transmits the information on an optical fiber into the telemetry receiver outside the chamber. This eliminates scattering by metallic cables, minimizes RF (Radio-frequency) interference in the system electronics, and reduces the cross-talk between the channels;

- A mechanical structure for supporting and positioning the probe with an uncertainty of ± 0.05mm along all three axes [4].

— A computer system consisting of an Intel 8085 used to control the experiment and a PDP11/34 for data acquistion, storage, display, and recording.

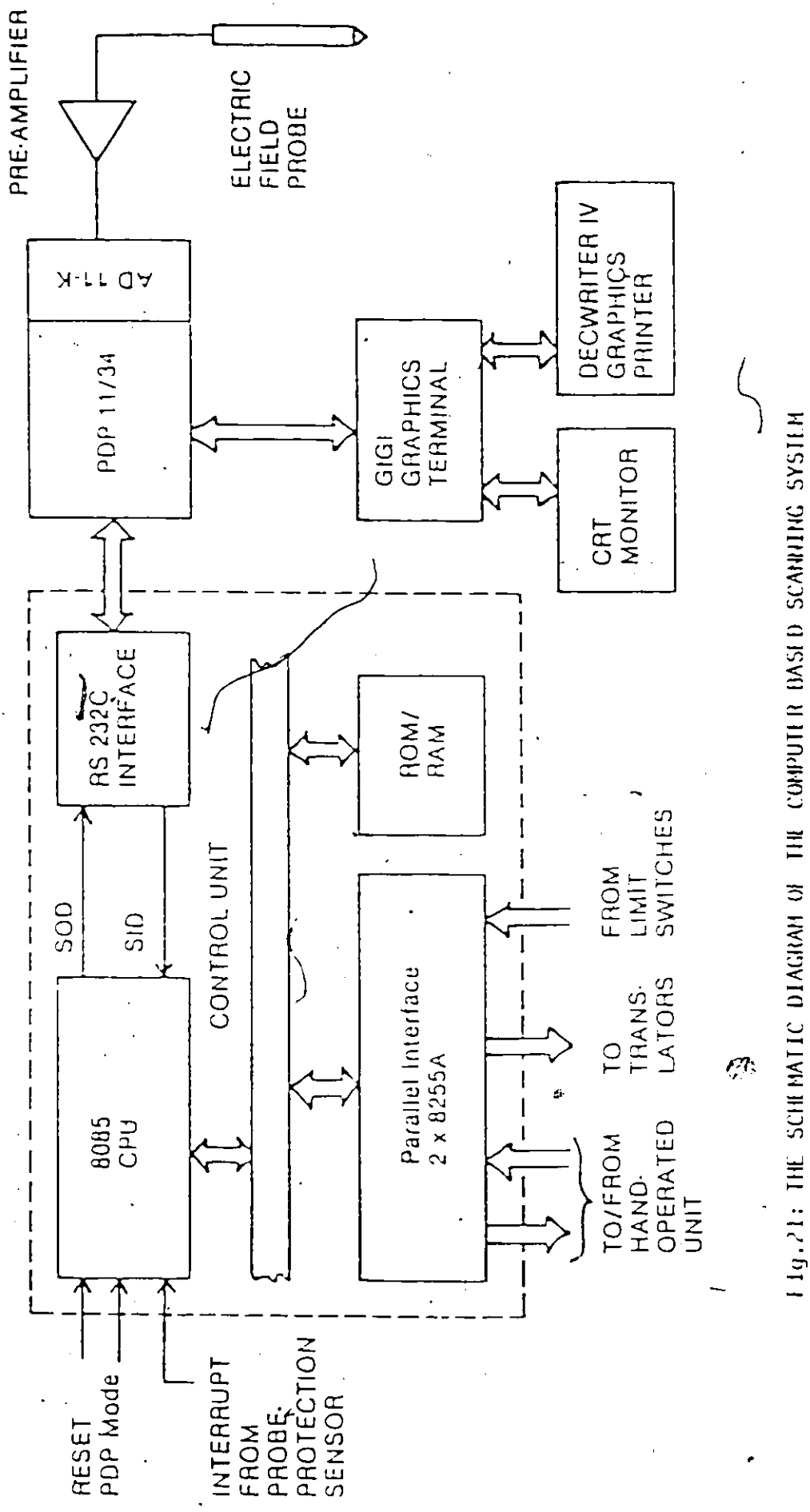

Fig.21: THE SCHEMATIC DIAGRAM OF THE COMPUTER BASED SCANNING SYSTEM

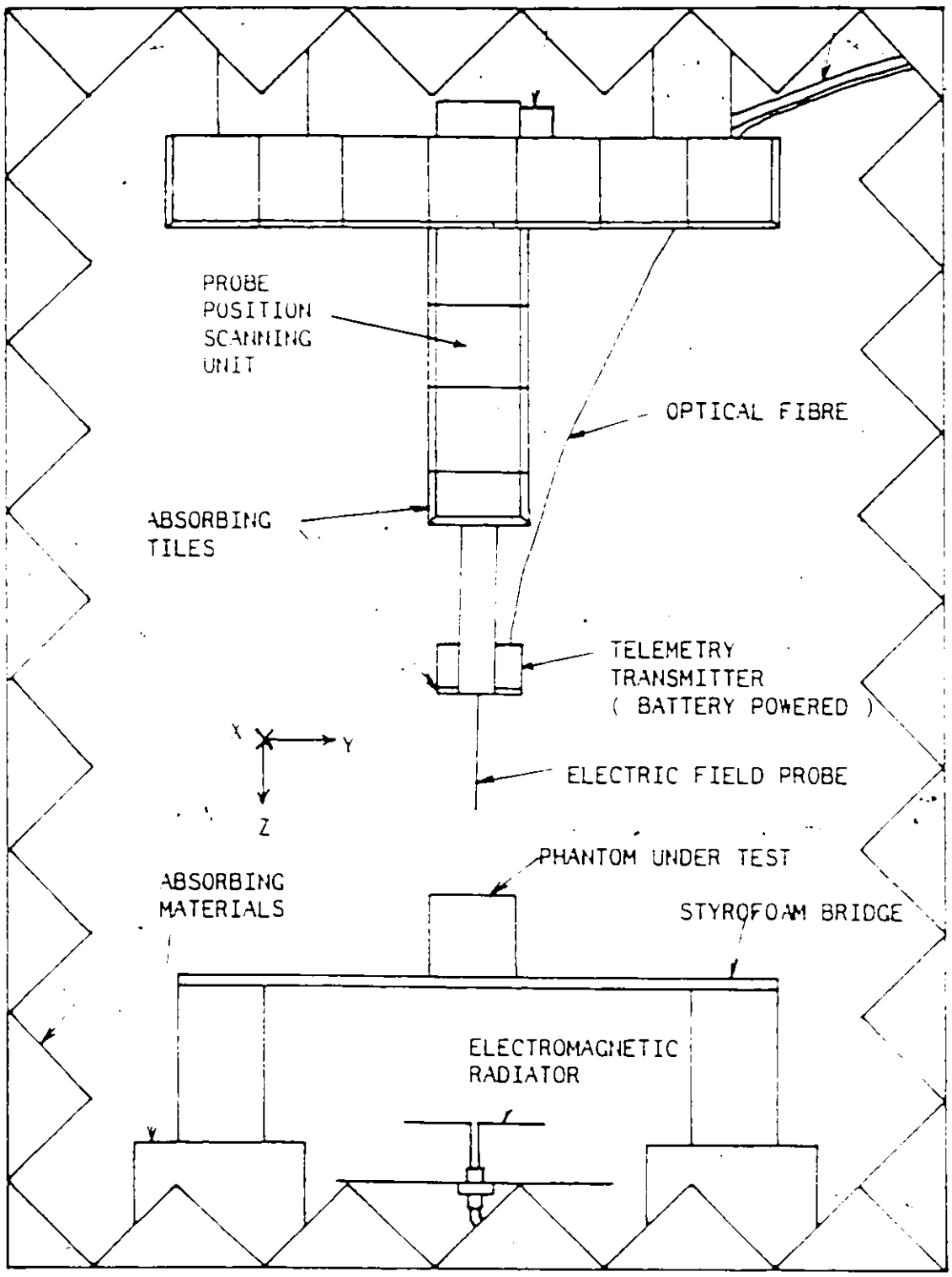

Fig.22: AN AUTOMATED SCANNING SYSTEM INSIDE THE ANECHOIC CHAMBER

4.3 ELECTRIC FIELD PROBE

Three triaxial E-field probes: a Narda Model 2608 (3mm in diameter), a EIT Model 979 (1.1cm in diameter), and a Holaday Model IME-01 (2cm in diameter), which are all insulated by a dielectric tubing, are used to measure the electric field intensity inside the phantom. The basic elements of the probe are:

- Three orthogonal miniature dipoles each on its own substrate arranged in three mutually perpendicular planes. For the EIT probe, the dipoles are arranged in an "I" configuration so that the three planar substrates can be placed very closely together and still provide minimal interaction between the orthogonal dipoles. The dipoles in the Narda and Holaday probes are arranged at an angle of 54° with respect to the long probe axis so that the single dipole can be oriented in three mutually perpendicular directions by successive rotations of the probe about its axis by 120°. Their simplified structures and dimensions are shown in Fig.23;

- The center gap of each dipole is shunted by a zero-bias (low barrier) beam lead Schottky diode. It has been verified [22] that the output DC voltage is proportional to the square of E-field

intensity within a certain range of E-field intensities, therefore the square of the total E-field intensity, $|E_T|^2$ is given by the following expression:

$$|E_T|^2 = B*V_T \qquad (21)$$

where,

V_T is the sum of all three voltages

B is the calibration factor for the probe at a given frequency and for a given phantom material;

— High-resistance thin-film leads with a low-pass, distributed filter composed of a highly lossy series inductance with distributed interload capacitance (Bassen et al. [5]);

In general, all three probes have higher response (i.e. approximately two to four times higher in the detected voltage for the same E-field intensity [22]) in the tissue equivalent material than in air and the response at a fixed frequency changes very slightly in tissue equivalent materials of different dielectric properties. Due to the low-pass filtering effect of the probe, the sensitivity of the probe decreases when the modulation frequency increases (Stuchly et al. [38]). This is shown in Fig.24.

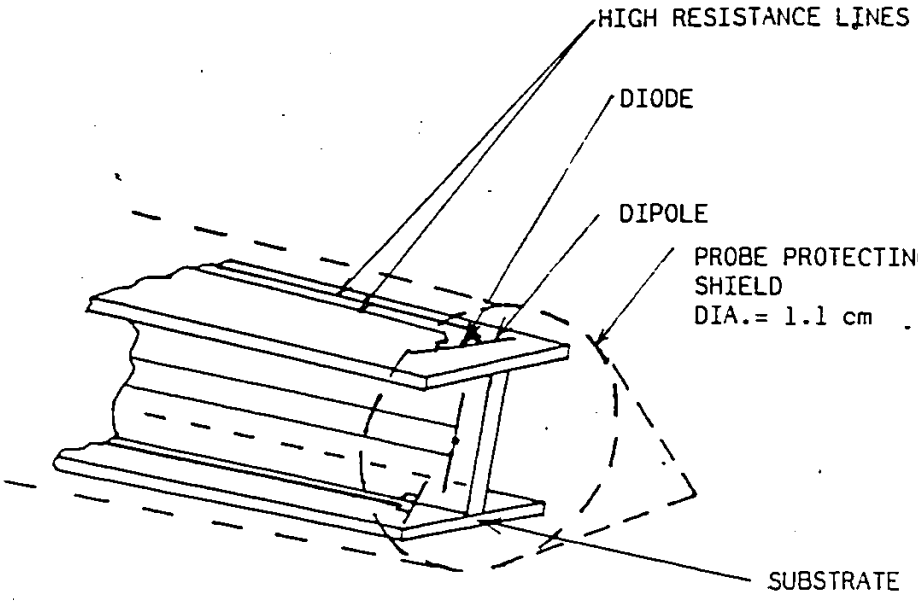

i.) I-BEAM CONFIGURATION FOR THE EIT979 PROBE

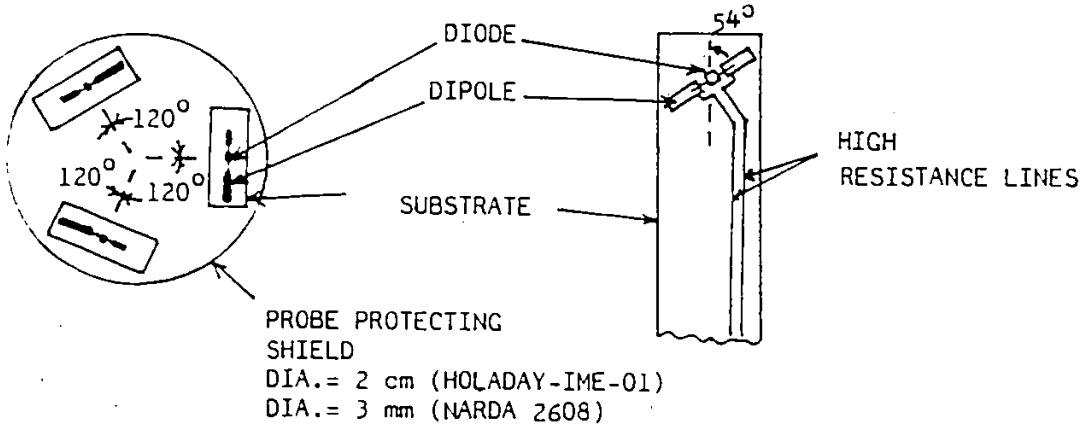

ii.) BOTTOM VIEW OF THE NARDA OR HOLADAY PROBES

iii.) STRUCTURE OF THE DIPOLE IN THE SUBSTRATE OF THE NARDA OR HOLADAY PROBES

Fig.23: SIMPLIFIED STRUCTURE OF THE EIT979 , NARDA 2608, AND HOLADAY-IME-01 PROBES

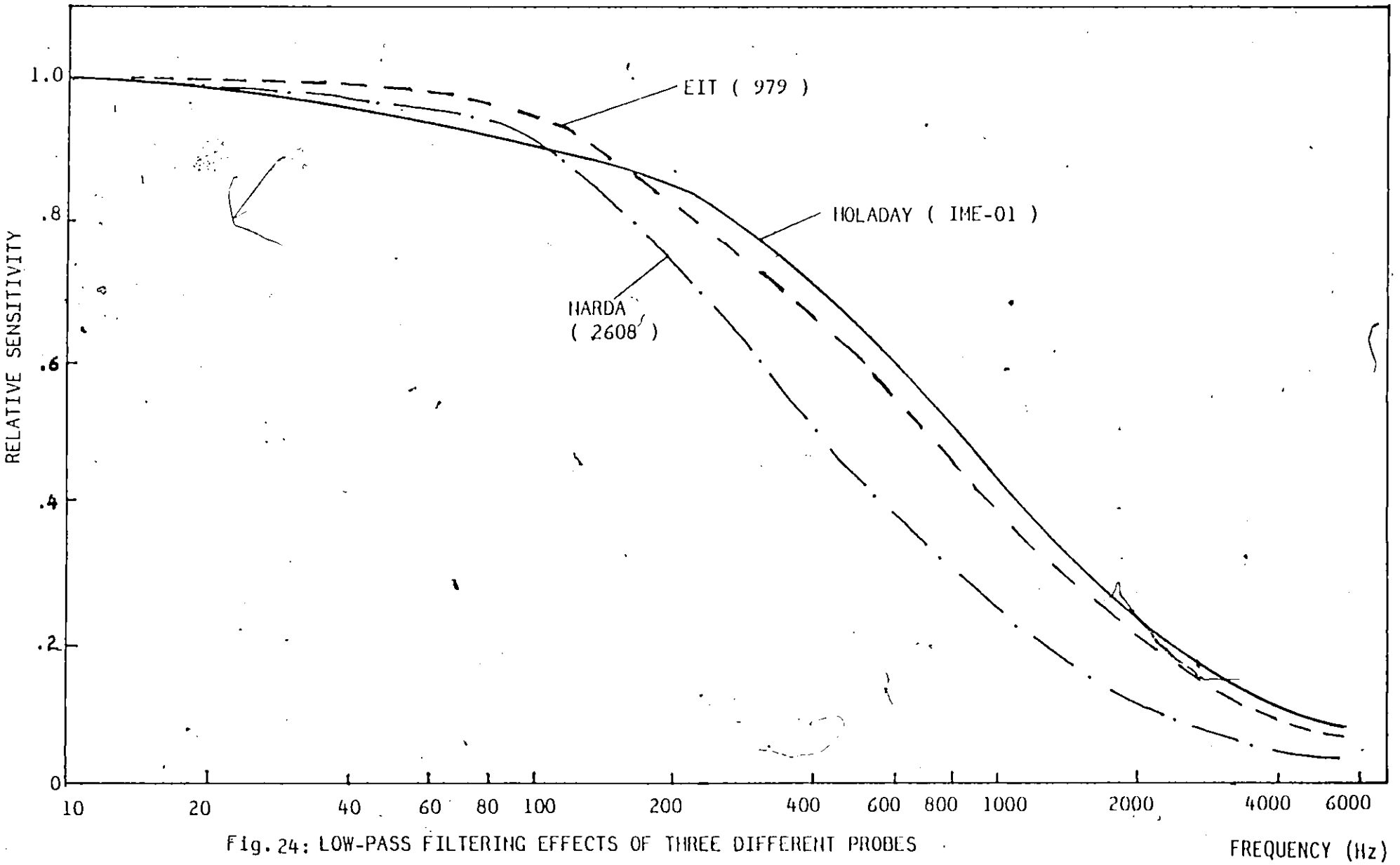

Fig. 24: LOW-PASS FILTERING EFFECTS OF THREE DIFFERENT PROBES

4.4 PHANTOM MATERIALS

To simulate electrical properties of biological tissues, special phantom materials were developed. The phantom materials with average tissue properties at a frequency of 350 MHz are prepared using a recipe given in Appendix D. The relative permittivities of the phantom were measured using an automatic measurement system. The system consists of an open-ended coaxial line sensor and an automatic network analyser under computer control. This system, when calibrated with well-known dielectric materials such as water or saline solution, can measure the permittivity with an uncertainty less than 3% (Kraszewski et al. [26]).

Different batches of the 350-MHz average-tissue phantom made following the same recipe are consistent and their differences in permittivity are within 3%. The average dielectric constant and conductivity of the 350-MHz average-tissue phantom as measured at a room temperature of 23°C are equal to 38.86 ± 1.17 and 1.04 ± 0.02 (S/m), respectively. Average-tissue phantom is used at 350 MHz because it has lower viscosity than the muscle-tissue phantom.

Knowledge of accurate values of the permittivity is important for the comparison of the measured E-field intensities with the calculated ones.

At frequencies of 920 and 2450 MHz, saline solutions are used as phantom materials because of their low viscosity and simplicity of preparation. The advantage of using low viscosity material is that it can avoid sustained air bubbles caused by the movement of the probe. These air bubbles, especially when their sizes are comparable to λ, may perturb the field in the phantom and therefore affect the accuracy of the measurement. The saline solution at 920 MHz contains 1 percent of salt by weight, while distilled water is used at 2450 MHz. The electrical properties of these saline phantoms as measured at a room temperature of 23°C are $\varepsilon' = 76.5$ and $\sigma = 1.58$ (S/m) at 920 MHz, and $\varepsilon' = 77.9$ and $\sigma = 1.021$ (S/m) at 2450 MHz. The conductivities of these saline solutions are very close to those of the muscle tissue.

4.5 SPHERICAL, BLOCK, AND CYLINDRICAL MODEL MOLDS

Molds for the spherical and block models are made of 2.5-cm and 5-cm radio-frequency transparent polystyrene foam. The mold for the cylindrical model is made of 0.32-cm thick acrylic having a dielectric constant of 2.6. All model dimensions are exactly the same as the ones used in the numerical analysis with the details shown in Fig.25.

4.6 EXPOSURE CONDITIONS OF THE MODELS

Due to the small (as compared to λ_o) sizes of the spherical and block models, they are exposed to the approximate plane wave in the far field region (i.e. distance from the source > $2D^2/\lambda_o$, as derived from the parallel ray approximation which creates a phase error smaller than 45° [39]; where D is the length of the source) of the radiator. The incident power density for the far field exposure is inversely proportional to the square of the separation between the phantom and the source.

Since the length of the cylinder is comparable to λ_o, the cylinder is exposed to a large portion of the spherical wave. In this case, only the middle section of the cylinder satisfies the far field exposure conditions. The incident power density at different sections in the cylinder can be evaluated by multiplying the incident power density at the center section by a factor. This factor is the square of the product of the field pattern and the electric field intensity calculated at the point of incidence of the wave in that particular section, due to the dipole-antenna source [39].

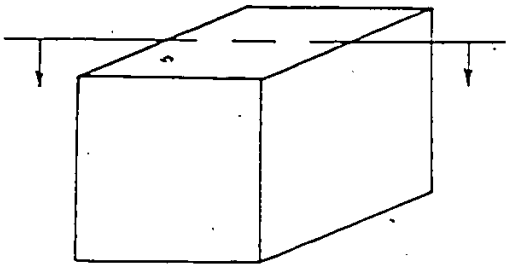

i.) EXTERIOR OF THE SPHERE AND BLOCK MODELS

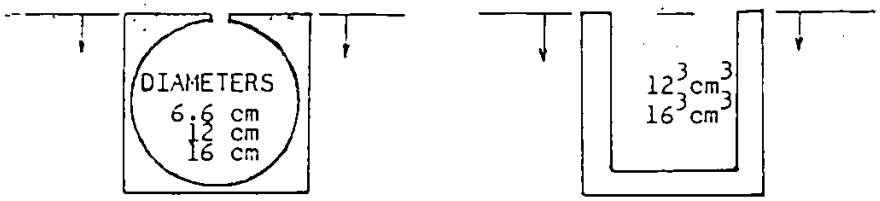

ii.) SECTIONAL VIEWS OF THE SPHERE AND BLOCK MODELS

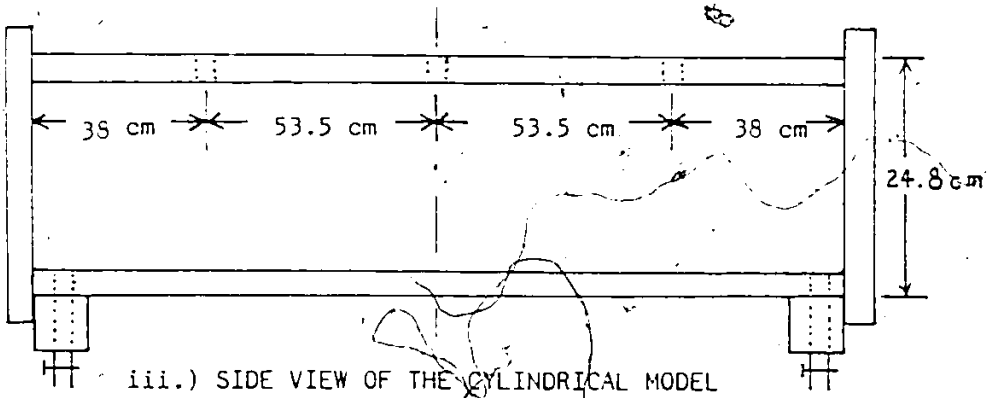

iii.) SIDE VIEW OF THE CYLINDRICAL MODEL

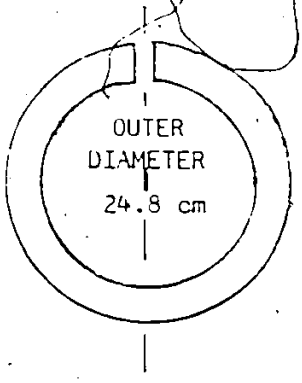

iv.) SECTIONAL VIEW OF THE CYLINDRICAL MODEL

Fig.25: SHAPES OF THREE DIFFERENT MODELS

4.7 UNCERTAINTY ANALYSES

The sources of experimental errors are summarized in Table 3. They are also described as follows:

— Non-isotopic response of the electric field probe

i) The rotational symmetry of the probes and the orthogonality of the dipoles in the probes, such as the EIT probe, whose rotational symmetry is within ±12% and one of its dipoles is coupled to another one by 12% of power as shown in Fig.26;

ii) Direct pick-up from the lossy transmission lines in the probe was measured when the incident E-field was directed along the long axis of the probe. The signal measured from this direct pick-up is more than ten times that detected by the dipoles;

— Reflections from the column of the scanning unit

i) The minimal reflection region is located at a distance of more than $0.37\lambda_o$ away from the column when the antenna is located on the ground. This is obtained from results of the field measurement in air as shown in Fig.27;

ii) Minimal reflections also occur when the antenna is radiating from the side and behind the absorbing tiles on the column;

— Reference direction of the incident field vector with respect to the axis of the test body

i) A nonuniform incident field can result from the radiator and test model not being leveled. As shown in Fig.28, the uniformity of the incident field can be improved 1% by leveling the radiating element and the test model;

ii) Misalignment of the incident field vector with the reference axis of the test model can cause cross polarization effects in the measured results. A rotation of 5^{o} from the reference axis will result in a 9% change in the cross polarization of the incident field;

— Nonlinear characteristics of the amplifiers and probe detectors:

This can be prevented by operating the measuring system within the linear range as shown in Fig.29;

— Decrease in detected output voltage:

This is caused by the drifting of the output power level from the unstable power amplifier or by

the battery discharge in the transmitter amplifier after a long switch-on period. This can be corrected by momentary adjustment to maintain the output power at a constant level throughout the experiment and checking the battery voltage before the measurement;

— Uncertainty in distance measurements

i) The map of the required measured points is created manually;

ii) Distance between the source and the test model is measured by a meter-stick with an accuracy of ±2 mm;

iii) The molds of the phantom models were constructed with a dimensional accuracy of ±1 mm;

— Nonhomogeneous phantom materials

After the phantom has been stored for a period of time, some ingredients may settle in the phantom and some water may have evaporated. All these factors will change the permittivity of the phantom. This can be avoided by well mixing and testing the phantom permittivity before the field measurement. From the calculation on the variations of the permittivity in spherical models, a 3% change in

permittivity will result in a difference of 2.2% in the peak SAR.

TABLE 3

A SUMMARY OF THE SOURCES OF EXPERIMENTAL UNCERTAINTIES

TYPE OF UNCERTAINTIES	SOURCES	CORRECTION	EXPERIMENTAL ERROR AFTER CORRECTION
Nonisotopic Electric Field Probe	-- nonperpendicular dipoles -- direct pick-up from the transmission lines on the probe	cannot be corrected	± 12%
Reflections from the column of the scanning unit	-- reflections coming from the metallic portion of the scanning unit which is not covered by the absorbing tiles	measurements to be done at a distance larger than $0.37\lambda_0$ away from the bottom part of the scanning unit or irradiation from the opposite side of the metallic structure which is covered by the absorbing tiles or covering all parts of scanning system with absorber	± 1%
Nonlinear Characteristics of the Equipment	-- nonlinear properties of the diode detector in the probe and the amplifiers	to operate the system in its linear range	± 2%
Decrease in Output Voltage	-- drifting of the unstable power amplifier -- battery discharge in the transmitter	preliminary testing of the battery voltage and momentary adjustment of the output power	± 2%
Distance Measurements	-- distance between the source and reference points -- initial manual mapping -- dimensions of the tested model	measurements to be done very carefully	± 5%
Nonhomogeneous Phantom Materials	-- mixture settling and water evaporating	mix and test the properties of the phantom before the field measurement	± 2.2%
		Total Experimental Error	± 13.5%

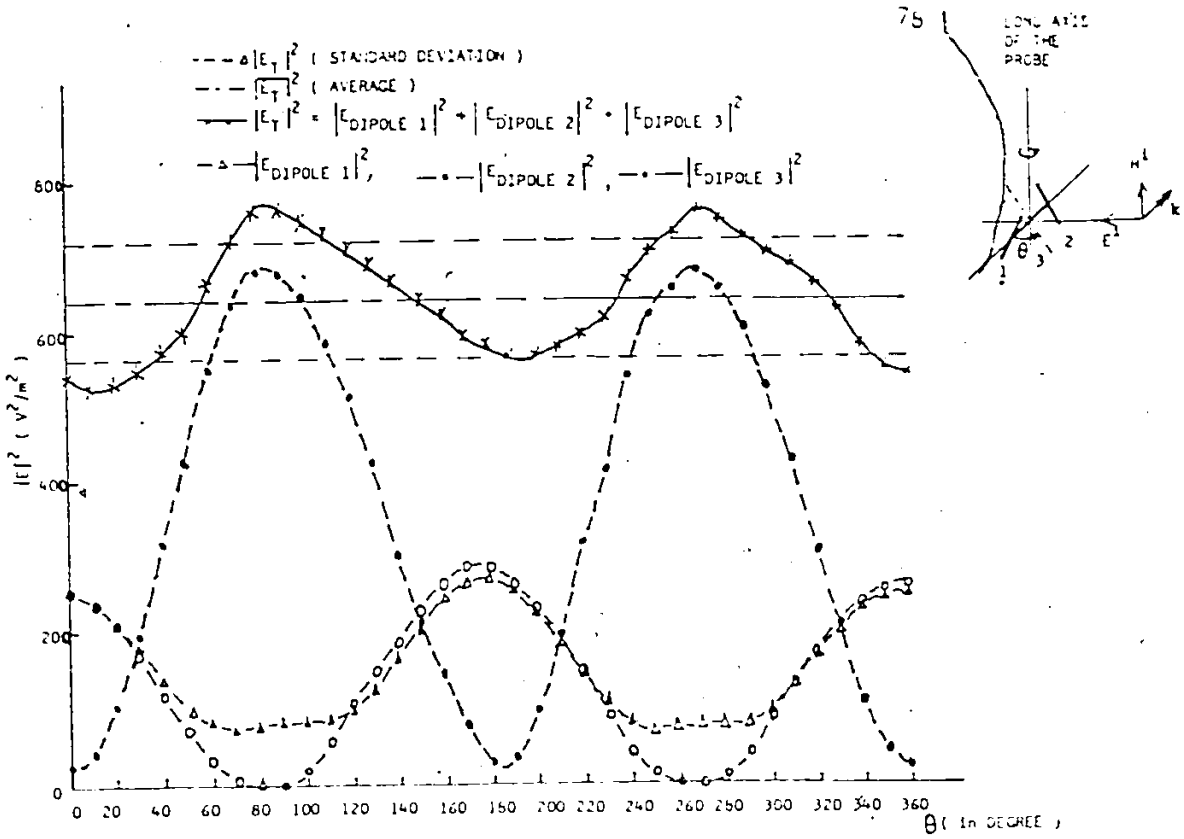

Fig.26: THE ROTATIONAL SYMMETRY OF THE E11979 PROBE MEASURED INSIDE THE TEM CELL

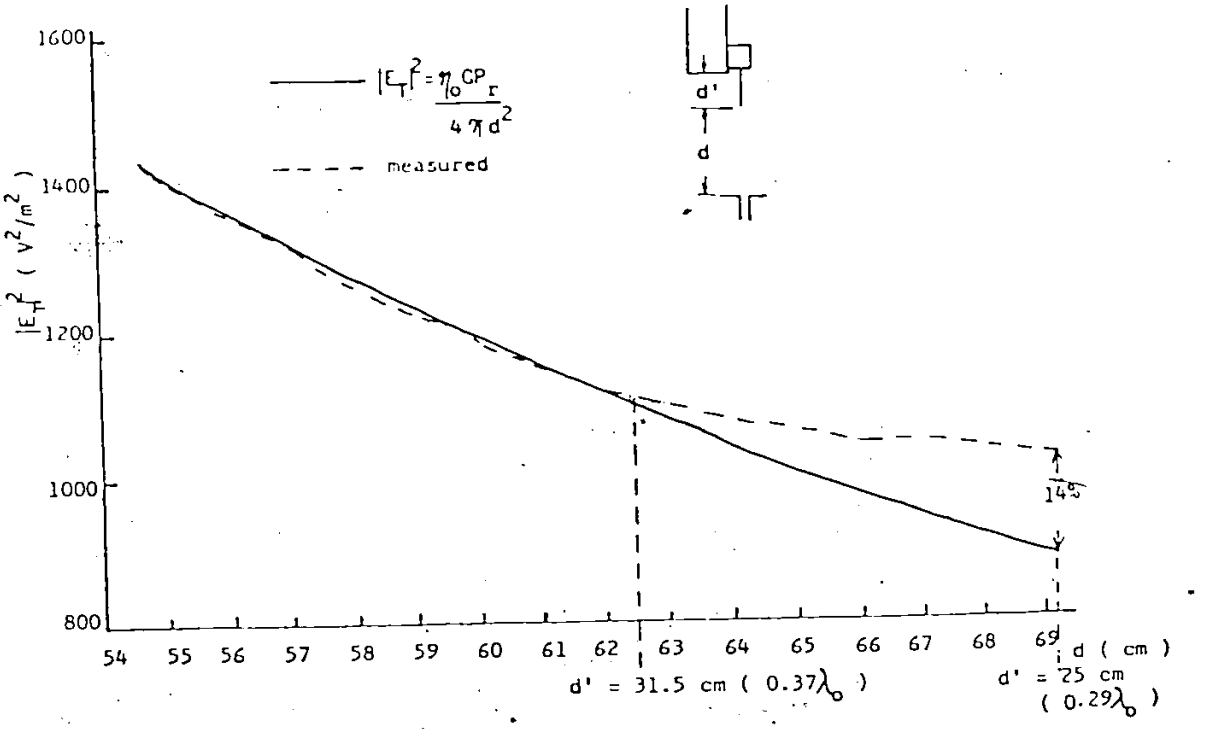

Fig.27: THE ELECTRIC FIELD MEASUREMENT IN AIR (P_r = 3W, G = 4.87, f = 350 MHz, SENSITIVITY OF THE E11979 PROBE IN AIR: C = 0.31 $\mu V/(V^2/m^2)$)
d + d' = 94 cm

.94	.94	.95	.95	.96	.94
.96	.97	.98	.98	.98	.98
.98	.99	1	1	1.01	1.01
1	1.01	1.02	1.02	1.02	1.02
1.02	1.02	1.02	1.03	1.03	1.03
1.02	1.03	1.04	1.04	1.05	1.05

UNLEVELED RADIATING SOURCE
(STANDARD DEVIATION = 3%)

1.02	1.02	1.02	1.02	1.02	1.02
1.02	1.02	1.02	1.04	1.02	1.02
1.02	1	1.02	1	1.01	1.01
1	1	1	1	1	.99
1	1.02	1	1.02	1	.98
.98	1	.98	1	1	.98

LEVELED RADIATION SOURCE
(STANDARD DEVIATION = 2%)

Fig.28: NORMALIZED MEASURED VOLTAGE WITH RESPECT TO ITS AVERAGE OVER AN AREA OF $.14 \times .14 \lambda_o^2$ AT A DISTANCE OF $.84 \lambda_o$ FROM THE RADIATING ELEMENT ($1/2 \lambda_o$ SLOT)

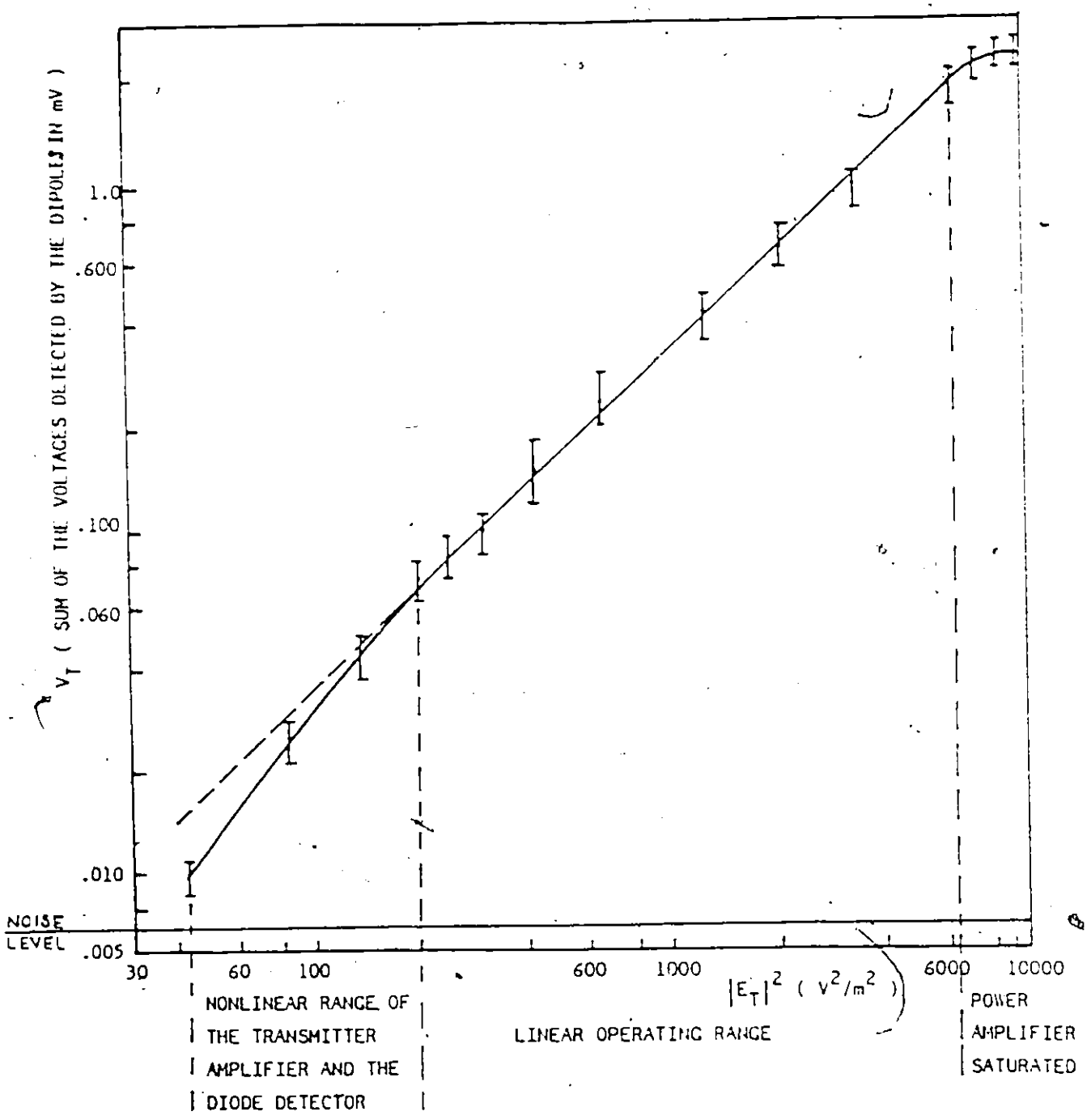

Fig.29: THE DYNAMIC RANGE OF THE EIT979 PROBE, TRANSMITTER AMPLIFIER, AND A1ADK POWER AMPLIFIER (GAIN OF THE TRANSMITTER AMPLIFIER = 4000 ± 80)

Chapter 5

COMPARISONS OF EXPERIMENTAL AND THEORETICAL RESULTS

5.1 GENERAL

All experimental results presented here are normalized to 1 mW/cm^2 incident power density in order to compare them with the theoretical results. All three models are exposed to the far field of the radiator. The error bars shown on the experimental curves represent absolute uncertainties and do not include the effect of imperfect shape of the model. The absolute uncertainties are estimated by taking the root mean square of the following factors:

- Uncertainty of the power meter and directional coupler (12% as specified by the manufacturer);
- Uncertainty of the voltmeter (1.2% as specified by the manufacturer);
- Uncertainty of the sensitivity of the probe (as shown in Table 4);
- Reproductability of the measured results (random variations) (5% as estimated);

— Uncertainty of the gain of the measurement system (4% as measured);

The response of the probes is calibrated using the measured results in spheres and cylinder. The sensitivity of the probe is evalulated by dividing the sum of the detected voltages from the three dipoles by the calculated field intensity at selected points and averaging over a few matched points. The sensitivities of the probes at three different frequencies and in different materials are given in Table 4. For comparison, those values obtained from a large (as compared to λ) flat layer of muscle phantom are also given in Table 4. Excellent agreement between sensitivities in differently-shaped phantoms gives confidence in both theoretical and experimental methods.

TABLE 4

RESPONSE OF ELECTRIC FIELD PROBES

PROBE	FREQUENCY (MODULATION FREQUENCY)	SOURCE OF CALIBRATION	SENSITIVITY* ± ** (μV PER V^2/m^2)
HOLADAY (IME-01)	350 MHz(1) (560 Hz)	Air	4.05
		Average Tissue Phantom: 16-cm diameter sphere	25 ± 2
		Cylinder (diameter = 24.8 cm)	
		TM Mode	20 ± 1
		TE Mode	17 ± 1
		Average	23 ± 2
		Flat Muscle Layer	23 ± 1
EIT (979)	350 MHz (560 Hz)	Air	0.31
		Average Tissue Phantom: 16-cm diameter sphere	2.9 ± 0.3
		12-cm diameter sphere	2.9 ± 0.1
		Cylinder (diameter = 24.8 cm)	
		TM Mode	3.0 ± 0.1
		TE Mode	2.8 ± 0.1
		Average	2.9 ± 0.2
	920 MHz (DC)	Muscle Saline: Average response in 12- and 16-cm diameter spheres	2.4 ± 0.2
		Flat Muscle Layer	2.23 ± 0.06
	2450 MHz(2) (560 Hz)	Flat Muscle Layer	0.95 ± 0.05

TABLE 4

(CONTINUED)

PROBE	FREQUENCY (MODULATION FREQUENCY)	SOURCE OF CALIBRATION	SENSITIVITY* ± ** (μV PER V^2/m^2)
NARDA (2608)	920 MHz (DC)	Muscle Saline:	
		16-cm diameter sphere	0.62 ± 0.05
		12-cm diameter sphere	0.67 ± 0.08
		6.6-cm diameter sphere	0.67 ± 0.04
		Average	0.65 ± 0.06
		Flat Muscle Layer	0.60 ± 0.03
	2450 MHz (560 Hz)	Air	0.02
		Muscle Saline:	
		12-cm diameter sphere	0.07 ± 0.01
		6.6-cm diameter sphere	0.08 ± 0.02
		Average	0.073 ± 0.02
		Flat Muscle Layer	0.106 ± 0.007

(1) One can conclude from the results shown in Fig.30 that this probe should not be used for models with a diameter smaller than 16 cm at 350 MHz or with a diameter of 16 cm at frequencies higher than 350 MHz;

(2) One can conclude from the results shown in Fig.35 that this probe should not be used for models with a diameter smaller than 12 cm at 2450 MHz or with a diameter of 12 cm at frequencies higher than 2450 MHz.

* The calculations of the sensitivity are described on P.82.

** The uncertainty of the sensitivity is derived from the standard deviation of the calculations as described on P.82.

5.2 SPHERICAL MODELS

In general, the experimental results obtained for the spherical models of different sizes and at different frequencies agree well with the theoretical results, both qualitatively and quantitatively. The details are shown in Figs.30-36.

Figure 30 shows the effect of the imperfect shape of the model at the entrance point of the probe (formation of the neck), the smearing and perturbation effects of the Holaday probe near the bottom part of the sphere at 350 MHz.

The shape of the sphere was distorted by inserting the probe thus raising the level of the phantom material in the sphere. This happened in all other measurements in spherical models with a similar structure. The smearing effect of the probe is due to the physical separation of the dipoles in the probe, while the perturbation is mainly because of the size of the probe.

The measurement results obtained along different axis of a sphere is shown in Fig.31. Unfortunately, correct measurement results along the axis parallel to the incident electric field cannot be obtained due to the direct pick-up by the lossy transmission lines in the probe.

Figures 32-34 show the results for the spheres with different diameter to wavelength ratios. These figures

indicate the excellent spatial resolution and consistent response of the Narda probe at 920 MHz.

A good example to show the smearing and cross coupling effects of the EIT probe is given in Fig.35. The discrepancies between the calculated and measured results using the Narda probe as shown in Figs.35-36 are mainly due to the perturbation of the probe at that frequency, the uncertainties in the permittivity of the phantom, and the uncertainty in the off-axis field measurement.

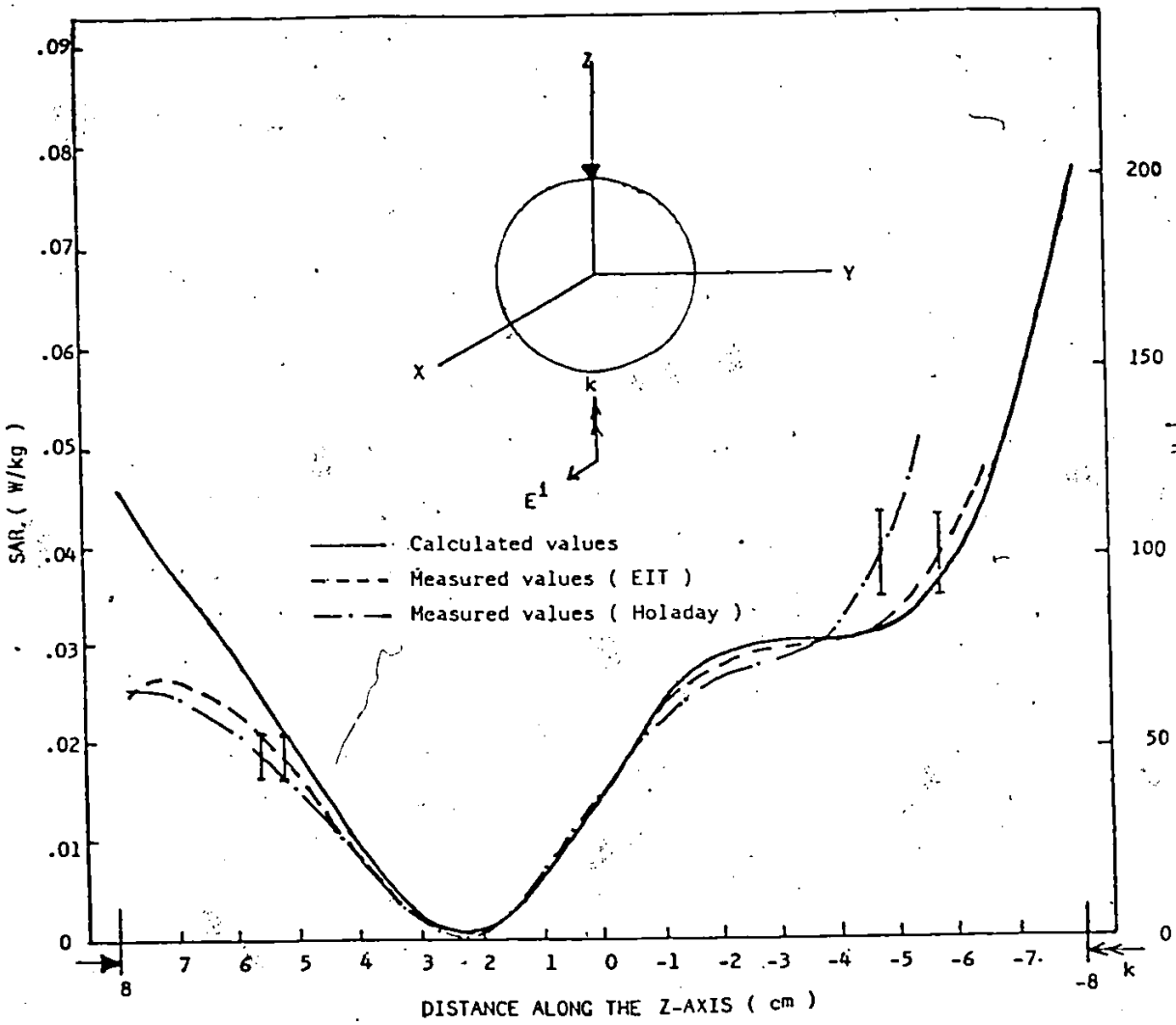

Fig. 30: COMPARISON OF THE CALCULATED AND MEASURED SAR AND ELECTRIC FIELD OF THE AVERAGE TISSUE PHANTOM SPHERE ($\varepsilon' = 38.9$, $\sigma = 1.04$ S/m, $f = 350$ MHz, Incident Power Density = 1 mW/cm^2, Diameter = 16 cm, Diameter/$\lambda_o = 0.19$, and Sensitivity = $2.9 \pm .3$ $\mu V/(V^2/m^2)$ (EIT), 25 ± 2 $\mu V/(V^2/m^2)$ (Holaday); where the double arrow indicates the direction of incidence of the EM wave and the dark arrow shows where the measurement started. Absolute uncertainties of the measured values are $\pm 12\%$ (EIT) and $\pm 11\%$ (Holaday).

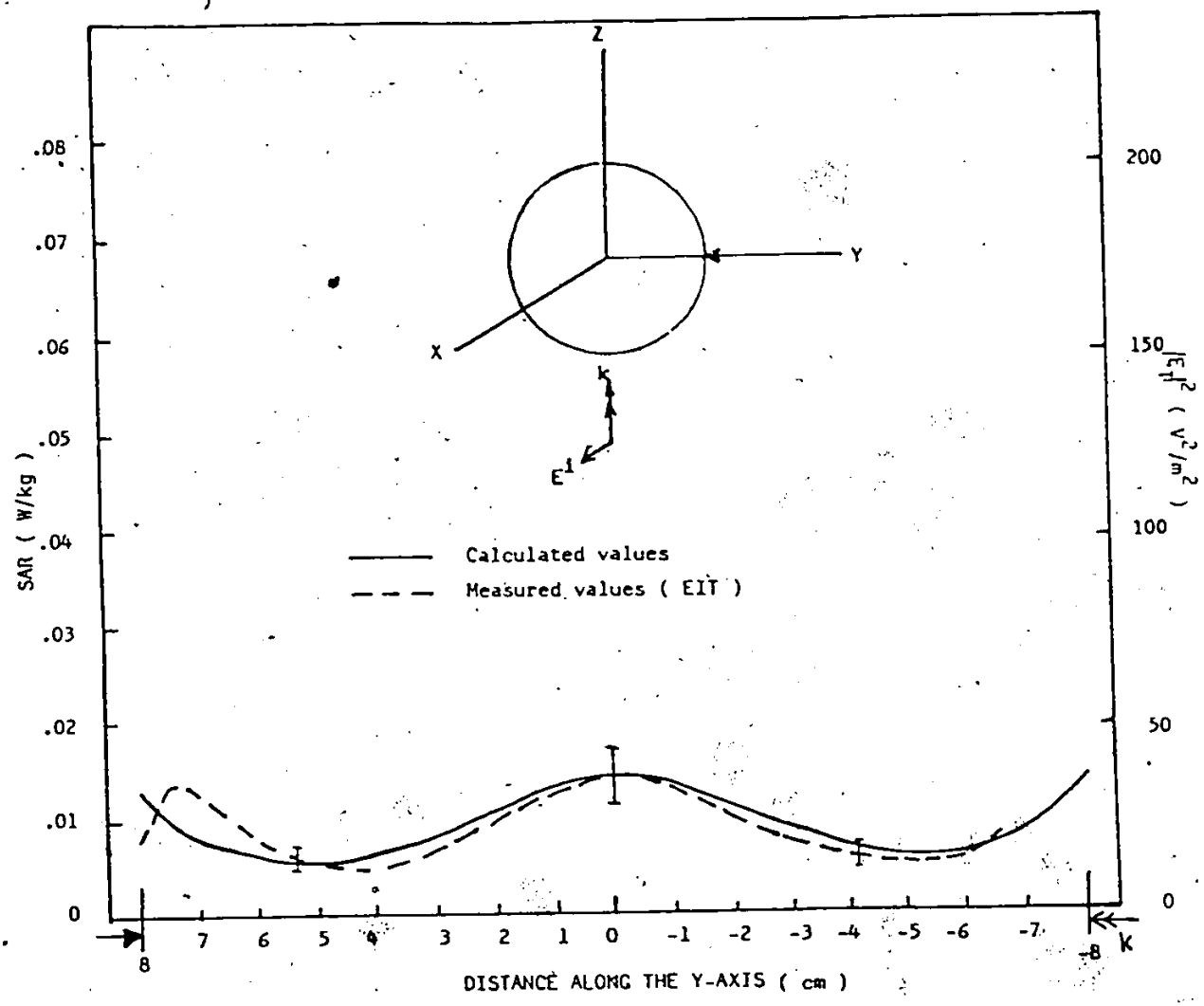

Fig.31: COMPARISON OF THE CALCULATED AND MEASURED SAR AND ELECTRIC FIELD OF THE AVERAGE TISSUE PHANTOM SPHERE ($\varepsilon' = 38.9$, $\sigma = 1.04$ S/m, f = 350 MHz, Incident Power Density = 1 mW/cm^2, Diameter = 16 cm, Diameter/λ_o = 0.19, and Sensitivity = 2.9 ± .5 μV/ (V^2/m^2) (EIT); where the double arrow indicates the direction of incidence of the EM wave and the dark arrow shows where the measurement started. Absolute uncertainty of the measured values is ±19 % (EIT).

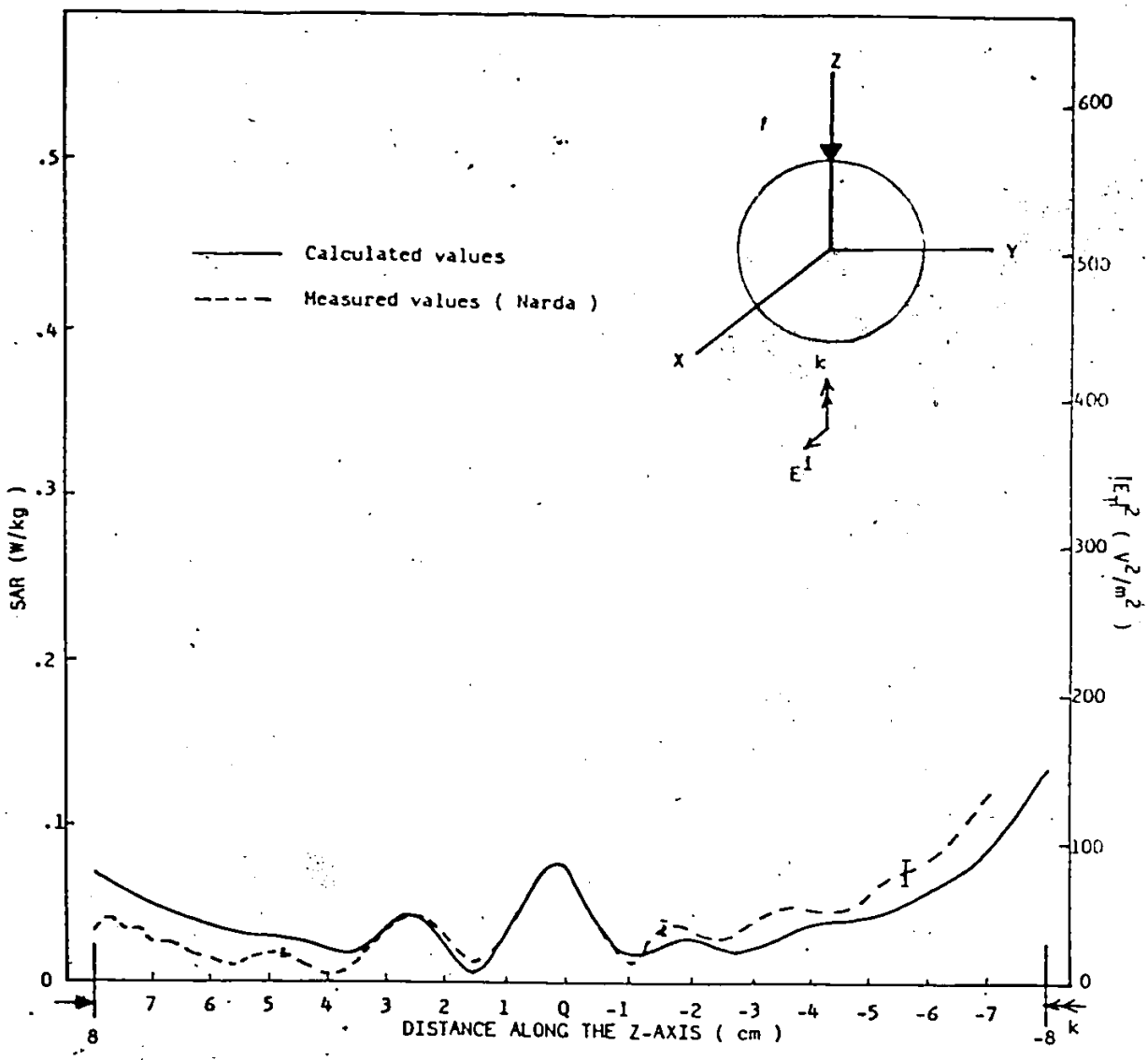

Fig.32: COMPARISON OF THE CALCULATED AND MEASURED SAR AND ELECTRIC FIELD OF THE MUSCLE SALINE SPHERE (ε' = 76.0, σ = 1.58 S/m, f = 920 MHz, Incident Power Density = 1 mW/cm^2, Diameter = 16 cm, Diameter/λ_o = 0.49, and Sensitivity = 0.62 ± .05 μV/(V^2/m^2) (Narda); where the double arrow indicates the direction of incidence of the EM wave and the dark arrow shows where the measurement started. Absolute uncertainty of the measured values is ±11% (Narda).

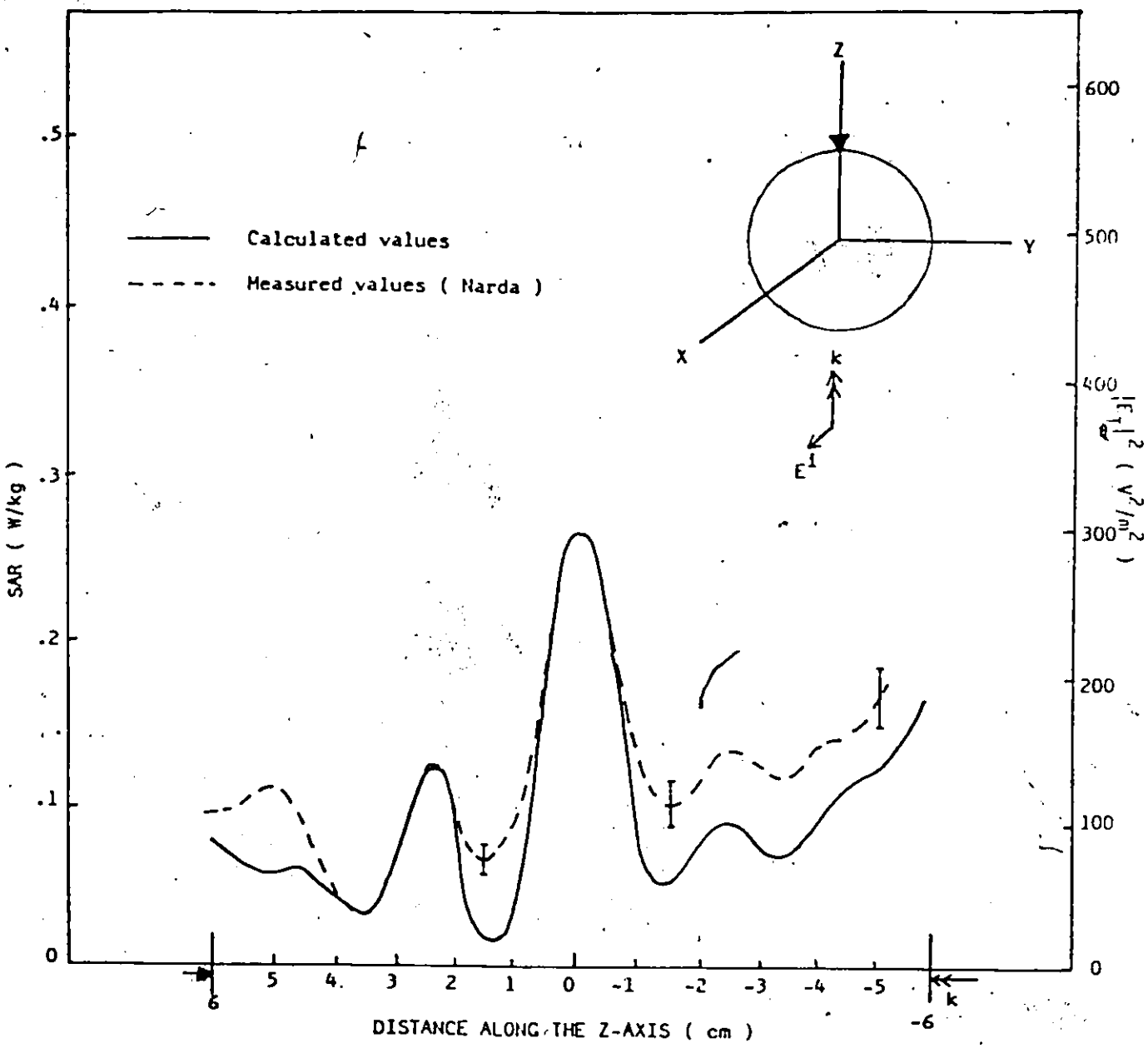

Fig.33: COMPARISON OF THE CALCULATED AND MEASURED SAR AND ELECTRIC FIELD OF THE MUSCLE SALINE SPHERE ($\varepsilon' = 76.0$, $\sigma = 1.58$ S/m, $f = 920$ MHz, Incident Power Density = 1 mW/cm^2, Diameter = 12 cm, Diameter/λ_0 = 0.37, and Sensitivity = 0.67 ± .08 μV/(V^2/m^2) (Narda); where the double arrow indicates the direction of incidence of the EM wave and the dark arrow shows where the measurement started. Absolute uncertainty of the measured values is ±14% (Narda).

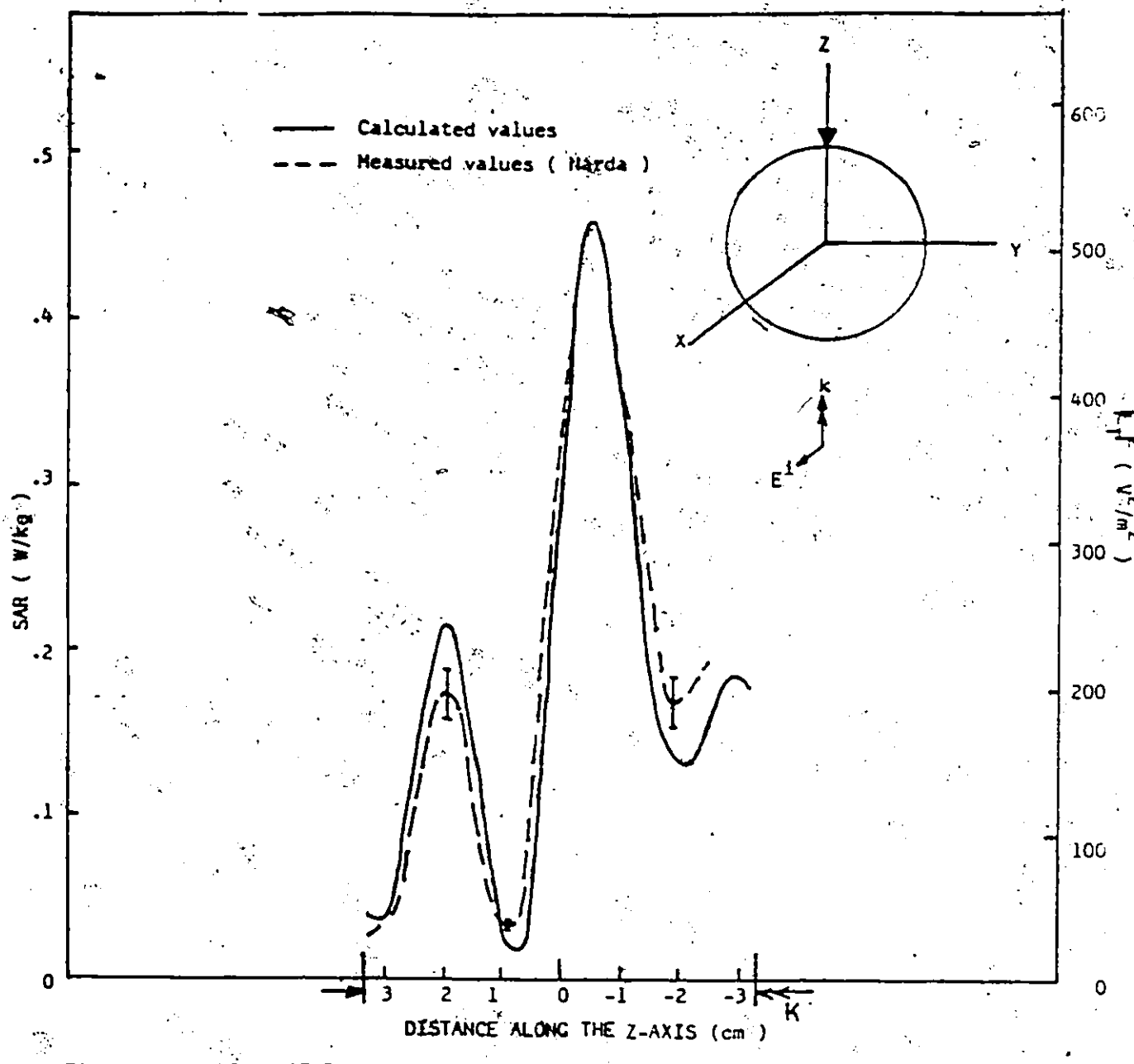

Fig.34: COMPARISON OF THE CALCULATED AND MEASURED SAR AND ELECTRIC FIELD OF THE MUSCLE SALINE SPHERE ($\varepsilon' = 76.0$, $\sigma = 1.58$ S/m, $f = 920$ MHz, Incident Power Density = 1mW/cm^2, Diameter = 6.6 cm, Diameter/λ_o = 0.2, and Sensitivity = 0.67 ± 0.04 μV/(V^2/m^2); where the double arrow indicates the direction of incidence of the EM wave and the dark arrow shows where the measurement started. Absolute uncertainty of the measured values is ±9% (Narda).

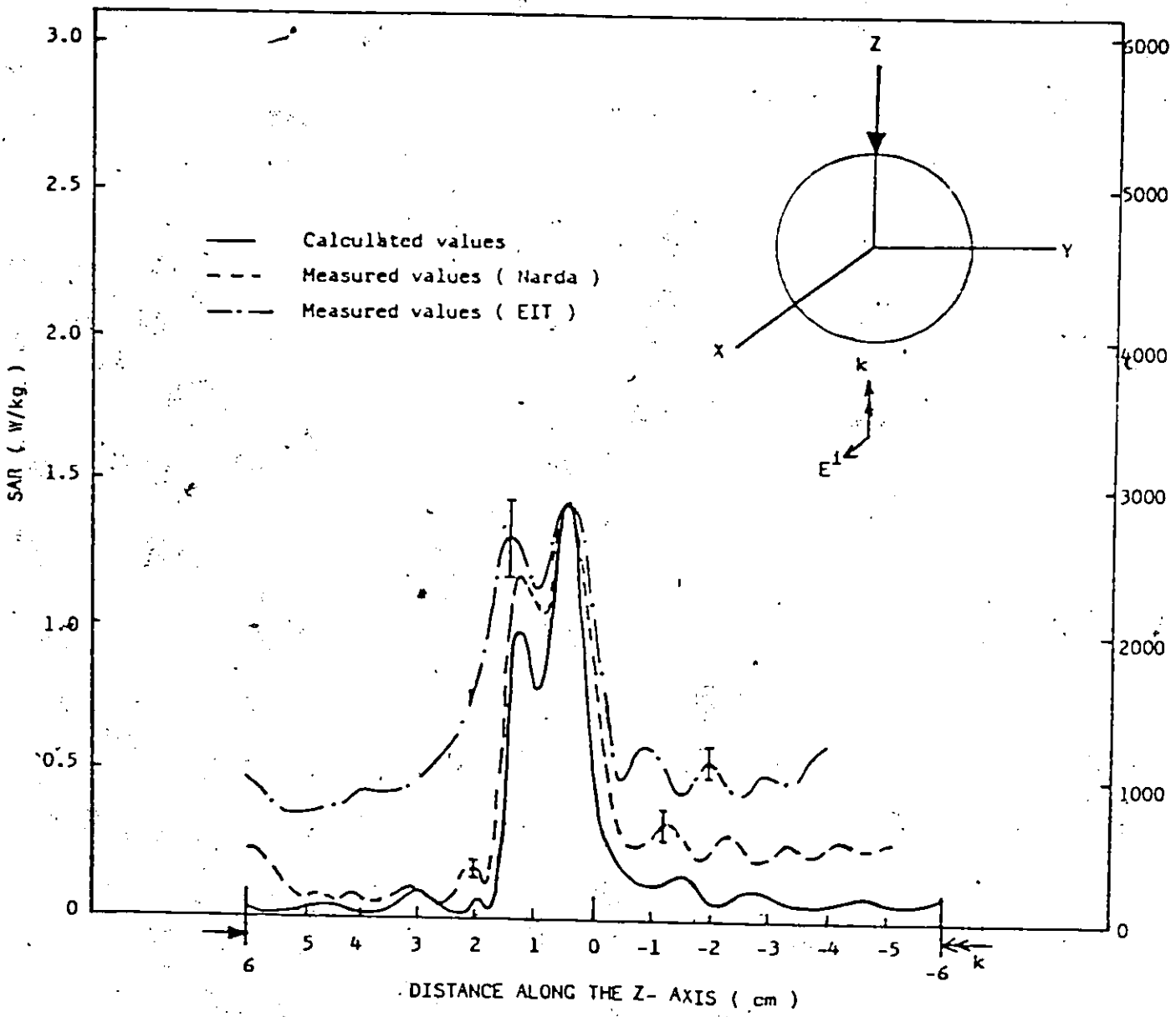

Fig.35: COMPARISON OF THE CALCULATED AND MEASURED SAR AND ELECTRIC FIELD OF THE MUSCLE SALINE SPHERE ($\varepsilon' = 77.9$, $\sigma = 1.02$ S/m, f = 2450 MHz, Incident Power Density = 1 mW/cm^2, Diameter = 12 cm, Diameter/λ_o = 0.98, and Sensitivity = 0.07 ± .01 μV/(V^2/m^2) (Narda), 0.14 ± .01 μV/(V^2/m^2) (EIT); where the double arrow indicates the direction of incidence of the EM wave and the dark arrow shows where the measurement started. Absolute uncertainties of the measured values are ±16% (Narda) and ±10% (EIT).

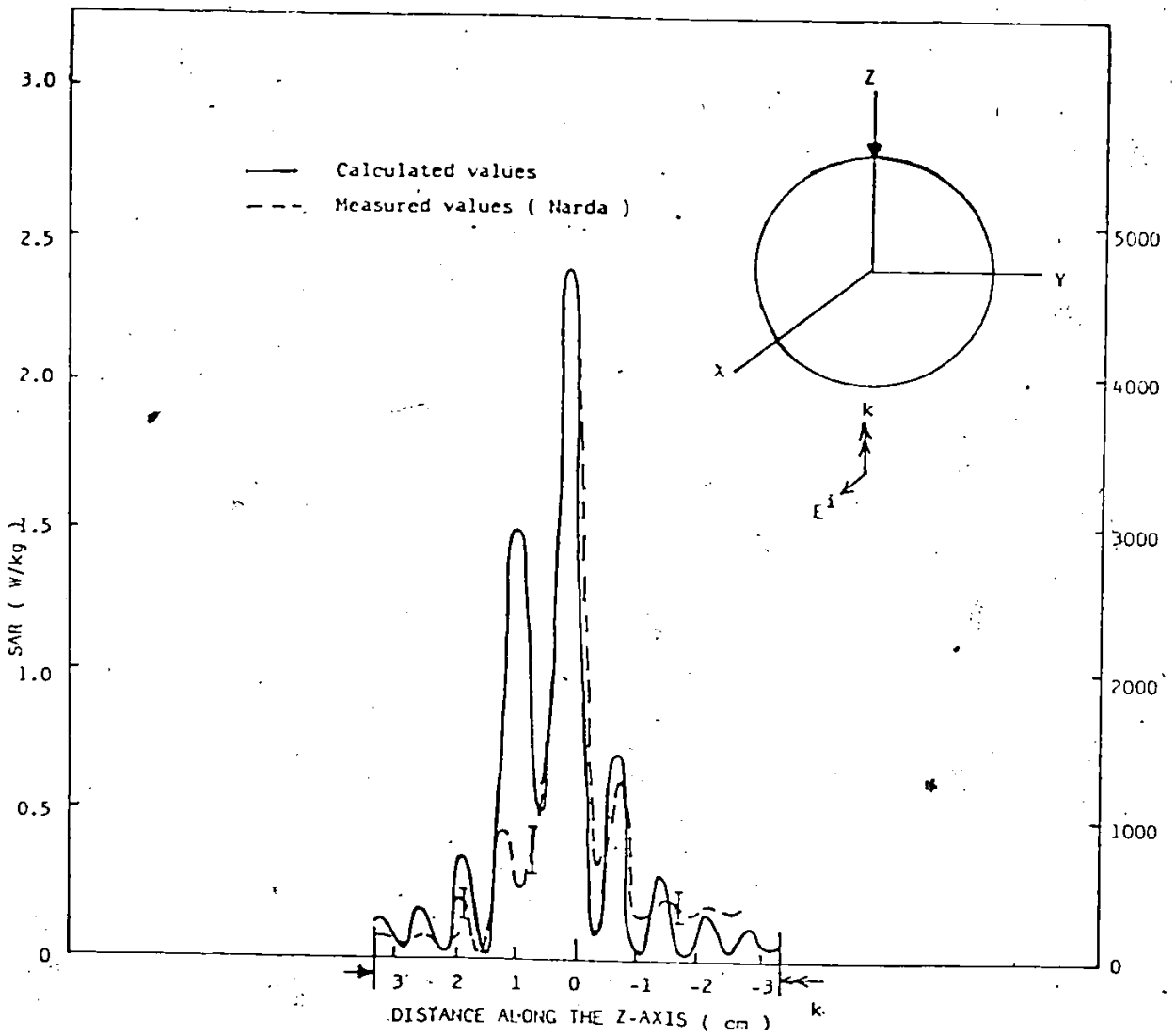

Fig.36: COMPARISON OF THE CALCULATED AND MEASURED SAR AND ELECTRIC FIELD OF THE MUSCLE SALINE SPHERE ($\varepsilon' = 77.9$, $\sigma = 1.02$ S/m, $f = 2450$ MHz, Incident Power Density = 1 mW/cm^2, Diameter = 6.6 cm, Diameter/λ_o = 0.54, and Sensitivity = 0.08 $\pm$ .02 μV/(V^2/m^2) (-Narda); where the double arrow indicates the direction of incidence of the EM wave and the dark arrow shows where the measurement started. Absolute uncertainty of the measured values is ±26% (Narda).

5.3 CYLINDER MODEL

The theoretical SAR distribution across an infinite circular cylinder also agree well with the experimental SAR distributions at the middle section of a finite circular cylinder with $0.29\lambda_o$ in diameter and $2.14\lambda_o$ in length at a frequency of 350 MHz. The comparisons of the calculated and measured results at different sections are given in Figs.37-40 for TM and TE modes.

Figures 37-38 show that there are good correlations between the calculated and measured results at the center section. The discrepancies occurring at the top part of the cylinder are due to the incomplete circular cylinder which was not completely filled to avoid spilling from the openings at the measurement locations. These figures also show the comparison of the measured results at different locations for TM and TE modes. The compared results indicate that reflections from the metallic part of the scanning structure are visible when the incident wave is irradiated towards it. Larger discrepancies occurred in the TM mode, as compared to those in the TE mode, are probably caused by the higher end reflections in this mode.

Similar comparisons are shown in Figs.39-40. These figures show an excellent matching between the calculated and measured results using the EIT probe, except some measured values which are close to the threshold of the sensitivity of the probe.

It was found that the measured results obtained along the direction perpendicular to the propagation axis are more than ten times the maximum of calculated results when the source is positioned on the side of the cylinder. It seems to result from the direct pick-up in the probe and reflections from the scanning unit.

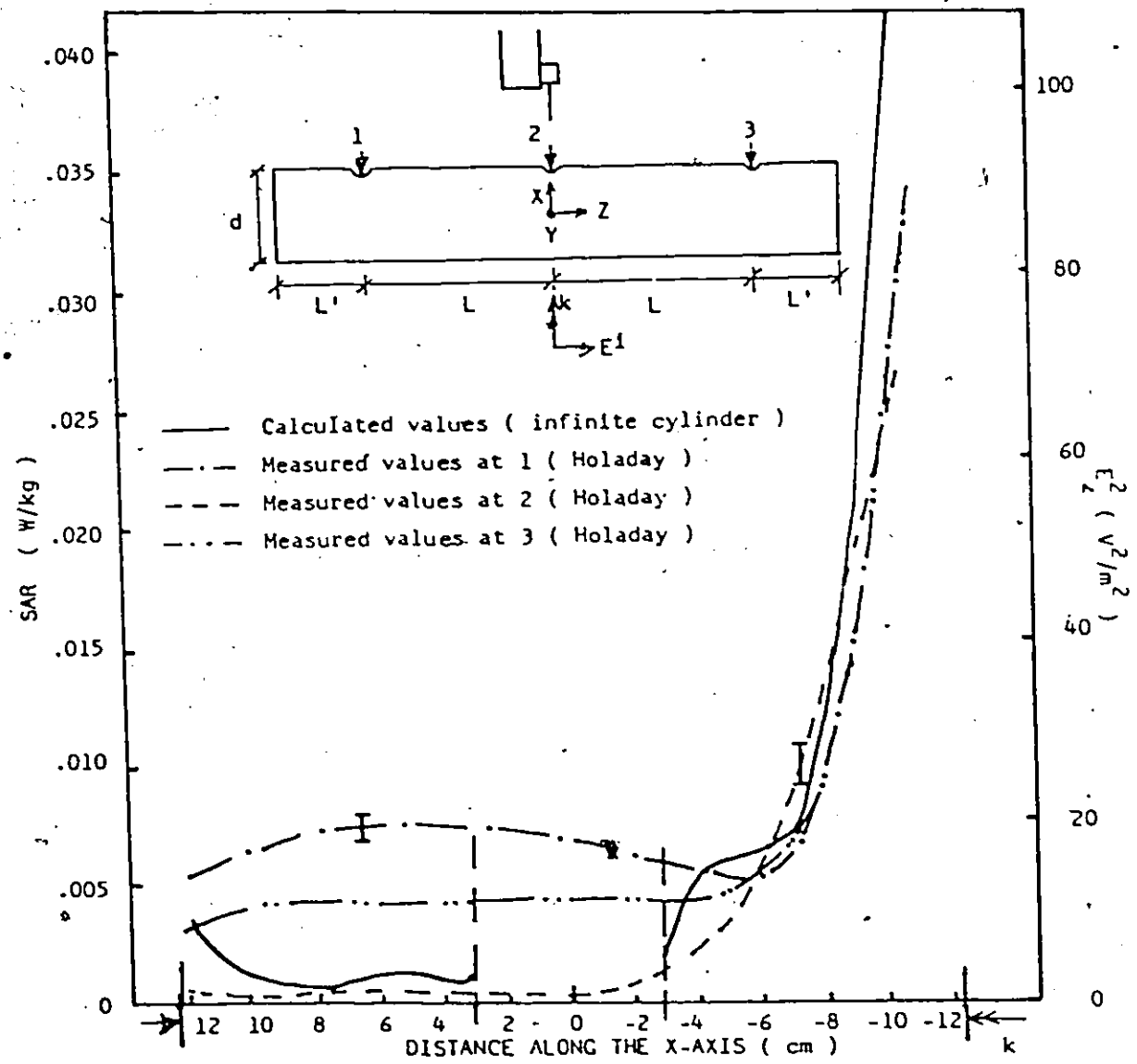

Fig.37: COMPARISON OF THE CALCULATED AND MEASURED SAR AND ELECTRIC FIELD ACROSS A CIRCULAR CYLINDER FILLED WITH THE AVERAGE TISSUE PHANTOM ($\varepsilon' = 38.9$, $\varepsilon'' = 53.5$), TM Mode, $f = 350$ MHz, Incident Power Density = 1 mW/cm^2, $L = 0.62\lambda_o$, $L' = 0.44\lambda_o$, $d = 0.29\lambda_o$, Sensitivity = 20 ± 1 $\mu V/(V^2/m^2)$ (Holaday); where the double arrow indicates the direction of incidence of the EM wave and the dark arrow shows where the measurement started. Absolute uncertainty of the measured values is ±8% (Holaday).

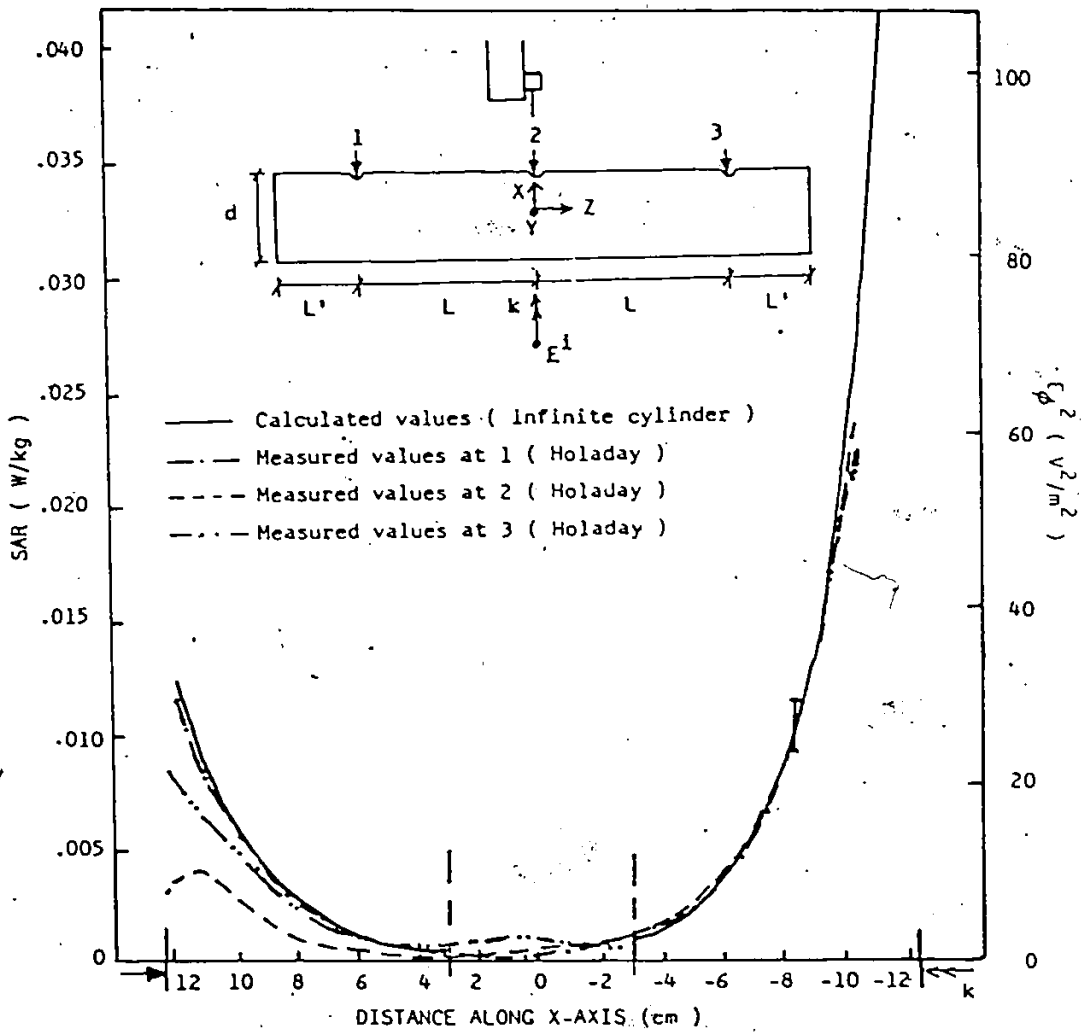

Fig.38: COMPARISON OF THE CALCULATED AND MEASURED SAR AND ELECTRIC FIELD ACROSS A CIRCULAR CYLINDER FILLED WITH THE AVERAGE TISSUE PHANTOM ($\varepsilon' = 38.9$, $\varepsilon'' = 53.5$), TE Mode, f = 350 MHz, Incident Power Density = 1 mW/cm^2, L = $0.62\lambda_o$, L' = $0.44\lambda_o$, d = $0.29\lambda_o$, Sensitvity = 17 $\pm$ 1 $\mu V/(V^2/m^2)$ (Holaday); where the double arrow indicates the direction of incidence of the EM wave and the dark arrow shows where the measurement started. Absolute uncertainty of the measured values is $\pm$9% (Holaday).

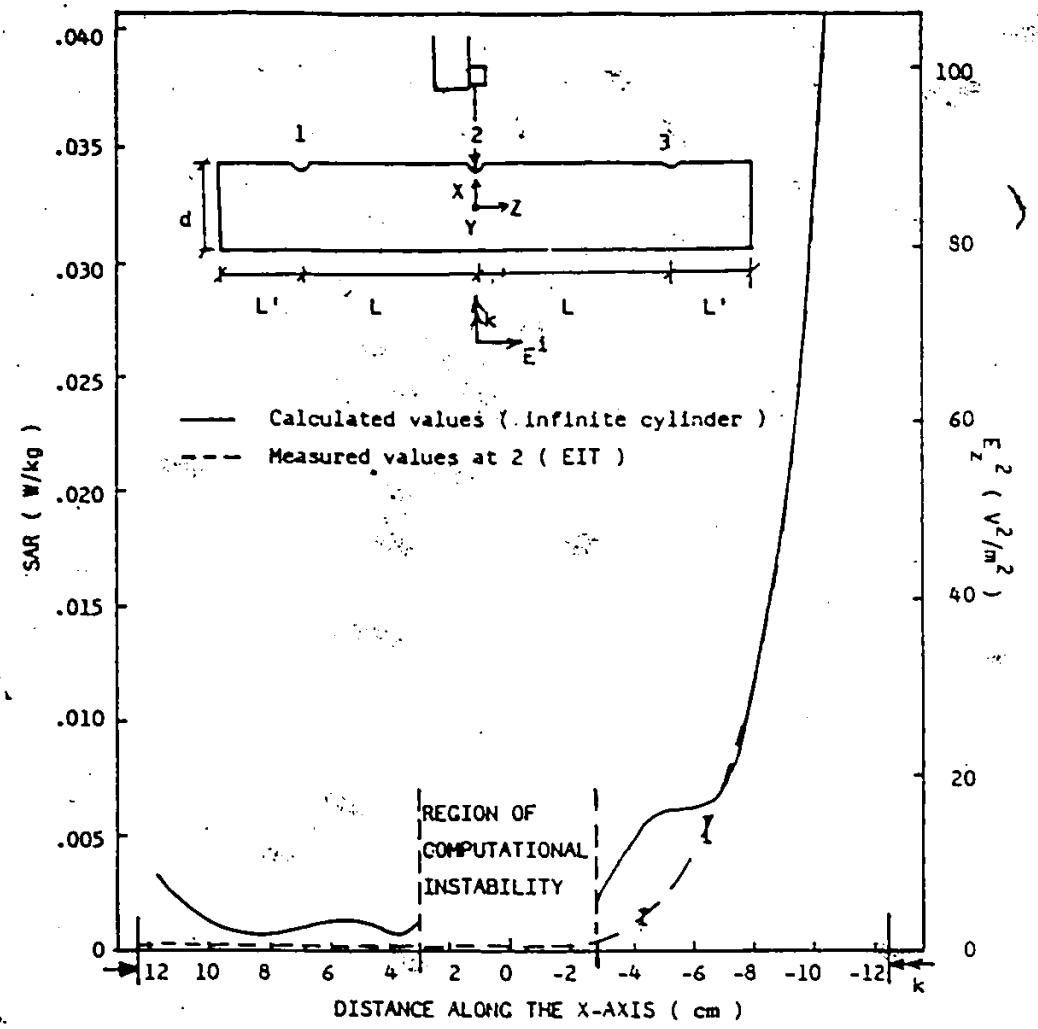

Fig.39: COMPARISON OF THE CALCULATED AND MEASURED SAR AND ELECTRIC FIELD ACROSS A CIRCULAR CYLINDER FILLED WITH THE AVERAGE TISSUE PHANTOM (ε' = 38.9, ε'' = 53.5), TM Mode, f = 350 MHz, Incident Power Density = 1 mW/cm^2, L = 0.62λ_o, L' = 0.44λ_o, d = 0.29λ_o, Sensitivity = 3.0 ± 0.1 $\mu V/(V^2/m^2)$ (EIT); where the double arrow indicates the direction of incidence of the EM wave and the dark-arrow shows where the measurement started. Absolute uncertainty of the measured values is ±8% (EIT).

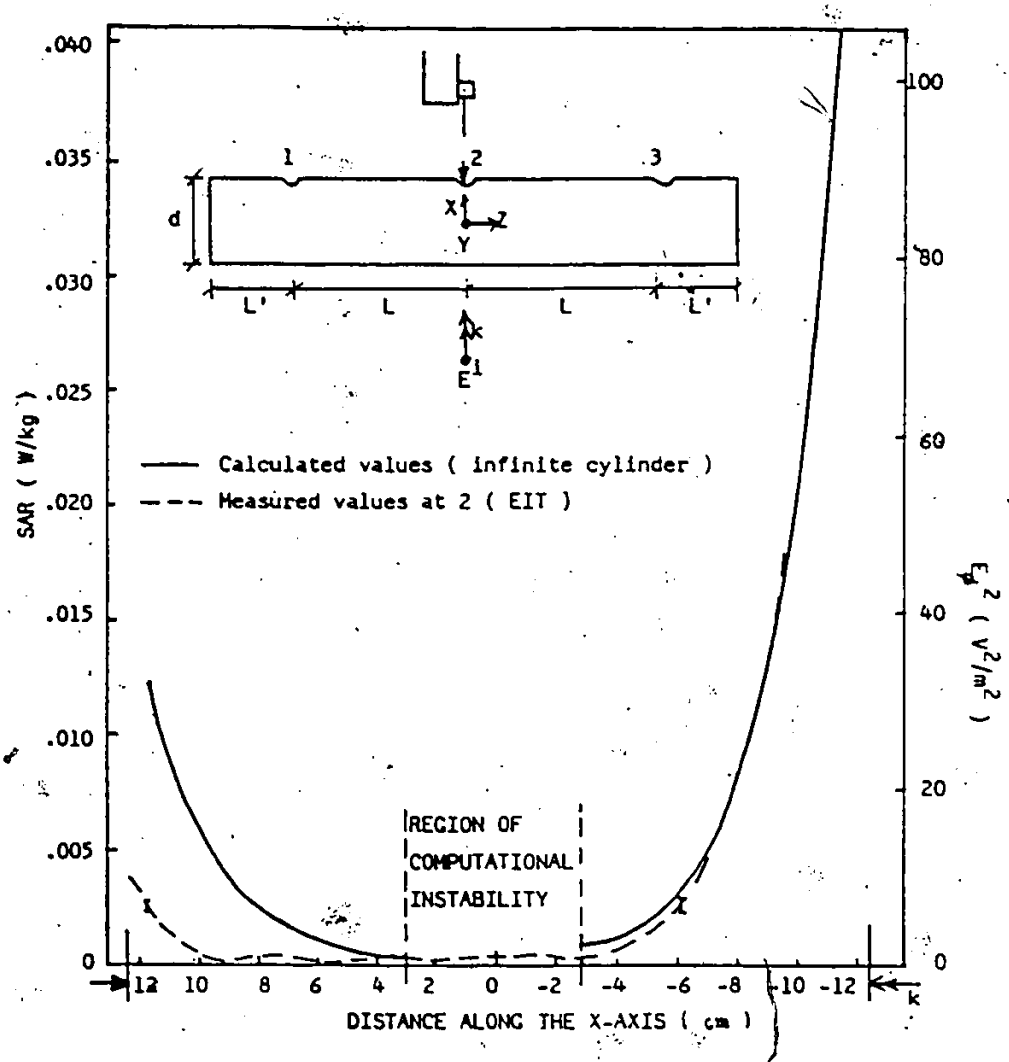

Fig.40: COMPARISON OF THE CALCULATED AND MEASURED SAR AND ELECTRIC FIELD ACROSS A CIRCULAR CYLINDER FILLED WITH THE AVERAGE TISSUE PHANTOM ($\varepsilon' = 38.9$, $\varepsilon'' = 53.5$), TE Mode, f = 350 MHz, Incident Power Density = 1 mW/cm^2, L = $0.62\lambda_o$, L' = $0.44\lambda_o$, d = $0.29\lambda_o$, Sensitivity = 2.8 ± 0.1 $\mu V/(V^2/m^2)$ (EIT); where the double arrow indicates the direction of incidence of the EM wave and the dark arrow shows where the measurement started. Absolute uncertainty of the measured values is ±8% (EIT).

5.4 BLOCK MODELS

In general, large discrepancies in the compared results for the block models occurred. These are due to the incorrect calculated results in some cases and the nonisotopic response of the EIT probe in most cases.

Figures 41-42 show the compared results for two cubes with different sizes and numbers of cell subdivisions. The results for a block model with the smaller thickness and cell size are shown in Fig.43. Aside from the fact that the calculated results in these models are not accurate (i.e. $l.t > 0.065\,\lambda^2$), the calculated SARs are symmetrical with respect to the incident E- and H-field axes while the measured results generally do not show these symmetries. The lack of symmetry is mainly due to the nonisotopic response of the probe in mapping a cross-polarized induced-field distribution and cross polarization of the incident field.

Figure 44 shows the results for the blocks with different cell size and thickness products. Reasonable agreement of the experimental and theoretical results is visible in the section of the block with the smallest cell size and thickness product as shown in the darken box in Fig.44. This may be because an accurate numerical solution is obtained from a cell size and thickness product smaller than $0.065\,\lambda^2$. The large discrepancies shown in the other

sections of this figure are probably caused by the two factors mentioned before (errors in calculations and probe response).

CALCULATED
MEASURED (EIT) (ABSOLUTE UNCERTAINTY = ±10%)

17/77	11/40	10/29	11/41	17/60
29/64	23/46	24/33	23/55	29/57
37/61	30/44	30/31	30/55	37/57
29/74	23/47	24/33	23/50	29/59
17/80	11/43	10/32	11/31	17/41

(1)

18/61	22/32	19/22	22/23	18/29
21/33	25/24	33/21	25/22	21/25
23/21	27/20	40/20	27/20	23/22
21/37	25/26	33/20	25/21	21/21
18/80	22/48	19/33	22/35	18/39

(2)

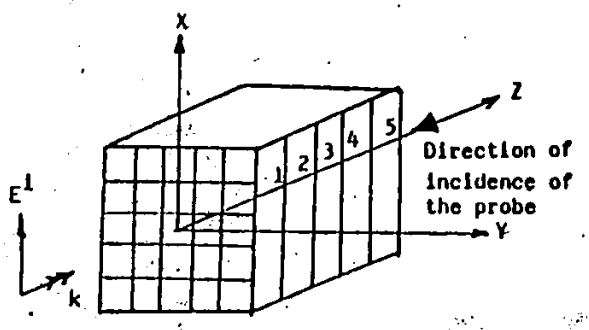

Dimensions: 16cm X 16cm X 16cm
Dimensions/λ : 1.52 X 1.52 X 1.52

f = 350 MHz, $\varepsilon' = 38.9$, $\sigma = 1.04$ S/m,
Incident Power Density = 1 mW/cm^2,
$|k|1 = 1.908$

39/63	52/35	49/24	52/21	39/24
24/24	44/19	60/20	44/13	24/13
21/8	45/12	72/17	45/10	21/9
24/26	44/19	60/18	44/14	24/11
39/74	52/37	49/23	52/26	39/30

(3)

42/65	54/37	51/26	54/25	45/28
11/30	14/17	17/13	14/14	11/19
2/30	5/17	14/6	5/8	2/15
11/26	14/15	17/11	14/12	11/12
45/70	54/34	51/21	54/25	45/26

(4)

26/58	25/34	21/24	25/23	26/31
17/46	22/26	15/19	22/23	17/37
19/35	28/19	20/15	28/22	19/34
17/31	22/14	15/9	22/13	17/22
26/53	25/26	21/17	25/18	26/23

(5)

Fig.41: COMPARISON OF THE CALCULATED AND MEASURED SAR DISTRIBUTION IN mW/kg IN A 16-cm CUBE WITH 125 CELL SUBDIVISIONS

CALCULATED
MEASURED (EIT) (ABSOLUTE UNCERTAINTY = ±10%)

48 41	72 24	55 16	72 17	48 26
32 51	35 59	19 63	35 60	32 55
34 69	36 84	13 96	36 89	34 73
32 63	35 70	19 78	35 76	32 68
48 29	72 20	55 18	72 24	48 38

(2)

65 40	95 23	79 16	95 15	65 15
18 13	19 23	21 28	19 19	18 9
12 15	9 27	11 39	9 28	12 11
18 18	19 21	21 29	19 24	18 14
65 14	95 13	79 12	95 17	65 30

(3)

65 38	88 22	77 15	88 15	65 12
9 9	12 4	19 2	12 1	9 5
1 23	3 2	15 1	3 1	1 13
9 27	12 5	19 1	12 2	9 12
65 16	88 12	77 9	88 15	65 31

(4)

29 29	37 9	35 4	37 7	29 11
18 35	36 22	46 21	36 25	18 38
23 87	45 58	60 51	48 56	23 75
18 74	36 46	46 36	36 37	18 48
29 14	37 10	35 5	37 4	29 19

(5)

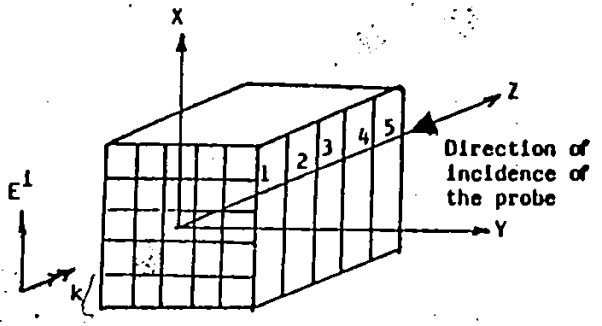

Dimensions: 12cm X 12cm X 12cm

Dimensions/λ : 1.14 X 1.14 X 1.14

f = 350 MHz, ϵ' = 38.9, σ = 1.04 S/m,

Incident Power Density = 1 mW/cm^2,

$|k|1$ = 1.431

Fig.42: COMPARISON OF THE CALCULATED AND MEASURED SAR DISTRIBUTION IN mW/kg IN A 12-cm CUBE WITH 125 CELL SUBDIVISIONS

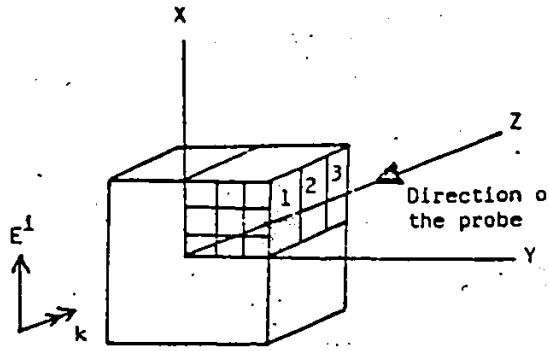

Dimensions: 12cm X 12cm X 6cm

Dimensions/λ : 1.14 X 1.14 X 0.57

f = 350 MHz, ε' = 38.9, σ = 1.04 S/m,

Incident Power Density = 1 mW/cm^2, $|k|$ = 1.193

CALCULATED / MEASURED (EIT)

(ABSOLUTE UNCERTAINTY = ±10%)

21/18	25/16	16/12	16/12	25/16	21/23
23/21	44/19	18/17	18/17	44/18	23/18
28/26	62/23	22/23	22/23	62/22	28/22
28/26	12/22	22/23	22/23	62/22	28/22
23/19	44/19	18/19	18/19	44/19	23/19
21/25	25/19	16/15	16/14	25/16	21/19

(2)

15/15	12/10	17/7	17/7	12/10	15/21
11/7	14/2	36/2	36/2	14/2	11/4
16/15	20/3	55/4	55/5	20/3	16/6
16/15	20/4	55/5	55/6	20/3	16/6
11/8	14/3	36/4	36/4	14/3	11/3
15/18	12/12	17/8	17/6	12/7	15/10

(3)

Fig.43: COMPARISON OF THE CALCULATED AND MEASURED SAR DISTRIBUTION IN mW/kg IN A BLOCK WITH 108 CELL SUBDIVISIONS

CALCULATED
MEASURED (EIT) (ABSOLUTE UNCERTAINTY = ±10%)

10/12	6/8	5/5	6/7	10/16
11/3	6/1	10/3	6/2	11/1
13/3	6/1	14/3	6/2	13/1
11/2	6/1	10/3	6/2	11/1
10/14	6/8	5/4	6/4	10/8

(2)
$|k|1 = 1.431$, $1 \times t = 0.1036\lambda^2$

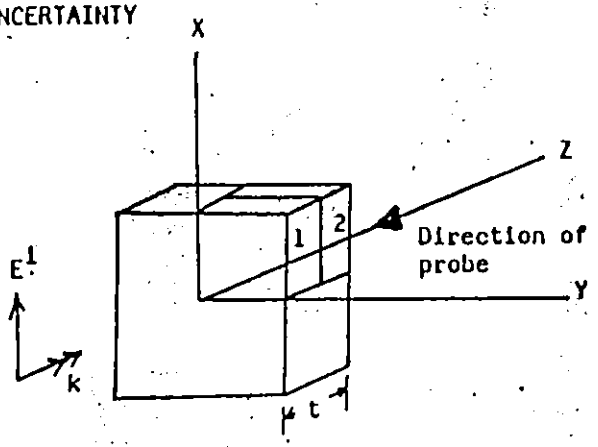

Dimensions: 12cm X 12cm X tcm
Dimensions/λ : 1.14 X1.14 X t'
f = 350 MHz, $\varepsilon' = 38.9$, $\sigma = 1.04$ S/m,
Incident Power Density = 1 mW/cm^2,
$|k| = 59.6$

18/27	17/23	11/22	7/20	7/20	11/54	17/32	18/74
13/25	23/22	17/20	9/19	9/19	17/20	23/22	13/26
13/23	32/23	22/23	10/24	10/23	22/24	32/23	13/23
12/22	37/22	25/24	10/25	10/26	25/26	37/24	12/24
12/18	37/19	25/22	10/23	10/24	25/23	37/21	12/21
13/14	32/15	22/17	10/18	10/18	22/18	32/17	13/17
13/12	23/12	17/12	9/12	9/11	17/12	23/13	13/14
18/18	17/14	11/11	7/9	7/7	11/7	17/10	18/18

(2)
$|k|1 = 0.895$, $1 \times t = 0.040\lambda^2$

9/20	6/12	2/8	2/8	6/12	9/24
6/7	6/6	1/6	1/6	6/6	6/6
5/6	6/4	1/7	1/8	6/6	5/4
5/6	6/3	1/7	1/8	6/5	5/3
6/3	6/3	1/5	1/6	6/4	6/3
9/20	6/10	2/6	2/4	6/5	9/10

(2)
$|k|1 = 1.193$, $1 \times t = 0.072\lambda^2$

Fig.44: COMPARISON OF THE CALCULATED AND MEASURED SAR DISTRIBUTION IN mW/kg IN A BLOCK WITH DIFFERENT THICKNESSES AND DIFFERENT NUMBERS OF CELL SUBDIVISIONS

5.5 EFFECTS OF CROSS POLARIZATION

Due to the shape and symmetry of the spherical model, the cross polarization of the incident field does not affect the SAR distribution along the propagation axis of the sphere since the induced electric field is polarized in the same direction as the incident electric field vector. This cross polarization effect causes a slight change in the SAR distribution in the other two axes of the sphere, since the induced electric field is cross-polarized along the direction of the incident electric field in the sphere. This may explain some of the discrepancies of the experimental results shown in Fig.31.

Since the induced electric field in the cylindrical model is polarized in the same direction as the incident electric field vector, the cross polarization effect also causes a slight change in the measured field intensities.

The cross polarization of the incident field can change both the intensities and the symmetry of the measured field in the block model. These effects are shown in Fig.45.

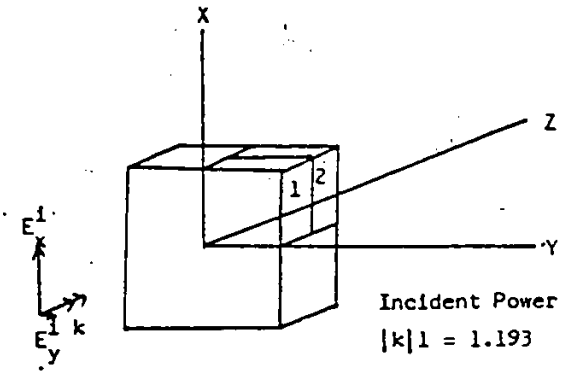

Incident Power Density = 1 mW/cm^2

$|k|1 = 1.193$

Dimensions: 12cm X 12cm X 4cm

Dimensions/λ : 1.14 X 1.14 X 0.38

f = 350 MHz, ε' = 38.9, σ = 1.04 S/m.

100% E^i_x / 90% E^i_x, 10% E^i_y

28/15	32/25	18/20	18/26	32/43	28/41
49/38	78/73	44/50	44/53	78/85	49/56
64/57	112/104	60/60	60/61	112/107	64/63
64/63	112/107	60/61	60/60	112/104	64/57
49/56	78/85	44/53	44/50	78/73	49/38
28/41	32/43	18/26	18/20	32/25	28/15

(1)

9/5	6/5	2/2	2/3	6/8	9/14
6/4	6/6	1/1	1/1	6/7	6/7
5/4	6/6	1/1	1/1	6/6	5/5
5/5	6/6	1/1	1/1	6/6	5/4
6/7	6/7	1/1	1/1	6/6	6/4
9/14	6/8	2/3	2/2	6/5	9/5

(2)

Fig.45: COMPARISON OF THE CALCULATED SAR DISTRIBUTION IN mW/kg IN A BLOCK WITH AND WITHOUT 10% OF CROSS POLARIZATION

5.6 CONCLUSIONS

In this thesis, the numerical and experimental SAR distributions in simple spherical, cylindrical, and block models under plane wave irradiation were compared. The numerical SAR distributions in the spherical and cylindrical models were obtained by solving Maxwell's equations analytically, while those in the block model were obtained by solving the formulated tensor integral equation numerically. The SAR distributions were also measured using an automated scanning system and the electric-field-probe technique.

The analytical results for the sphere and cylinder agreed very well with the experiments. The cylindrical model analysed here can simulate an infinite cylinder in the middle section, while at a distance of $0.44\,\lambda_o$ from the end, the SAR distributions are slightly distorted by the end reflections. The conditions for an accurate numerical solution in the block model by the tensor-integral-equation technique and the moment method were derived from the comparison of the calculated SAR distribution in the block with different cell sizes. It was found that the product of the cell size and thickness along the propagation axis of the block must be smaller than $0.065\,\lambda^2$. Due to the inherent properties of the electric field probes, large discrepancies in the cross-polarized induced-field

measurement, such as those in the block model, occurred. Therefore, the results for the block model cannot be compared and the conditions for the accurate numerical solution cannot be verified by experiments.

The main source of the overall system's experimental errors comes from the field measurements using a nonideal electric field probe. The perturbation of the probe in the field measurement of a given model was proven to be minimal below a certain frequency. Good repeatability in the field measurement of the same measurement set-up was found using the automated scanning system. It is suggested for all other future phantom measurements, in which the induced electric field is polarized at a certain angle with respect to the incident field, a more isotopic triaxial electric field probe should be used.

In this study, the following was accomplished:

- The preparation and implementation of two computer programs for solving the SAR distributions in the cylindrical and block models;
- The electric field measurements in three simple shaped models under the far field irradiation conditions;
- The determination of the practical limitations of the theoretical and experimental analyses of three simple shaped models under plane wave irradiation;

- The evaluation of a part of the automated experimental dosimetric system;
- The calibration of three electric field probes in the tissue equivalent materials and in air at different frequencies;
- The verification of the analytical solution for the SAR distribution in the cylindrical model.

APPENDIX A

DERIVATION OF THE RECURSION EQUATIONS FOR THE INFINITE CIRCULAR CYLINDER

TM Mode:

By applying the boundary conditions, E_z and H_ϕ evaluated in the layers m and m+1, as expressed in Eqns.3 and 4 on P.15 , can be equated respectively as:

$$A_{m+1}J_{m+1} + B_{m+1}Y_{m+1} = A_mJ_m + B_mY_m$$

$$\Leftrightarrow \quad A_{m+1}J_{m+1} = A_mJ_m + B_mY_m - B_{m+1}Y_{m+1} \qquad \text{--- (A-1)}$$

$$\text{and} \quad \frac{k_{m+1}}{\mu_{m+1}} (A_{m+1}J'_{m+1} + B_{m+1}Y'_{m+1}) = \frac{k_m}{\mu_m} (A_mJ'_m + B_mY'_m)$$

$$\Leftrightarrow \quad k_{m+1}\mu_m (A_{m+1}J'_{m+1} + B_{m+1}Y'_{m+1}) = k_m\mu_{m+1} (A_mJ'_m + B_mY'_m) \qquad \text{--- (A-2)}$$

Multiplying A-2 by J_{m+1} gives:

$$k_{m+1}\mu_m (A_{m+1}J'_{m+1}J_{m+1} + B_{m+1}Y'_{m+1}J_{m+1})$$

$$= k_m\mu_{m+1} (A_mJ'_mJ_{m+1} + B_mY'_mJ_{m+1}) \qquad \text{--- (A-3)}$$

Substituting A-1 into A-3 gives:

$$k_{m+1}\mu_m (A_mJ_mJ'_{m+1} + B_mY_mJ'_{m+1} - B_{m+1}Y_{m+1}J'_{m+1} + B_{m+1}Y'_{m+1}J_{m+1})$$

$$= k_m\mu_{m+1} (A_mJ'_mJ_{m+1} + B_mY'_mJ_{m+1})$$

$$\Leftrightarrow \quad k_{m+1}\mu_m (J_{m+1}Y'_{m+1} - J'_{m+1}Y_{m+1}) B_{m+1}$$

$$= (k_m\mu_{m+1}J_{m+1}J'_m - k_{m+1}\mu_mJ'_{m+1}J_m) A_m$$

$$+ (k_m\mu_{m+1}Y'_mJ_{m+1} - k_{m+1}\mu_mY_mJ'_{m+1}) B_m \qquad \text{--- (A-4)}$$

Similarly by isolating $B_{m+1}Y_{m+1}$ in A-1 and repeating the same procedures as above, we get:

$$B_{m+1}Y_{m+1} = A_mJ_m + B_mY_m - A_{m+1}J_{m+1}$$

and $k_{m+1}\mu_m \left(J_{m+1}Y'_{m+1} - J'_{m+1}Y_{m+1} \right) A_{m+1}$

$= \left(k_{m+1}\mu_m J_m Y'_{m+1} - k_m \mu_{m+1} J'_m Y_{m+1} \right) A_m$

$+ \left(k_{m+1}\mu_m Y'_m J_{m+1} - k_m \mu_{m+1} Y_m J'_{m+1} \right) B_m$ --- (A-5)

The recursion equations are obtained by setting:

$A'_{m+1} = k_{m+1}\mu_m \left(J_{m+1}Y'_{m+1} - J'_{m+1}Y_{m+1} \right) A_{m+1}$

$B'_{m+1} = k_{m+1}\mu_m \left(J_{m+1}Y'_{m+1} - J'_{m+1}Y_{m+1} \right) B_{m+1}$

$A'_m = A_m$

$B'_m = B_m$ in Eqns. A-4 & A-5.

The recursion equations are then given as follow;

$$\begin{pmatrix} A'_{m+1,n} \\ B'_{m+1,n} \end{pmatrix} = \begin{pmatrix} U_{mn} & W_{mn} \\ V_{mn} & X_{mn} \end{pmatrix} \begin{pmatrix} A'_{m,n} \\ B'_{m,n} \end{pmatrix}$$

where,

$U_{mn} = \mu_m k_{m+1} J_n(k_m r_m) Y'_n(k_{m+1} r_m) - \mu_{m+1} k_m J'_n(k_m r_m) Y_n(k_{m+1} r_m)$

$V_{mn} = \mu_{m+1} k_m J_n(k_{m+1} r_m) J'_n(k_m r_m) - \mu_m k_{m+1} J'_n(k_{m+1} r_m) J_n(k_m r_m)$

$W_{mn} = \mu_m k_{m+1} Y_n(k_m r_m) Y'_n(k_{m+1} r_m) - \mu_{m+1} k_m Y'_n(k_m r_m) Y_n(k_{m+1} r_m)$

$X_{mn} = \mu_{m+1} k_m Y'_n(k_m r_m) J_n(k_{m+1} r_m) - \mu_m k_{m+1} Y_n(k_m r_m) J'_n(k_{m+1} r_m)$

Now equating coefficients of Eqns. 2 and 3 on P.15 in the outermost boundary of the cylinder, we have:

$C_n = jB_{M+1,n}$ --- (A-7)

$A_{M+1,n} - jB_{M+1,n} = j^{-n} e_n$ --- (A-8)

Lets define a normalization constant K_n for A' and B', such that:

$A_{m,n} = K_n A'_{m,n}$ and $B_{m,n} = K_n B'_{m,n}$

Therefore Eqn. A-8 becomes:

$K_n \left(A'_{M+1,n} - jB'_{M+1,n} \right) = j^{-n} e_n$

$\Leftrightarrow \quad K_n = j^{-n} e_n \; / \; \left(A'_{M+1,n} - jB'_{M+1,n} \right)$

and now we have:

$A_{M,n} = j^{-n} e_n A'_{M,n} \; / \; \left(A'_{M+1,n} - jB'_{M+1,n} \right)$ --- (A-9)

$B_{M,n} = j^{-n} e_n B'_{M,n} \; / \; \left(A'_{M+1,n} - jB'_{M+1,n} \right)$ --- (A-10)

To denormalize the amplitudes, multiply $A_{M,n}$ and $B_{M,n}$ by a factor:

$$\mu_m \left(J_n(R)Y_n'(R) - J_n'(R)Y_n(R) \right) \qquad \text{--- (A-11)}$$

where R = radius of the outermost boundary

To find the unnormalized amplitudes $A'_{M+1,n}$ and $B'_{M+1,n}$ in the outer space of the cylinder, lets define the unnormalized amplitudes in the first layer:

$$A'_{1,n} = (1,0) \qquad \text{and} \qquad B'_{1,n} = (0,0) \qquad \text{for all n}$$

and then step through the layers to the outer space from the recursion equations (A-6).

As the denormalized amplitudes $A_{M,n}$ & $B_{M,n}$ in the outermost layer are found from Eqns. A-9 & A-10, the amplitudes in the subsequent layers can be found by equating coefficients of Eqn. 3 on each boundary:

$$A_{m-1,n} = A_{m,n} \frac{J_n(k_m R_m)}{J_n(k_{m-1} R_m)} \qquad \text{--- (A-12)}$$

$$B_{m-1,n} = B_{m,n} \frac{Y_n(k_m R_m)}{Y_n(k_{m-1} R_m)} \qquad \text{--- (A-13)}$$

TE MODE:

Amplitudes $A_{m,n}$ and $B_{m,n}$ in this case can be obtained from the same procedures as in the TM Mode by interchanging μ & ε, such that the denormalization factor becomes:

$$\varepsilon_m \left(J_n(R)Y_n'(R) - J_n'(R)Y_n(R) \right) \qquad \text{--- (A-14)}$$

APPENDIX B

SPHERICAL VECTOR FUNCTIONS FOR THE SPHERICAL MODEL

Spherical vector functions for the spherical models are expressed as:

$$\bar{m}_{\substack{e\\o}mn} = \mp \frac{m}{\sin\theta} Z_n(\rho)\, P_n^m(\cos\theta) \begin{matrix}\sin\\\cos\end{matrix} m\phi \; \hat{i}_\theta - Z_n(\rho) \frac{\partial P_n^m}{\partial\theta} \begin{matrix}\cos\\\sin\end{matrix} m\phi \; \hat{i}_\phi \qquad \text{--- (B-1)}$$

$$\bar{n}_{\substack{e\\o}mn} = \frac{n(n+1)}{\rho} Z_n(\rho)\, P_n^m(\cos\theta) \begin{matrix}\cos\\\sin\end{matrix} m\phi \; \hat{i}_r + \frac{1}{\rho}\frac{\partial}{\partial\rho}\left[\rho Z_n(\rho)\right] \frac{\partial}{\partial\theta} P_n^m(\cos\theta) \begin{matrix}\cos\\\sin\end{matrix} m\phi \; \hat{i}_\theta \mp \frac{m}{\rho\sin\theta}\frac{\partial}{\partial\rho}\left[\rho Z_n(\rho)\right] P_n^m(\cos\theta) \begin{matrix}\sin\\\cos\end{matrix} m\phi \; \hat{i}_\phi \qquad \text{--- (B-2)}$$

where, $\rho = kr$, $k = \sqrt{\omega\mu\varepsilon + j\omega\mu\sigma}$

$Z_n(\rho)$ is the Spherical Bessel Function

Superscripts 1 and 3 on $\bar{m}$ and $\bar{n}$ indicate whether the Spherical Bessel Function is the first kind $J_n(\rho)$ or the third kind $H_n^{(1)}(\rho)$.

$P_n^m(\cos\theta)$ is the Associated Legendre Polynomials with $m,n \geq 0, 1, 2, \ldots$

Unit rectangular vectors $\hat{i}_x$ and $\hat{i}_y$, when they are transformed into spherical coordinates, are given by:

$$\hat{i}_x = \sin\theta\cos\phi\, \hat{i}_r + \cos\theta\cos\phi\, \hat{i}_\theta - \sin\phi\, \hat{i}_\phi \qquad \text{--- (B-3)}$$

$$\hat{i}_y = \sin\theta\sin\phi\, \hat{i}_r + \cos\theta\sin\phi\, \hat{i}_\theta + \cos\phi\, \hat{i}_\phi \qquad \text{--- (B-4)}$$

The coefficients for Eqns.12 and 13 on P.20in region p in terms of the coefficients in the adjacent p+1 region are given as follows:

$$a_n^p = \frac{1}{\Delta_n^p}\left[\left(\rho_n^p J_n^{p+1} - \tau^p H_n^p \eta_n^{p+1} \right) a_n^{p+1} + \left(\rho_n^p H_n^{p+1} - \tau^p H_n^p \rho_n^{p+1} \right) \alpha_n^{p+1} \right]$$

$$\alpha_n^p = \frac{1}{\Delta_n^p}\left[\left(\tau^p J_n^p \eta_n^{p+1} - \eta_n^p J_n^{p+1} \right) a_n^{p+1} + \left(\tau^p J_n^p \rho_n^{p+1} - \eta_n^p H_n^{p+1} \right) \alpha_n^{p+1} \right]$$

$$b_n^p = \frac{1}{\Delta_n^p}\left[\left(\tau^p \xi_n^p J_n^{p+1} - H_n^p \eta_n^{p+1}\right) b_n^{p+1} + \left(\tau^p \xi_n^p H_n^{p+1} - H_n^p \xi_n^{p+1}\right) \beta_n^{p+1}\right]$$

$$\beta_n^p = \frac{1}{\Delta_n^p}\left[\left(J_n^p \eta_n^{p+1} - \tau^p \eta_n^p J_n^{p+1}\right) b_n^{p+1} + \left(J_n^p \xi_n^{p+1} - \tau^p \eta_n^p H_n^{p+1}\right) \beta_n^{p+1}\right]$$

--- (B-5)

where,

$$\Delta_n^p = J_n^p \xi_n^p - H_n^p \eta_n^p \; ; \quad \tau^p = \frac{k^{p+1}}{k^p} \frac{\mu^p}{\mu^{p+1}}$$

$$J_n^p = J_n(\varsigma^p) \; ; \quad H_n^p = H_n(\varsigma^p)$$

$$\xi_n^p = \frac{1}{\varsigma^p} \frac{\partial}{\partial \varsigma^p} \left(\varsigma^p H_n^p\right)$$

$$\eta_n^p = \frac{1}{\varsigma^p} \frac{\partial}{\partial \varsigma^p} \left(\varsigma^p J_n^p\right) \; ; \quad \varsigma^p = k^p r^p$$

Constraints on the coefficients in equations (B-5) are:

$$\alpha_n' = \beta_n' = 0 \quad \text{(finiteness at the origin)}$$

$$a_n^N = b_n^N = 1 \; .$$

APPENDIX C

FORMULATION OF THE TENSOR INTEGRAL EQUATION FOR THE BLOCK MODEL

Principal value of an integral is defined as:

$$PV\int_{-A}^{B} f(x)dx = \lim_{\xi \to 0}\left[\int_{-A}^{-\xi} f(x)dx + \int_{\xi}^{B} f(x)dx\right],$$

where $f(x)$ is not continuous at $x=0$.

From Eqn.17 on P.24 , the inner product of the integral is given by:

$$E(r')G(r,r') = \begin{bmatrix} G_{xx}(r,r') & G_{xy}(r,r') & G_{xz}(r,r') \\ G_{yx}(r,r') & G_{yy}(r,r') & G_{yz}(r,r') \\ G_{zx}(r,r') & G_{zy}(r,r') & G_{zz}(r,r') \end{bmatrix} \bullet \begin{bmatrix} E_x(r') \\ E_y(r') \\ E_z(r') \end{bmatrix} \qquad \text{--- (C-1)}$$

where the free space tensor Green's function is given by:

$$G(r,r') = -j\omega\mu_o\left[1 + \frac{\nabla\nabla}{k_o^2}\right]\Psi(r,r') \qquad \text{--- (C-2)}$$

$$\Psi(r,r') = \frac{\exp\left(-jk_o|r - r'|\right)}{4\pi|r - r'|} \quad ; \quad r \neq r' \qquad \text{--- (C-3)}$$

$$k_o = \omega\sqrt{\mu_o\varepsilon_o}$$

To simplify the symbols, lets change the rectangular coordinates x, y, and z to x_1, x_2, and x_3, respectively; so that

$x = x_1$, $y = x_2$, and $z = x_3$; then Eqn.C-2 becomes:

$$G_{x_p x_q}(r,r') = -j\omega\mu_o\left[\delta_{pq} + \frac{1}{k_o^2}\frac{\partial^2}{\partial x_p \partial x_q}\right]\Psi(r,r') \quad ; \quad p,q = 1, 2, 3 \qquad \text{--- (C-4)}$$

The Kronecker Delta function δ_{pq} is defined as:

$$\delta_{pq} = \begin{cases} 1 & \text{if } p = q \\ 0 & \text{if } p \neq q \end{cases}$$

Since the matrix in C-1 is symmetric, each component of Eqn.17 may be written as:

$$\left[1 + \frac{\tau(r)}{3j\omega\varepsilon_o}\right] E_{x_p}(r) - PV\int_V \tau(r')\left[\sum_{q=1}^{3} G_{x_p x_q}(r,r') E_{x_q}(r')\right] dV'$$

$$= E^i_{x_p}(r) \quad ; \qquad p = 1, 2, 3 \qquad \text{--- (C-5)}$$

By applying the moment method, Eqn.C-5 can be transformed into a matrix equation.

The total field is expanded using a pulse function as follows:

$$E = \sum_{n=1}^{N} E_n P_n \quad ; \qquad P_n = \begin{cases} 1 & \text{inside the cell n} \\ 0 & \text{elsewhere} \end{cases} \qquad \text{--- (C-6)}$$

Now the body is divided into N cells.

Assume E and τ does not vary inside the cell, therefore Eqn.C-5 becomes:

$$\left[1 + \frac{\tau(r)}{3j\omega\varepsilon_o}\right] E_{x_p}(r) - \sum_{q=1}^{3}\sum_{n=1}^{N} \tau(r_n) E_{x_q,n}(r_n)\, PV\int_{V_n} G_{x_p x_q}(r,r')dV'$$

$$= E^i_{x_p}(r) \quad ; \qquad p = 1, 2, 3 \qquad \text{--- (C-7)}$$

Using $\delta(x - x_m, y - y_m, z - z_m)$ for testing or by Collocation Method (i.e. to replace all the terms which are functions of x, y, and z by the values of the terms evaluated at the point m, which is the centre of the cell), Eqn.C-7 becomes:

$$\left[1 + \frac{\tau(r_m)}{3j\omega\varepsilon_o}\right] E_{x_p}(r_m) - \sum_{q=1}^{3}\sum_{n=1}^{N}\left[\tau(r_n)\, PV\int_{V_n} G_{x_p x_q}(r_m,r')dV'\right] E_{x_q}(r_n)$$

$$= E^i_{x_q}(r_m) \quad ; \qquad m = 1, 2, 3, \ldots, N, \quad p = 1, 2, 3 \qquad \text{--- (C-8)}$$

Lets define :

$$\bar{G}^{mn}_{x_p x_q} = \tau(r_n)\, PV\int_{V_n} G_{x_p x_q}(r_m,r')dV' \qquad \text{--- (C-9)}$$

so that Eqn.C-8 can be rewritten as:

$$\sum_{q=1}^{3}\sum_{n=1}^{N}\left[G_{x_p x_q}^{mn} - \delta_{pq}\delta_{mn}\left(1 + \frac{\gamma(r_m)}{3j\omega\varepsilon_o}\right)\right]E_{x_q}(r_n) = -E_{x_p}^{i}(r_m)\ ;$$

$$m = 1, 2, \ldots, N\ ; \quad p = 1, 2, 3 \qquad \text{--- (C-10)}$$

Let $\left[G_{x_p x_q}\right]$ be a NXN matrix, whose elements are given by:

$$G_{x_p x_q}^{mn} = G_{x_p x_q}^{mn} - \delta_{pq}\delta_{mn}\left[1 + \frac{\gamma(r_m)}{3j\omega\varepsilon_o}\right] \qquad \text{--- (C-11)}$$

and let $\left[E_{x_p}\right]$ and $\left[E_{x_p}^{i}\right]$ be NX1 matrices as defined by:

$$\left[E_{x_p}\right] = \begin{bmatrix} E_{x_p}(r_1) \\ \vdots \\ E_{x_p}(r_N) \end{bmatrix} \quad \text{and} \quad \left[E_{x_p}^{i}\right] = \begin{bmatrix} E_{x_p}^{i}(r_1) \\ \vdots \\ E_{x_p}^{i}(r_N) \end{bmatrix} \qquad \text{--- (C-12)}$$

$p = 1, 2, 3$

The matrix representation of Eqn.17 can now be obtained by ranging m and p over all possible values:

$$\begin{bmatrix} G_{xx} & G_{xy} & G_{xz} \\ G_{yx} & G_{yy} & G_{yz} \\ G_{zx} & G_{zy} & G_{zz} \end{bmatrix}\begin{bmatrix} E_x \\ E_y \\ E_z \end{bmatrix} = -\begin{bmatrix} E_x^i \\ E_y^i \\ E_z^i \end{bmatrix} \qquad \text{--- (C-13)}$$

Symbolic representation of Eqn.C-13 is given as:

$$\left[G\right]\left[E\right] = -\left[E^i\right] \qquad \text{--- (C-14)}$$

Size of the Matrix $\left[G\right]$ equals 3NX3N and size of the matrices $\left[E\right]$ and $\left[E^i\right]$ equals 3N.

In the calculation of the off-diagonal coefficients of the Matrix $\left[G\right]$, we can omit the PV operation in the volume integral, since $r_m \notin V_n$ and $G_{x_p x_q}(r_m, r')$ is continuous throughout V_n.

Therefore from Eqn.C-9 and C-11, we obtain the off-diagonal coefficients of the matrix G expressed as:

$$G_{x_p x_q}^{mn} = \tau(r_n) \int_{V_n} G_{x_p x_q}(r_m, r')dV' \quad , \qquad m \neq n \qquad \text{--- (C-15)}$$

As a first approximation, we have:

$$G_{x_p x_q}^{mn} = \tau(r_n) G_{x_p x_q}(r_m, r_n) \Delta V_n \quad , \quad m \neq n \; ; \qquad \text{--- (C-16)}$$

where $\Delta V_n = \int_{V_n} dV'$ is the volume of the cell n.

Evaluating $G_{x_p x_q}(r_m, r_n)$ from Eqn.C-4 gives:

$$G_{x_p x_q}^{mn} = \frac{- j\omega\mu_o k_o \tau(r_n) \Delta V_n \exp(-j\alpha_{mn})}{4\pi\alpha_{mn}^3} \cdot \left[(\alpha_{mn}^2 - 1 - j\alpha_{mn}) \delta_{pq} + \cos\theta_{x_p}^{mn} \cos\theta_{x_q}^{mn} (3 - \alpha_{mn}^2 + 3j\alpha_{mn}) \right] ,$$

$m \neq n$;

where $\alpha_{mn} = k_o R_{mn}$; $R_{mn} = |r_m - r_n|$

$$\cos\theta_{x_p}^{mn} = \frac{(x_p^m - x_p^n)}{R_{mn}} \; ; \quad \cos\theta_{x_q}^{mn} = \frac{(x_q^m - x_q^n)}{R_{mn}}$$

$r_m = (x_1^m, x_2^m, x_3^m)$ and $r_n = (x_1^n, x_2^n, x_3^n)$

--- (C-17)

For the diagonal matrix coefficients, Eqn.C-15 becomes:

$$G_{x_p x_q}^{nn} = \tau(r_n) \; PV \int_{V_n} G_{x_p x_q}(r_n, r')dV' - \delta_{pq} \left[1 + \frac{\tau(r_n)}{3j\omega\varepsilon_o} \right] \qquad \text{--- (C-18)}$$

The volume integral in Eqn.C-18 can be evaluated analytically by replacing V_n of the cell n with a sphere of equal volume centered at r_n.

The expression for the diagonal coefficients, as derived by Livesay and Chen [29], is given by:

$$G^{nn}_{x_p x_q} = \delta_{pq}\left\{\frac{-2j\omega\mu_o\mathcal{V}(r_n)}{3k_o^2}\left[\exp(-jk_o a_n)(1 + jk_o a_n) - 1\right] - \left[1 + \frac{\mathcal{V}(r_n)}{3j\omega\varepsilon_o}\right]\right\}$$

where $a_n = \left(\frac{3\Delta V_n}{4\pi}\right)^{1/3}$ is the equivalent radius of a sphere centered at cell n.

----- (C-1)

Appendix D

RECIPE FOR PREPARING 350 MHZ AVERAGE TISSUE PHANTOM

Phantom material simulating the electrical properties of average human tissue at 350 MHz can be prepared as follows:

Composition in percentage by weight:

water	salt	sugar	Tx150
37.04%	8.33%	50.93%	3.70%

Electrical parameters:

$\varepsilon' = 38.86$, $\varepsilon'' = 53.46$, and $\sigma = 1.04$ S/m.

Physical parameter:

Density $\rho = 1.355$ g/cc.

Direction for Preparation:

Dissolve the proper amount of salt and sugar in water at 60-65 °C, while continuous stirring, until the solution is clear. Turn the heat off and add the correct amount of Tx150, while stirring. Let the solution cool down to room temperature, and then measure the permittivity of the phantom. If the dielectric constant and conductivity are too

low, add a slight amount of water and mix well before repeating the permittivity measurement. The drop in permittivity is mainly due to the water evaporated in the mixing process.

REFERENCES

1. P.Barber and C.Yeh,"Scattering of Electromagnetic Waves by Arbitrady Shaped Dieletric Bodies," Applied Optics, vol.14, no.12, Dec.1975, pp.2864-2872

2. P.W.Barber,"Resonance Electromagnetic Absorption by Nonspherical Dielectric Objects," IEEE Trans. on MTT, vol.MTT-25, May.1977, pp.373-381

3. P.W.Barber, O.P.Gandhi, M.J.Hagmann, and I.Chatterjee, "Electromagnetic Absorption in a Multilayered model of man," IEEE Trans. on BME, vol.BME-26, 1979, pp.400-404

4. M.Barski, B.Tam, S.S.Stuchly, G.Hartgrove, and S.Symons, "A Computer Based Scanning System for Electromagnetic Dosimetry," submitted to Review of Scientific Instruments, Nov.1982

5. H.Bassen, W.Herman and R.Hoss,"EM Probe with Fiber Optic Telemetry System," Microwave Journal, April 1977

6. B.D.Blanco and C.R-Sierra,"Microwave Radiation Pattern Measurements in the presence of Biological Specimens," IEEE Trans. on EMC, vol.EMC-20(1, Part 2), 1978, pp.248-258

7. H.E.Bussey and J.H.Richmond,"Scattering by A Lossy Dielectric Circular Cylindrical Multilayer, Numerical values," IEEE Trans. on Ant. and Propag., Sep.1975, pp.723-725

8. I.Chatterjee, M.J.Hagmann, and O.P.Gandhi, "Electromagnetic Energy Deposition in an Inhomogeneous Block Model of Man for Near-Field Irradiation Conditions," presented at the IEEE/MTT-S Internation Microwave Symposium, Wash. D.C., May.28-30, 1980

9. I.Chatterjee, M.J.Hagmann, and O.P.Gandhi, "Electromagnetic Energy Deposition in an Inhomogeneous Block Model of Man for Near-Field Irradiation Conditions," IEEE Trans. on MTT, vol.MTT-28, no.12, Dec.1980, pp.1452-1459

10. K.M.Chen and B.S.Guru,"Internal EM Field and Absorbed Power Density in Human Torsos Induced by 1-500-MHz EM Waves," IEEE Trans. on MTT, vol.MTT-25, no.9, Sep.1977, pp.746-756

11. D.A.Christensen and C.H.Durney,"Hyperthermia Production for Cancer Therapy: A Review of Fundamentals and Methods," The Journal of Microwave Power, vol.16, no.2, Jun.1981, pp.89-105

12. D.A.Christensen and R.J.Volz,"A Nonperturbing Temperature Probe System designed for Hyperthermia Monitoring," Abstract of National Radio Science Meeting, Bioelectromagnetics Symposium, Univ. of Washington, Seattle, Washington, 1979

13. C.K.Chou and A.W.Guy,"Effects of Electromagnetic Fields on Isolated Nerve and Muscle preparations," IEEE Trans. on MTT, vol.MTT-26(3), 1978, 141-147

14. C.H.Durney,"Electromagnetic Dosimetry for Models of Humans and Animals: A Review of Theoretical and Numerical Techniques," Proceeding of IEEE, vol.68, no.1, Jan.1980, pp.33-39

15. C.H.Durney, C.C.Johnson, and H.Massoudi, "An Empirical Formular for Broad-band SAR Calculation of Prolate Spheroidal Models of Humans and Animals," IEEE Trans. on MTT, vol.MTT-27, 1979, pp.758-763

16. C.H.Durney, C.C.Johnson, and H.Massoudi, "Long-Wavelength Analysis of Plane Wave Irradiation of a Prolate Spheroidal Model of Man," IEEE Trans. on MTT,vol.MTT-23, no.2, Feb.1975, pp.246-253

17. A.W.Guy,"Analysis of Electromagnetic Fields Induced in Biological Tissues by Thermographic Studies on Equivalent Phantom Models," IEEE Trans. on MTT, vol.MTT-19, 1971, pp.205-214

18. M.J.Hagmann, O.P.Gandhi, and C.H.Durney, "Upper Bound on Cell Size for Moment-Method Solution," IEEE Trans. on MTT, vol.MTT-25, no.10, Oct.1977, pp.831-832

19. M.J.Hagmann, O.P.Gandhi, and C.H.Durney, "Improvement of Convergence in Moment-Method Solutions by the Use of Interpolants," IEEE Trans. on MTT, vol.MTT-26, no.11, Nov.1978, pp.904-908

20. M.J.Hagmann, O.P.Gandhi, and C.H.Durney, "Numerical Calculation of Electromagnetic Energy Deposition for a Realistic Model of Man," IEEE Trans. on MTT, vol.MTT-27, no.9, Sep.1979, pp.804-809

21. M.J.Hagmann, O.P.Gandhi, J.A.D'Andrea, and I.Chatterjee, "Head Resonance: Numerical Solutions and Experimental Results," IEEE Trans. on MTT, vol.MTT-27, no.9, Sep.1979, pp.809-1034

22. D.Hill,"Waveguide Technique for the Calibration of Miniature Implantable Electric-Field Probes for Use in Microwave-Bioeffects Studies" IEEE Trans. on MTT, vol.MTT-30, no.1, Jan.1982, pp.93-99

23. A.Hizal and Y.K.Baykal, "Heat Potential Distribution in an Inhomogeneous Spherical Model of a Cranial Structure Exposed to Microwaves Due to Loop or Dipole Antennas," IEEE Trans. on MTT, vol.MTT-26, no.8, Aug.1978, pp.607-612

24. H.S.Ho and M.McManaway,"Heat Dissipation Rate of Mice after Microwave Irradiation," J.Microwave Power, vol.12(1), 1977, pp.93-100

25. M.F.Iskander, P.W.Barber, C.H.Durney, and H.Massoudi, "Irradiation of Prolate Spheroidal Models of Humans in the Near Field of a Short Electric Dipole," IEEE Trans. on MTT, vol.MTT-28, no.7, Jul.1980, pp.801-807

26. A.Kraszewski, M.A.Stuchly, and S.S.Stuchly,"ANA Calibration Method for Measurement of Dielectric Properties," IEEE Trans. vol.IM-32(2), 1983

27. A.Lakhtakia, M.F.Iskander, C.H.Durney, and H.Massoudi, "Near-Field Absorption in Prolate Spheroidal Models of Humans Exposed to a Small Loop Antenna of Arbitrary Orientation," IEEE Trans. on MTT, vol.MTT-29, no.6, Jun.1981, pp.588-594

28. J.C.Lin, A.W.Guy, and C.C.Johnson, "Power Deposition in a Spherical Model of Man Exposed to 1-20-MHz Electromagnetic Fields," IEEE Trans. on MTT, vol.MTT-21, no.12, Dec.1973, pp.791-797

29. D.E.Livesay and K.M.Chen, "Electromagnetic Fields Induced Inside Arbitrarily Shaped Biological Bodies," IEEE Trans. on MTT, vol.MTT-22, no.12, Dec.1974, pp.1273-1280

30. H.Massoudi, C.H.Durney, and C.C.Johnson, "A Geometrical-optics and an Exact Solution for Internal Fields in and Energy Absorption by a Cylindrical Model of Man Irradiated by an Electromagnetic Plane Wave," Radio Science vol.14, No.6S, Nov.-Dec.1979, pp.35-42

31. H.Massoudi, C.H.Durney, and C.C.Johnson, "Long-Wavelength Analysis of Plane Wave Irradiation of an Ellipsoidal Model of Man," IEEE Trans. on MTT, vol.MTT-25, no.1, Jan.1977, pp.41-46

32. H.Massoudi, C.H.Durney, and C.C.Johnson, "Long-Wavelength Electromagnetic Power Absorption in Ellipsoidal Models of Man and Animals," IEEE Trans. on MTT, vol.MTT-25, no.1, Jan.1977, pp.47-52

33. H.Massoudi, C.H.Durney, and C.C.Johnson, "Long-Wavelength Analysis of Near-field Irradiaion of Prolate Spheroidal Models of Man and Animals," Electron Letter, vol-16(3), 1980, pp.99-100

34. H.Massoudi, C.H.Durney, P.W.Barber, and M.F.Iskander, "Electromagnetic Absorption in Mutilayered Cylindrical Models of Man," IEEE Trans. on MTT, vol.MTT-27, no.10, Oct.1979, pp.825-830

35. N.Morita and J.Bach Andersen,"Electromagnetic Power Dissipation in a Circular Cylinder -A Model for Hyperthermia-," a copy from Institute of Electronic Systems, Aalborg University Centre, Nov.1980

36. S.M.Neuder,"Electromagnetic Fields in Biological Media, Part II-The SCAT Program, Multilayered Spheres, Theory and Applications," BRH, Aug.1979

37. A.R.Shapiro, R.F.Lutomirski, and H.T.Yura, "Induced Fields and Heating Within a Cranial Structure Irradiated by an Electromagnetic Plane Wave," IEEE Trans. on MTT, vol.MTT-19, no.2, Feb.1971, pp.187-196

38. M.A.Stuchly, A.Kraszewski, and S.S.Stuchly, "Implantable Electric Field Probe - Some Performance Characteristics," presented at 5th Annual Conference of Bioelectromagnetic Society, Jun.12-17, 1983

39. W.L.Stutzman and G.A.Thiele,"Antenna Theory and Design," Publisher: J.Wiley, 1981, see Ch.1

40. C.L.Wu and L.L.Tsai, "The Distribution of Induced Electromagnetic Field Inside Lossy Prolate Spheroidal Head Models in the Resonance Region," Submitted to IEEE Trans. on BME

41. T.K.Wu and L.L.Tsai, "Electromagnetic Fields Induced Inside Arbitrary Cylinders of Biological Tissue," IEEE Trans. on MTT, Jan.1977, pp.61-65

42. T.K.Wu,"Electromagnetic Scattering from Arbitrarily-Shaped Lossy Dieletric Bodies," a copy of PhD thesis from the Dept. of Electrical Engineering of the University of Mississippi, May.1976

43. T.K.Wu,"Electromagnetic Fields and Power Deposition in Body-of-revolution Models of Man," IEEE Trans. on MTT, vol.MTT-27, 1979, pp.279-283